UNIVERSIDAD CARLOS III DE MADRID

TESIS DOCTORAL

Enhancing the Radiated Power in the Terahertz Band

Autor:
Belén Andrés García

Director:
Luis Enrique García Muñoz

Departamento de Teoría de la Señal y Comunicaciones
Universidad Carlos III de Madrid
Leganés, Madrid, Diciembre de 2013

UNIVERSIDAD CARLOS III DE MADRID

TESIS DOCTORAL

Enhancing the Radiated Power in the Terahertz Band

Autor:
Belén Andrés García

Director:
Luis Enrique García Muñoz

Departamento de Teoría de la Señal y Comunicaciones
Universidad Carlos III de Madrid
Leganés, Madrid, Diciembre de 2013

TESIS DOCTORAL

ENHANCING THE RADIATED POWER IN THE TERAHERTZ BAND

Autor: Belén Andrés García

Director: Luis Enrique García Muñoz

Firma del tribunal calificador:

	Nombre y apellidos	Firma
Presidente:		
Vocal:		
Secretario:		

Calificación:

Leganés, de de

A mi familia

Los números primos sólo son exactamente divisibles por 1 y por sí mismos. Ocupan su sitio en la infinita serie de los números naturales y están, como todos los demás, emparedados entre otros dos números, aunque ellos más separados entre sí. Son números solitarios, sospechosos, y por eso encantaban a Mattia, que unas veces pensaba que en esa serie figuraban por error, como perlas ensartadas en un collar, y otras veces que también ellos querrían ser como los demás, números normales y corrientes, y que por alguna razón no podían. Esto último lo pensaba sobre todo por la noche, en ese estado previo al sueño en que la mente produce mil imágenes caóticas y es demasiado débil para engañarse a sí misma.

Abstract

The needs of the Technology, Science and Communications to have available the *Terahertz band* has grown dramatically during the last years. This band is still a challenge from the technological point of view. Considering two approximations, photonic and microwave, the first is not capable of delivering enough power to have a reliable communication or an efficient system. Regarding microwave, as the existing devices and systems should be scaled in frequency, the available manufacturing techniques and design processes are not capable of providing enough precision for the miniaturized devices on these frequencies. Despite these issues, the efficiency on the devices, either in the sources itself or in the antennas, regarding radiated power or coupling of electromagnetic fields, is not good enough, and most of the power is lost either on the lasers illuminating the devices, in the bias or simply in the coupling and matching.

It is important to know, also, that classical antenna theory, and the well known antenna topologies, need to be redesigned to allow the limitations of the technology in manufacturing process and also in the measurement of devices, for example, the design in *high permittivity* substrates or semiconductors.

Photomixers are, from the optics point of view, one of the most common way to generate a Terahertz signal. Their properties, such as easiness in manufacturing, tunnability, high integrability, operation at room temperature, and reduced cost make them affordable devices to implement in new systems, both with commercial purposes and also in the research field. Gathering together all the circumstances, the optimization of the radiation ele-

ments that serves as a matching between free space and the feed, is a key point to develop efficient devices as well as reduced in cost. It is important to develop radiating elements that can be processed and measured in the same wafe of the THz sources, reducing this way the complexity of the system. This means the radiating elements should be preferably in a technology that allows the manufacturing at the same procedure than the source.

The main goal of the proposed Thesis is the development and design of new devices, that allow the optimization of radiaton power and coupling between the THz source and the radiating element. This goal has been achieved with different antenna topologies, either in planar structures and in 3D devices. The first block of the Thesis is based on the use of photomixing devices, framed in a research stage at FAU (Erlangen), for the optimization of the radiating element adapted to n-i-pn-i-p photomixers. From this optimization, a reduction in the size of the element has been achieved, allowing the implementation of the next step, which are new 3D horns etched in the semiconductor material where the PM is processed.

The second block of the present work is the development of a modal theory for TSA antennas together with some applications that allows the validation of the theory as well as the implementation over semiconductor or high permittivity substrates. The baseline of waveguide theory was employed for the analysis with PMC conductors and air discontinuities. Three different applications have been designed, manufactured and measured, with good results in the band over study. The three of them are based on new geometries on the substrate where the antenna is printed, including EBG, substrate-superstrate configuration and thick wedges.

The third block is based on numerical methods, with the objective of analysis acceleration as well as the reduction of computational resources in the calculations and in simulations. First of all, QO techniques are employed, with the aid of the BME coefficients of the feed. A complex optical system including lens and mirrors can be analyzed in a matter of seconds, with a reduced error. To continue with resources optimization and also the analysis of reflectors, a combination of MoM+PO has been developed based on Krylov subspaces, imposing orthogonality on each step, together with the use of Macro Basis Functions; the feed is analyzed with MoM, and the impedances matrix is obtained, while the matrix from the reflector is computed with a PO approach. The complexity of the problem is reduced by a N_f/P factor with N_f the number of unknowns in the reflector and P the number of MBFs. To continue with MoM, and the analysis of large arrays, a method based on the modification of the impedance matrix taking into account the effect on impedance of the surrounding elements is developed.

Resumen

La necesidad de la Tecnología, la Ciencia y las Comunicaciones de tener disponible la *banda de Terahercios* ha crecido drásticamente durante los últimos años. Esta banda es todavía un reto desde el punto de vista tecnológico. Considerando dos aproximaciones, desde el punto de vista de la Fotónica y desde el de las Microondas, la primera no es capaz de entregar, o generar, suficiente potencia para conseguir un sistema de comunicaciones fiable y eficiente. Con respecto a la aproximación basada en Microondas, los dispositivos y sistemas que existen actualmente, se escalan en frecuencia, utilizando las técnicas de fabricación disponibles en la industria. Estos procesos, todavía no son capaces de proporcionar una precisión suficientemente alta para dispositivos miniaturizados y escalados a esta banda de frecuencias. A pesar de estas limitaciones, la eficiencia de los dispositivos, tanto en las mismas fuentes como en las antenas utilizadas, con respecto a la potencia radiada o el acoplo de los campos electromagnéticos, no es lo suficientemente buena, por lo que la mayoría de la potencia se pierde o bien en la iluminación de los dispositivos con láseres, en la corriente de alimentación o en el acoplo y adaptación.

Es importante destacar también que la teoría clásica de antenas, y las bien conocidas formas, necesitan ser rediseñadas para contrarrestar las limitaciones en la tecnología y procesos de fabricación y también en los procesos de medida, por ejemplo en el diseño con sustratos y semiconductores de *alta permitividad*.

Los *fotomezcladores* son, desde el punto de vista de la óptica, una de las formas más comunes de generar una señal en Terahercios. Sus propiedades,

como por ejemplo la facilidad en la fabricación, alta integrabilidad, ajuste en frecuencia, operación a temperatura ambiente y coste reducido, los convierten en dispositivos asequibles para implementar en nuevos sistemas, tanto con fines comerciales como en el campo de la investigación. Teniendo en cuenta todos estos factores, la optimización de los elementos radiantes que sirven de adaptación entre el espacio libre y el propio generador es un factor clave en el desarrollo de dispositivos eficientes así como de bajo coste. Es muy importante desarrollar estos dispositivos lo más eficientes posible así como de bajo coste. Otro punto con mucha relevancia es también que estos sistemas se puedan procesar y medir en la misma oblea o sustrato que la fuente de Terahercios, reduciendo de esta forma la complejidad de todo el sistema. Esto obliga a que los elementos radiantes se desarrollen en una tecnología que permita la fabricación al mismo tiempo de antena y fuente.

El objetivo principal de esta tesis es el desarrollo y diseño de nuevos dispositivos que permitan la optimización de la potencia y eficiencia de radiación y el acoplamiento entre la fuente de Terahercios y el elemento radiante. Este objetivo se ha conseguido con la utilización de diferentes formas de antena, tanto en estructuras planas como en dispositivos 3D. El primer bloque de esta tesis se basa en el uso de fotomezcladores, enmarcado en una estancia de investigación en FAU (Erlangen), con el objetivo de optimizar el elemento radiante adaptado a sistemas n-i-pn-i-p. A raíz de este trabajo, se ha conseguido una reducción en el tamaño del elemento, permitiendo la implementación del siguiente objetivo: bocinas 3D grabadas en material semiconductor, donde se implementa el fotomezclador.

El segundo bloque del presente trabajo es el desarrollo de una teoría modal para antenas de tipo TSA junto con varias aplicaciones que permiten la validación de esta teoría, así como la implementación sobre sustratos semiconductores o de alta permitividad. Se ha empleado como punto de referencia teoría de guías de onda clásica, para su análisis con conductores magnéticos perfectos e interfaces aire-sustrato. Se han desarrollado tres aplicaciones para esta teoría, además de fabricadas y medidas, con buenos resultados sobre la banda de frecuencias bajo estudio. Las tres aplicaciones están basadas en nuevas geometrías en el sustrato donde se implementa la antena, incluyendo EBG, configuración sustrato-superestrato y cuñas gruesas.

El tercer bloque de esta tesis se centra en métodos numéricos, con el objetivo de la aceleración del análisis así como la reducción del coste computacional y de los recursos empelados en cálculos y simulaciones. El primer método que se ha estudiado se basa en técnicas quasi-ópticas, con la ayuda de desarrollos de BME para obtener los coeficientes de las fuentes. Un sistema complejo incluyendo lentes y espejos se puede analizar en cuestión de

segundos, con un bajo error. Para continuar con la optimización de recursos y con el análisis de elementos ópticos, se ha desarrollado una combinación de MoM+PO basada en subespacios de Krylov, imponiendo ortogonalidad en cada paso, junto con el uso de MBFs; la fuente se analiza con MoM, obteniendo la matriz de impedancias, mientras que la matriz correspondiente al reflector se calcula con PO. La complejidad del sistema se reduce en un factor N_f/P, con N_f el número de incógnitas en el reflector y P el número de MBFs. Para continuar con MoM, y el análisis de arrays con un número elevado de elementos, se ha desarrollado un método basado en la modificación de la matriz de impedancias teniendo en cuenta el efecto en esta impedancia de los elementos circundantes.

List of Acronyms

3D	3-Dimensions
AUT	Antenna Under Test
BF	Basis Functions
CPS	Coplanar Strip
CW	Continuous Wave
EBG	Electromagnetic Band-Gap
EM	Electromagnetic
FAU	Friedrich Alexander Universitat
FDTD	Finite Difference Time Domain
GaAs	Gallium Aresenide
HE	Magnetic Electric
InGaAs	Indium Gallium Arsenide
LAEs	Large Area Emitters
LT	Low Temperature
LTSA	Linear Tapered Slot Antenna
MBF	Macro Basis Function
MoM	Method of Moments
MPL	Max Planck Institute for the Science of Light
MSE	Mean Square Error
PEC	Perfect Electric Conductor
PM	Photomixer
PMC	Perfect Magnetic Conductor
PO	Physical Optics

SEM	Scanning Electronic Microscope
Si	Silicon
SKA	Square Kilometer Array
SLL	Side Lobe Level
TE	Transverse Electric
TEM	Transverse Electromagnetic
TM	Transverse Magnetic
TSA	Tapered Slot Antenna
THz	Terahertz
UCSD	University of California San Diego
UV	Ultraviolet radiation

Agradecimientos/Acknoledgements

En esta tesis, por suerte, tengo muchos agradecimientos que hacer. En primer lugar a mi director de tesis Quique, que confió en mi en su día para realizar mi proyecto de fin de carrera, y después para esta tesis. Siempre he tenido su apoyo en cualquier circunstancia, tanto en las estancias en el extranjero como en la universidad. El me dio a conocer el mundo de la investigación, y me ha brindado todas las oportunidades a su alcance para realizarla. También a Daniel Segovia, Magdalena Salazar y a todo el grupo de radiofrecuencia de la UC3M, el GREMA, donde he tenido el honor de trabajar todos estos años, y al departamento de Teoría de la Señal y Comunicaciones.

Quiero agradecer a mis compañeros de laboratorio todos estos años: Edu, Ogarpe, Dani, Javi Herráiz, Javi Montero, Nacho y Alex, por toda su ayuda tanto durante mi estancia en la Universidad, como fuera, y también por su amistad después. He disfrutado mucho con vosotros durante esas discusiones estrumeantes, en el comunio y las cervecitas.

I would like to thank also Prof. Christophe Craeye, from UCL, where I did my first research stage, and also David, who helped me both at work and also out of work while I was there. They taught me everything they could about numerical methods, and also they were a great help out of work. I also would like to thank the hospitality from all the people working at that time at UCL, Ulash, Lyazid, Greg, etc.

The next stage related with this PhD was at FAU, where Prof. Stefan Malzer and Prof. Gottfried Dohler gave me the opportunity to work with them, learning everything I know about photomixers and helping me with my stage there. I also would like to thank Sascha and Sebastian, who were

wonderful hosts and also taught me everything about photomixers and they work. They brought me the first opportunity to work in a THz lab.

I can not finish the acknolegments without mention Prof. Rebeiz, from UCSD. He accepted me in his group, and treated me like one of his students, helping with the work and also making everything on his hands to give me the knowledge and strength to achieve great results. I would like to thank also all the people working at UCSD with Prof. Rebeiz: Hosein, Alex, Berke, Chirag, Jen, Ozgur, Yu-Chin, ...

Ahora empieza el turno de lo personal, aunque muchos de los de arriba, habés pasado también a ese terreno, y espero que sigamos así muuuuuuchos años más.

Necesito empezar estos agradecimientos con los que siempre han estado ahí, en los buenos y los malos momentos, siempre con unas palabras de ánimo, Elena, Celia, Beita, Rober, Johan, Bea Cipri, Irene, Ferda, Rober, Tamara y Jose. Que aunque estemos en la distancia, siempre estamos unidos, y sobre todo, cuando nos necesitamos.

A mis amigas de toda la vida, Lau, Marta e Iris, que siempre vamos a seguir ahi!!! da igual los años que pasen!!!!! porque siempre parece que nos hemos visto el día anterior, y es como volver a estar en casa.

A Cris, a Iván, a Bárbara, Sergio y Jorge porque también habéis estado ahí, en muchos momentos, buenos y malos, con sonrisas y con lágrimas, y aunque hayáis vivido solo la recta final, esta tesis tiene mucha, mucha parte de vosotros, porque me habéis animado hasta la saciedad, porque sigamos así muchos años más, y porque pasemos muuuuuchos findes más de los que nos gustan ;-)

Both are alive, thanks to... who knows... both jumped into the deepness, with a strange feeling of What were they going to find there, or How were they going to get out of it. But there is a light, up in the shallow. And both started to climb up, and one day, they will reach the highest of the mountains.

A los compis (y amigos) y senseis de buceo, porque sin vosotros no habría pececillos, ni cuevecillas, y no me hubiese inspirado tanto: Ester, Patri y Carlos, y Bonico DEL TÓ, porque hagamos muchas más Medas juntos; a Sergi, Inma, Juandi, Andi, Boris, Fran y todo el equipo de Rivemar, por hacerme sentir como en casa y poder desconectar, porque sin eso esta tesis tampoco hubiese sido posible.

A mis compis de la uni!!!! porque aunque el trabajo nos separe, sabemos que podemos contar las unas con las otras, y siempre nos quedan esos gintonics de moda!! Patri y Lau!!! las telequitas!

Porque tras años y años, seguimos teniendo vidas paralelas, y siempre las

tendremos, porque ni me acuerdo desde cuando somos amigas, porque se que siempre vamos a estar juntas, da igual la distancia y el tiempo, y porque si yo he podido, tu puedes más!!!

A la gente de Deimos, que también ha vivido la última parte de esta tesis, y porque es un honor trabajar con ellos todos los días.

Rosa!! no me olvido de ti!!! que nos contamos y nos contaremos nuestras penas, y nos reiremos muchísimo juntas!! porque eso nos falta todavía!! muchas risas!!!! y por esos findes sanadores!!

Ao meu curmán Javi, porque tamén hai moita parte de ti nesta tese, sobre todo na recta final, para que nos vexamos na terriña, que estamos ambos os dous moi desterrados.

Miguel, que aunque te diga que estás muy loco, cerrar esta tesis ha sido una de las mayores satisfacciones de mi vida, tienes que perseguir tus sueños, y lo estás haciendo muy bien, no importa las piedrecitas que nos pongan en el camino, tu siempre has estado a mi lado y yo también estaré ahí, nunca olvidaré nuestros cafés, comidas, cenas y buenos ratos que pasamos juntos, y con Félix, que no me olvido!!! aunque tarde mucho más de lo debido en llamarte; Adam, con quien también he compartido viajes, y seguro que alguno más haremos.

To the people in San Diego, all of you know that you made me feel like at home, and I will go back sometime soon, I promised, and I will do it, and we will hang out again together, because I don't forget you, ever, you were a very important part of my life, and you made me as I am now, Silvana, Viktoria, Jackie, Raleigh, Bill, Cristina, Amber, Kelli, and all the people in Power Scuba, the Spanish living there and the people from UCSD.

I don't forget you, you were the one introducing me to yoga and surf, and San Diego will not ever be the same without you, and you will be always in every yoga class, in every surf table I touch, and I miss you.

A mi primi, que a pesar de la distancia, siempre estarmos unidas, sigue a tu corazón, porque así sabrás que no te vas a equivocar, porque en ese momento, lo sentías así.

A mi familia, a mis padres, a mi tio, porque aunque haya muchos agradecimientos por arriba, sin vosotros no estaría aquí, ni mi vida sería igual, porque me habéis ayudado siempre y habéis confiado en mi, y seguís haciéndolo, gracias por estar ahí.

A todos, porque TODA esta tesis está formada por partes de vosotros.

Contents

CHAPTER 1

Introduction

The human being is curious itself. The eagerness for discover, explain and reason the surrounding world is an intrinsic human quality, something that has driven him not only from his origins, not only to explore the universe, but to theorize about it and try to give a sense of what is happening around. Religion, Philosophy or Science are disciplines emerged from the need of having a knowledge of the world, and finding real explanations about it, that in any case, satisfy our curiosity.

In ancient times, the Greek and Roman civilizations appealed to myths as a way of justify life and dead, and all the events happening around them, especially the adversity. Their hypotheses are not far from the subsequently scattering by the different Religions emerged around the world and survive nowadays. Some theories are superimposed with others, modifying them as they please or shifting them depending on the influence over people, over faith power, and the relevance for the mankind. Or what is equivalent, they agree with the man's knowledge need, his concerns and eagerness.

The human being is an information absorber, he needs it to elaborate his own theories about life and universe; he is strongly dependent on it to continue the evolution in all other aspects of his life: as an individual, with society and with the world surrounding him. After thousands of years of study and research, from all perspectives and points of view that allow the science areas, the human being has fulfilled the expertise and solved and answered questions about certain aspects of reality that were unexplained or

strange. Step by step, some theories and explanations are found, but loads of new of them arise at the same time, as an exponential matter. Each acquired knowledge, each proven theory, each successful experiment, is a contribution to clear a side of the exotic and undiscovered, but, most of all, they encourage our eagerness and our hunger.

As the knowledge of our world increases, the more and more resources are available to act and explore it, to make it progress, to develop it, but unavoidably, this evolution is transformed in a new reality to cope with, in new challenges and in new study subjects, we need to find new information sources. Once again, we question ourselves and we still need more answers.

A spectator, who waits sitting on the darkness, for the function to start, waiting to discover the hopes and deceptions, the evolution and blockages and the content of the play that someone has created in a piece of paper. While he is waiting, on the darkness, schratch yesterday's small wound on his arm, falling off his bike, and asks himself why those small cells are there, how do they know their function and the best behavior for him. Why do they work as they do? What does they make themselves being like that? How do they organize and know what to do on every occasion...? While his arm is resting in the armchair, his attention wander to the environment. He tries, being in darkness, to imaging the surrounding world, from the theater build up, to the foundations, below the floor, asking himself why is him, who in that specific moment and place, is about to see a function, in one of the not many dry sites of the planet, mainly water, and which we are not completely sure about its performance as a system, how it is organized and how it is evolving in a geological structure, and if we are transforming it, either for good or bad. Immediately jumps to a sphere of a bigger attention; In the darkness, the sound of a horn in the outside of the theater.

What it is in the outside of the theater? His looking tries to see in the darkness of the room the stars, he knows they are out of it, even out of our Solar System. Once again, What is it there? Why? How much do we really know? How do we use what we know? Is that the biggest sphere? Maybe there is one, two, or three more... When the light switch on, the spectator realize that is exactly him who has been sit in the center of the scenario, the play lie in the voyage towards our own knowledge, the one surrounding us and the one that we can not even perceive, because of the distance or our imagination. We are the leads, in the title of the play says: 'curiosity'. But this consideration is never motivated in an space dimension, when the other is alive, the time.

That spectator can remember that when he just got his PhD, his attention was entirely into knowing the objective of his studies, a human cell, the earth

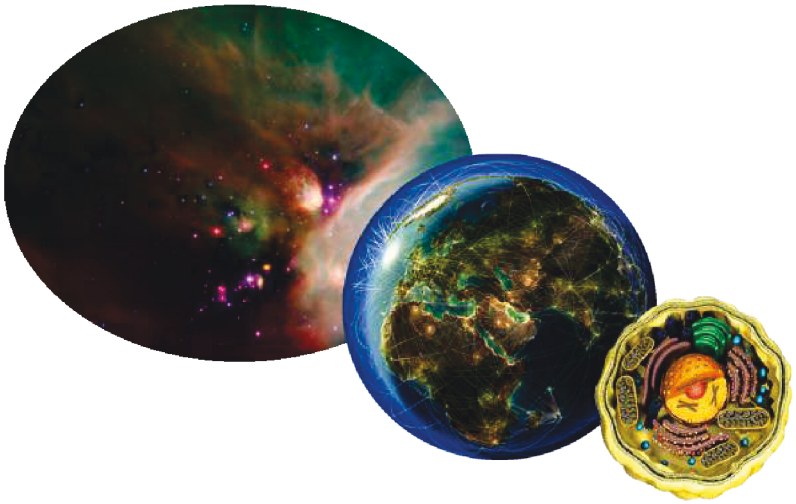

Figure 1.1: Ophiuchus constellation, the world and a human cell

or the space. With time, and knowledge, his study sphere became huge, and the curiosity forced him to question how to transform that cell, the planet or the universe, and all our efforts nowadays are based on that, at least, in the two first spheres, the cell and the environment, inside us and the world around us.

As an old fellow professor, knowing in a first moment why things happen and in a second how to change them, he asked in a third point for what knowledge sphere are the best applications and possibilities that for the acquired expertise, What is the best use of all of it? On every aspects up to now, the direction was linear, either spatial or temporal, but in all of them linear, not probabilistic or quantic in more scientific terms. In the world that we have to live, where the information and communications are instant and the knowledge flows in huge quantities from one side to another of the world, in a universe that an electron can be, from a quantic point of view, in two different sites at the same time, just because having the same probability of being in one site or another, it is possible that those three knowledge spheres will not be go over in a linear behavior, from small to big or in the other way around. It is possible that those three spheres are connected between them, the small, the environment and the infinite, the cell, the planet and the universe, or they can be superposed between them, as circles drawn in different pages of a closed book, we need to go through them in a new form.

The Terahertz band, in the scope of this thesis, is opening a huge range

of possibilities to explore the human body, by developing new techniques of body scanning; the world surrounding us, by enhancing the bandwith and allowing powerful communications; and the universe, beyond us, by launching telescopes and instruments to space with new scanning capabilities, going beyond what is already known by the Astronomers.

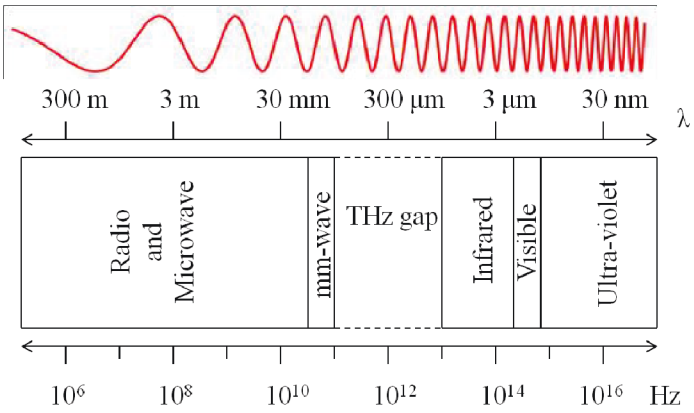

Figure 1.2: Schematic diagram showing the location of the THz band in the electromagnetic spectrum

1.1 State of art

The Terahertz radiation is typically used to describe the region of the electromagnetic spectrum in the range of 100 GHz (3 mm) to 10 THz (30 μm) [1, 2, 3], which is between the millimetre and infrared frequencies. The THz band has variously been named such as sub-millimetre, far infrared and near millimetre wave. At 1 THz, the radiated signal has 300 μm wavelength in free space, 1 ps period, 4.14 meV photon energy and $hf/k_B = 48K$ temperature; where h is Planck's constant, f is frequency and k_B is Boltzmann's constant. Fig. 1.2 depicts the location of the THz band in the electromagnetic spectrum.

This portion of the electromagnetic spectrum is the least investigated region because of the absence of efficient, coherent, and compact THz sources and detectors [3, 4]. These characteristics for the sources can be found in the common microwave-frequency sources such as transistors or RF/MW antennas and in devices working in the visible and infrared range like semiconductor laser diodes [5]. However, it is not possible to adopt these technologies for operation in the THz region without a significant reduction in power and

efficiency. At the lower extreme of THz frequency range, the generated power by solid-state electronic devices, such as diodes, has roll-offs of $1/f^2$ [6] due to reactive-resistive effects and long transit times. On the other hand, optical devices, such as diode lasers, do not perform well at the THz range limit because of the lack of materials with adequately small bandgap energies [5]. Hence the term 'THz gap' is phrased to explain the infancy of this band compared to well-developed neighbouring spectral regions. Recent advances have commenced to address this problem and various types of new emitters and detectors based on semiconductor technology are emerging [4, 7, 8, 9].

In this introduction, first, different THz sources and detectors are reviewed. Then, THz wave properties and applications are described. Based on the built foundation, the research motivations and objectives of this thesis are outlined.

The THz source has been considered as the most difficult component to realise among all the elements in this technology [10]. A great deal of effort has been put to extend RF/MW and optical technologies to THz band and even combine them in order to realise THz sources with better performance [11]. Thus, THz emitters are divided into three main groups: THz sources developed from RF/MW side, THz sources extended from optical side, and THz sources combining RF/MW and optical techniques.

1.1.1 THz Sources from RF/MW Side

In this category, diodes and THz vacuum tube sources are explained. Regarding diodes and frequency multipliers, on the lower end of THz spectrum, diodes can transfer the functionality of lower frequency electronics into the THz band. There are several types of diodes, such as Gunn diodes, IMPATT diodes and resonant tunnelling diodes (RTD). Although the operation bases of these diodes are different, the principle of power generation from these diodes is the same and it is based upon their negative differential resistance [12]. Each of these diodes has its own advantages and disadvantages [12, 13, 14, 15, 16, 17] nevertheless, in these components by increasing the frequency there is a dramatic reduction in power [14].

Another method to reach THz band is the use of frequency multipliers which outperform other solid-state electronic sources. This is because the diode multipliers are operationally and physically simple [13]. Since higher order multipliers are extremely inefficient, series arrangements of doublers and triplers have mostly been implemented [10]. In this method, chains of microwave sources, such as GaAs Schottky diodes, at lower GHz bands ($20\ to\ 40\ GHz$) can be used in series to drive multiplication at THz ranges

[13]. However, the output power from multipliers decreases at higher frequencies [18] and the bandwidth of these sources is limited.

1.1.2 THz sources from optical side

THz sources from optical side are mainly divided into lasers with different generation techniques and nonlinear crystals.

For molecuar lasers, by injecting grating tuned CO_2 lasers into low-pressure flowing gas cavities, THz signals with power level of a few ten milliwatts can be produced [10]. The frequency of this THz power depends on the spectral line of the gas; for example, a rotational transition of methanol occurs at 2.522 THz.

THz semiconductor diode lasers are very successful and prevalent in the near-infrared and visible frequency ranges, however; for THz bands materials with suitable band gaps are not available unless considering artificially engineered materials [5, 19]. Therefore, the concept of THz Quantum-Cascade lasers (QCL) which are intra-band lasers and require creation of quantized sub-bands was introduced [4]. QCL can operate in both pulsed and continuous-wave (CW) modes; its operating frequency is controlled by quantum well design (band gap engineering) and different wavelengths can be achieved in the same material. QCLs have been one of the most intensive research topics in THz area during the past decade and the survey on different THz QCLs show that the frequency range of these devices span from 0.84 THz to 5 THz at various cryogenic working temperatures [20, 21, 22, 23] with the best peak optical power of 200 mW at about 4.5 THz [5] and the best peak operating temperature of 200 K at about 3.2 THz [24]. It is good to add that at room temperature, a THz QCL with power of 8.5 μW at 4 THz has been demonstrated [25]. To sum up, QCLs have larger output power at higher THz frequencies and as frequency decreases the power reduces considerably. One of the main limitations of THz QCLs is that for THz operation they need cryogenic cooling and this restricts operation of QCLs to the laboratory environments.

Another option for THz generation is to use optical down converters. One of the common methods for THz generation is the use of nonlinear crystals with large second order susceptibility, χ^2, for down conversion of power from optical regime. Several nonlinear materials for this purpose can be used [11]. THz parametric processes such as parametric oscillator or difference frequency generation (DFG) are techniques for generation of monochromatic highly tunable THz wave sources with high spectral resolution [26, 27, 28]. Another optical down conversion method is the optical rectification in which

all possible difference frequencies of spectrally broad optical pulses are generated. The major limitation of this technique is that phase matching between the optical fields and induced THz field is required. The THz output power in this method is low; hence, high power optical sources are required for generating meaningful THz power. However, wide THz bandwidth from this method is achievable [3].

1.1.3 THz sources combining RF/MW and Optical techniques

THz antennas which are based upon photoconduction can be allocated to this category of THz sources. As shown in Fig. 1.3, a THz antenna consists of a biased antenna mounted on a photoconductive substrate (commonly GaAs). Optical laser sources as the excitation sources of THz antennas are used to produce THz waves by inducing rapid changes in the carrier density of the photoconductive substrate. Depending on the type of optical excitation, there are basically two alternatives for THz antennas:

- THz photoconductive antennas in pulsed systems
- THz photomixer antennas in CW systems

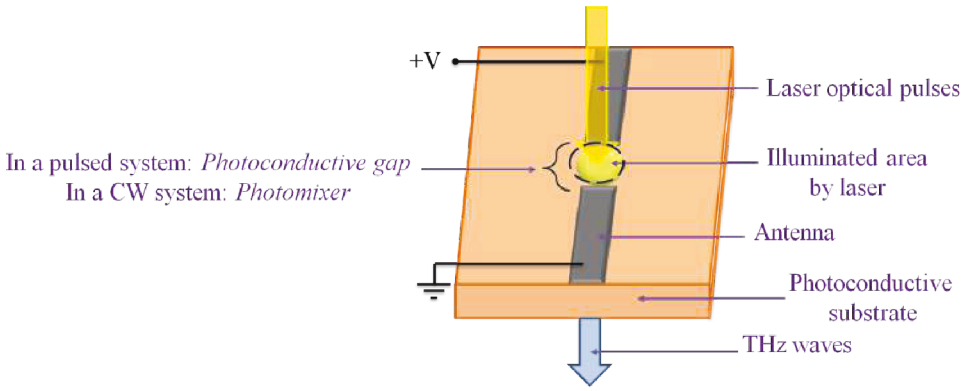

Figure 1.3: THz antenna as an emitter for both pulsed and CW THz systems, including optical laser illumination, photoconductive substrate, and metallic antenna with a bias voltage.

Although it is possible to use the same antenna in both systems, different excitation methods dictates different requirements for each antenna type and result in different generated THz waves and applications. In THz pulsed systems, because of the external bias field, the optically induced photo-carriers

in the photoconductive gap give rise to rapid changes in the current density. These currents induce a THz electromagnetic field in the connected antenna, and as a consequence, ultrafast electrical pulses are produced and radiated into free space. In CW systems the process is the same; however, usually two monochromatic lasers with slightly different optical frequencies are used for THz emission from the antenna. This inherent difference in excitation methods of THz pulsed and CW systems leads to the generation of ultra wideband and (tuneable) narrow band THz waves respectively. In a CW system, the term of 'photomixer' refers to the antenna gap (which can have various designs) in analogy of 'photoconductive gap' in a THz pulsed system. Detailed and comprehensive study and investigation on THz antennas will be presentenced in next chapters.

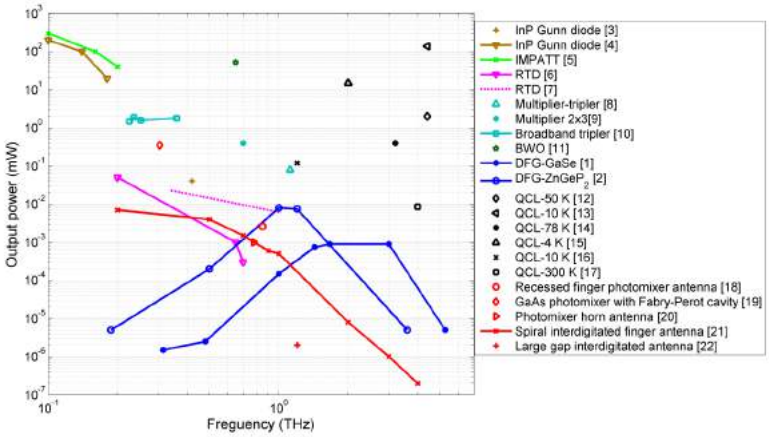

Figure 1.4: An outline of THz sources, average THz output power versus frequency. The same colours correspond to the same type of the device and more information on difference of the devices in the same category is stated in the legend.

1.1.4 Terathertz detectors

Progress in THz detectors have been faster than in THz sources [10]. One of the main issues in detection of THz frequencies is that the photon energy in this frequency band is in the range of 0.41 to 41 meV which is comparable to the background thermal noise energy. Therefore, to overcome this problem, mainly two methods have been adopted: cryogenic cooling and signal integration for long enough periods [10]. It is possible to categorize THz detection to coherent and incoherent techniques. The main difference between them

is that in coherent technique both the amplitude and phase of the received signal are determined; but in incoherent technique only the intensity of the signal is measured.

Heterodyne detection is an important coherent technique in detecting weak and narrow band signals. In this method, a mixer, a non linear device, as a local oscillator is used for frequency down conversion. Fig. 1.5 demonstrates the process of electronic heterodyne detection. The amplitude of the detected signal is proportional to the amplitude of the THz signal [2]. There are various types of mixers in THz range. A Schottky diode is a common and basic mixer type for room temperature detectors where a modest sensitivity is required. However, for high sensitivity applications, superconducting heterodyne detectors are employed that operate in cryogenic temperatures. SIS tunnel junction mixers and HEB mixers are two examples of mixers in this category.

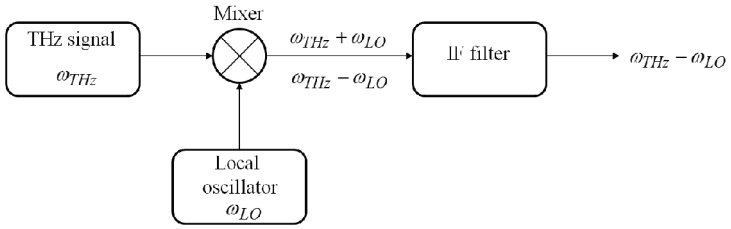

Figure 1.5: Block diagram of a THz heterodyne detector.

Electro-Optic (EO) sampling and detection by THz antennas are also coherent methods. In the former, the amplitude and phase of the THz signal were measured by using a nonlinear crystal. In the latter type as shown in Fig. 1.6, the THz signal induces voltage across the antenna which leads to generation of THz current due to existence of free electron-hole pairs in the antenna gap. The phase of the THz signal in these methods can be measured by varying the optical path length of the optical probe pulse. Direct detectors such as Golay cells and bolometers are mainly incoherent detectors. These detectors at room temperature are appropriate for applications where high spectral resolution and quick response time (it is on the order of seconds) are not required [10]. For a better sensitivity and dynamic range, cryogenic cooled direct detectors such as cryogenically cooled bolometers that have response time on the order of microseconds can be employed [10].

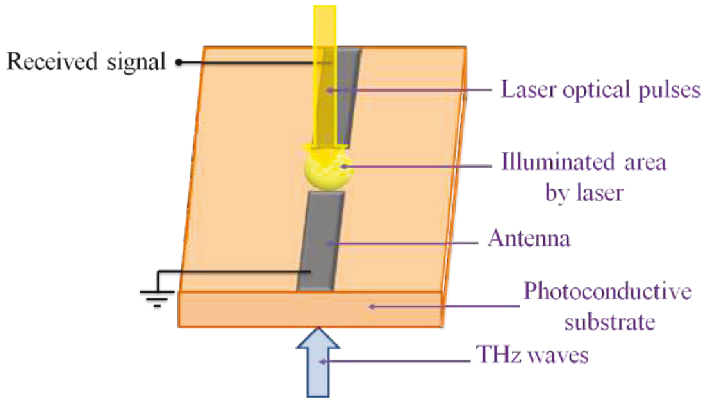

Figure 1.6: THz antenna as a detector for both pulsed and CW THz systems, unlike the emitter, THz detector has no bias voltages and THz waves usually come from the substrate direction while the optical pulses hit the detector from the antenna side.

1.1.5 The Terahertz Wave Properties and Applications

Although interest in THz region dates back to at least from 1920s [29], extensive studies have been devoted to this region only within the past three decades. A key motivation for this is the exceptional wave properties and, as a result, the possible applications in the THz frequency range. Since THz region is contained between microwave-millimetre and infrared areas it has mid-characteristics borrowed from the two bands. These properties can be summarised as follows:

1. *Penetration*: The wavelength of THz radiation is longer than the infrared radiation; hence, THz waves have less scattering and better penetration depth ($\approx cm$) compared to infrared ones ($\approx \mu m$).Therefore, dry and non-metallic materials are transparent in this range but are opaque in the visible spectrum.

2. *Resolution*: THz waves have shorter wavelength in comparison to the microwave regime, this gives a better spatial imaging resolution.

3. *Safety*: Opposite to X-rays, the photon energy in THz band is much lower. Therefore, THz radiation is non-ionising.

4. *Spectral fingerprint*: Vibrational modes of many molecules lie in THz range.

THz radiation has distinct atmospheric characteristics compared to the microwave and infrared waves. THz waves have extremely high absorption in

the atmosphere and in moist environments. Fig. 1.7 depicts the atmospheric attenuation across the electromagnetic spectrum. It is obvious that signal degradation in this range- with the main peak attenuation between 1 to 10 THz- is considerably higher than microwave and infrared bands. Thus, for long range ($>$ few hundred meters) the required power for signal transmission is high and non-practical [6]. However, the application of THz waves in the two following environments is possible.

1. In space, since the ambient is near-vacuum, signal absorption and attenuation due to water drops are not present. Moreover, black body temperatures of THz signals lie in the range of $4.8 - 480\ K$ which means the majority of ambient radiation is THz light. Considering spectral signature of interstellar dust which is located in THz region, and aforementioned advantage of THz signals in space, THz technology is a very interesting and common used technique in Radioastronomy and space science [10]. For instance, Herschel Space Observatory, the largest infrared space telescope, was launched in 2009 in THz region by the European Space Agency [30].

2. For short range applications ($<$ 100 m [6]), atmospheric attenuation is not a big issue. Hence, THz technology is a very versatile tool for fundamental investigations in various disciplines such as Physics and Chemistry.

It is good to add that despite of negative effect of water vapour lines on THz signals, these lines are narrow enough and their positions are known; this allows removal/recognition of their effect in THz applications such as Spectroscopy [31].

Based upon THz wave properties, THz radiation can be applied in many possible applications including Imaging, Spectroscopy and Wireless Communications [11, 33, 34]. Although THz applications have been widely investigated, only in recent decades several commercial THz imaging and spectroscopy systems have entered the market by companies such as TeraView Ltd. [35], Picometrix [36] and Toptica [37]; or the first THz camera that can see and record in real-time at room temperature was introduced in early 2011 by Traycer [38].

For THz Pulsed Systems applications, the work of pioneers in THz pulsed imaging [39] and THz CW imaging [40], applications based on THz imaging have been on the focus of many research areas [33]. Medical imaging is one of the main subcategories in this field. THz waves can penetrate up to a few hundred micrometers (μm) in human tissues; therefore, it is a convenient

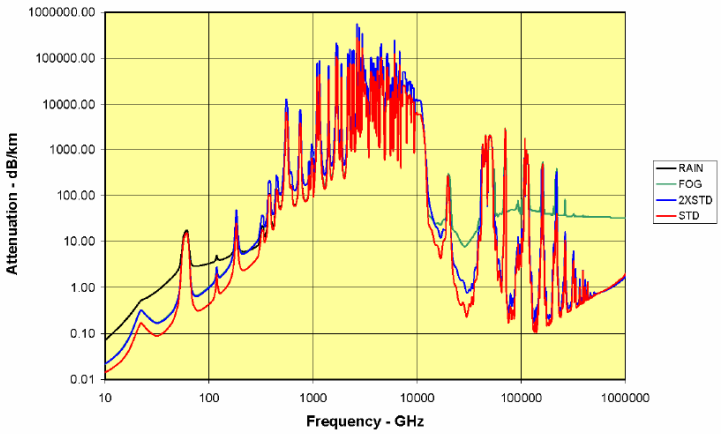

Figure 1.7: Attenuation at sea level for different atmospheric situations, Rain = 4 mm/h, Fog = 100 m visibility, STD = 7.5 gm/m^3 water vapour, and $2 \times STD$ = 15 gm/m^3 water vapour [32]

method for body surface diagnosis such as skin, breast and mouth cancer detection [35, 41, 42] and dental imaging [43]. Some of the benefits of this method can be named as, early detection of cancerous tissues and tooth decay or minimisation of the damage to the surrounding healthy skin in biopsy [35]. THz medical imaging has two major drawbacks; the equipment is expensive and data acquisition time is long. The latter disadvantage has been addressed by employing arrays of antennas and micro lenses [33].

THz pulsed Spectroscopy has been another fascinating application for commercialising THz technology in diverse areas [10] since the first introduction of this method in [44]. Now THz spectroscopy is a very powerful technique to characterise material properties and understand their signature which lies in the THz band because many molecules have rotational and vibrational transition lines in this range of frequency. One type of interesting THz spectroscopy applications is in Biochemical science such as analysis of DNA signatures and protein structures [45].

Also, THz radiation is a suitable technique to investigate material integrity and inspect multi-layered materials such as wood, composites, and cloths which are transparent in THz frequencies. THz pulsed imaging and spectroscopy has been adopted for non-destructive testing; for example, on imaging antiquities [46, 47] to reveal the thickness of the different layers of the art work and to show types of their materials [48]. This technique can be used for in-line control of polymeric compounding processes as well [49].

Furthermore, THz pulsed imaging and spectroscopy are two strong quantitative and qualitative non-invasive methods for examining pharmaceutical solid dosage forms [50, 51]. THz systems have the market potential for security applications [33] because of the possibility of using these systems in personnel screening [35], solid explosive material detection [52, 53], and mail screening [54]. However, THz signals are not transparent to metals; therefore, they are not suitable for imaging inside metallic suitcases. Thus, this method can be treated as a complementary scheme for the well-established monitoring techniques like X-ray [33].

Although high water absorption is one of the drawbacks in the THz area, it can be manipulated positively to distinguish the hydrated substances from dried ones. For instance, in paper industry, THz spectroscopy has been used for monitoring the thickness and moisture content of papers by manufacturers [55, 56]. THz pulsed imaging is a very convenient method to take 3D images from the inside of an integrated circuit device compared to 2D images provided by the X-ray method [35].

As a summary, schematic overview of various THz applications based upon optoelectronic systems is depicted in Fig. 1.8.

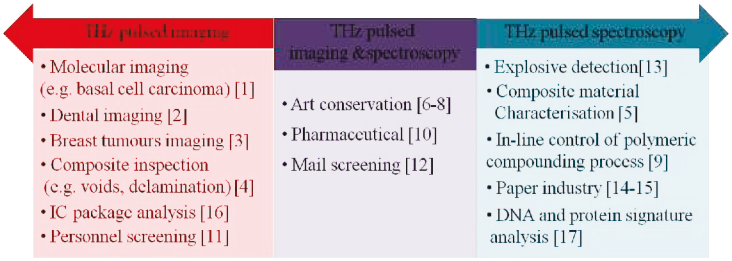

Figure 1.8: Overview with some of commercial and laboratory applications of THz pulsed imaging and spectroscopy across the various sciences.

It is good to mention that there is one interesting THz application which cannot be categorised in either of THz pulsed Imaging or Spectroscopy and that is THz application in Wireless Communication. To provide sufficient transmission capacity for future high data rate demands, higher carrier frequencies need to be employed and potentially THz frequencies can satisfy this request. However, THz communication links inherently have two main limitations: 1) THz signals can only propagate short path length without severe atmospheric attenuation 2) THz communication systems should be line of sight. Considering these restrictions, THz communication systems can be a suitable option for indoor short distances multipoint to point/multipoint basis at frequencies between about 0.2 to 0.3 THz [57]. From another point

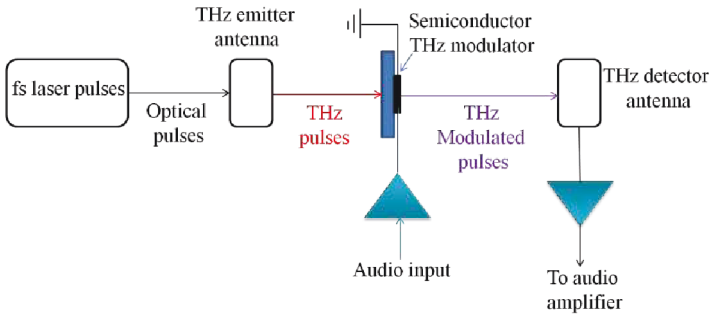

(a)

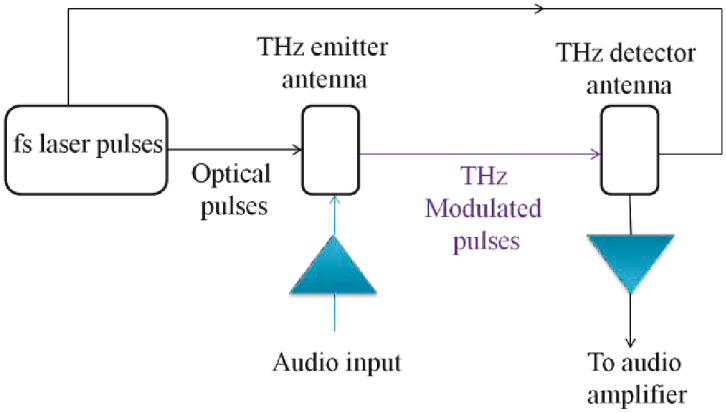

(b)

Figure 1.9: Schematic diagram of THz communication links for (a) system of [59] with external modulator (b) system of [60] where voltage modulation of the THz antenna is used.

of view, these restrictions are beneficial for secure THz communication. Since the beam is highly directional and it attenuates severely over the distance, unwanted signal detection and jamming is very difficult. Some THz data communications for short ranges ($< 1\ m$) based upon THz time domain systems have been tested at 0.3 THz in recent years [58]. In [59] a external semiconductor THz modulator is used with data transmission of 6 kHz while in [60] audio signals through the voltage of the transmitter THz antenna modulates the THz frequency and the reported data transmission was 5 Kb/s. The block diagrams of these two approaches are shown in Fig. 1.9.

For CW applications, although THz pulsed Imaging and Spectroscopy can provide data on broadband frequency ranges, for some applications such as gas-phase spectroscopy, high frequency dielectric measurements of electronic, metamaterials and nano-materials, and analyses of signatures in microliter

DNA [35, 61, 62, 63], narrowband high resolution systems are required. THz CW imaging and spectroscopy systems can provide such opportunity [64, 65]. It is good to add that for some applications like imaging of aircraft glass-fibre composites or determining thickness of a sample, both pulsed and CW imaging methods can be used [58, 66].

1.2 Objectives

This thesis is focused on the optimization of devices and techniques with the goal of having powerful systems on the THz band. It has been in great expansion in the last decade due to the improved technologies and techniques on manufacturing small devices in special substrates.

The increase on the number of sources and their improvements for the THz band also demands a better design of the radiated antenna, and its adaptation to new substrates with new designs or new topologies.

On the line of increasing the power radiated by THz isolated antennas, the second approach is based on the idea of new topologies of already existing elements. The main problem of classical antenna theory is the lack of thin substrates, especially due to manufacturing issues. Also, the feeds at these frequencies are mainly fabricated on high electric permittivity semiconductor, making it difficult the design of antennas in terms of impedance and radiation to free space. An antenna is nothing else than the matching to vacuum or air of the electromagnetic wave, according to Babinet's principle. With semiconductor substrates, the high permitivity absorbs all the radiation, preventing the energy to be radiated to the free space. Also, there are technical difficulties on the production of thin substrates that can be used to manufacture the elements. One of the most common approach is the use of photomixers, due to its bandwidth, the reduced size their easiness to manufacture, tunnability, reduced cost and operation at room temperature. Most of the new topologies on this PhD thesis are based on ultra wideband antennas.

1.3 Outline

The structure of the present thesis is as follows:

There are three main blocks, converging in the optimization of Terahertz devices, first physically from photonics and solid state approaches together with new topologies. The last block presents acceleration methods to analyze

the properties of theses systems.

In more detail, in Chapter 2 basic antenna designs are modified to meet Terahertz techniques and manufacturing restrictions. Different types of antennas are employed, optimizing the design to the material properties and to the characteristics of each feed. Also, some techniques to increase the radiated power are presented.

One step further, in Chapter 3, the antennas measured and designed in the previous Chapter, are employed to continue the power enhancement with new geometries. Dielectric horns are designed in the InGaAs substrate, where the PMs are implemented, and the modes propagating inside are also studied.

In order to obtain more power and also to allow the use of different feds, new antenna topologies needed to be designed. The need to eliminate the Si lens from the system, that introduces losses, forces the design to end-fire antennas. In Chapter 4, Tapered Slot Antennas are studied to obtain new substrate geometries. With this goal, a modal theory is presented based on waveguide technology, while some applications for it are studied and also measured.

To continue improving the efficiency and especially, for this case, the computational resources on THz analysis, three different techniques have been developed in order to analyze electrically large systems as usually occurs in this frequency band. The methods are presented in Chapter 5. The methods are based in Quasioptical analysis, Method of Moments and Method of Moments combined with Physical Optics.

Finally, Chapter 6 presents the conclusions of the Thesis and proposes the future working lines.

CHAPTER 2

Planar antennas

2.1 Introduction

Terahertz (THz) band has been in a great expansion during the last decade due to its growing interest for Spectroscopy, Radioastromy, Imaging, etc [10, 11]. The room temperature generation of THz radiation, especially high power signals, has been an issue for all the technologies in this frequency band. From electronics, THz generation has been achieved through microwave technology obtaining a maximum power of 1 mW around 1 THz [67]. On the other side, optoelectronic devices have been developed for THz generation achieving a maximum power in the range of a few μW by photomixing of two laser beams in a semiconductor [68, 69]. Here, different devices based on a photoconductor with short carrier lifetime [70], especially designed UTC p-i-n-diodes [71], n-i-pn-i-p superlattice devices [72] or interdigitated photomixers [68] are used to absorb the optical beating signal and transform it into an AC (THz) current. All these devices operate at room temperature and are widely tunable by tuning the optical frequency of one of the mixing lasers. The design of the antenna has to address the coverage of the desired frequency range and the impedance matching to the photomixer, here after, PM. The output signal is usually radiated by an antenna designed in the THz range [69, 72]. The optimization, design and measuring of the radiating element connected to the PM will be the goal of this Chapter, being out of scope the design of the PM itself.

These feeding structures have strong restrictions in terms of antenna implementation. Typically, they are placed on a semiconductor substrate with a high permittivity ($\epsilon_r \approx 12$). The design of antennas with good performance in terms of radiation efficiency and input impedance that could perfectly match the source (as in the microwave regime) results in a great challenge, especially for broadband radiation.

Planar antennas are widely used in current technologies and are one of the most popular radiation devices due to their low profile, light weight, easiness of manufacturing and integration with other components such as local oscillators [73] or simply feeds on large systems [74]. However, in the Terahertz band, sometimes it is not easy the integration of the radiating element with sources generators of power, such as PMs or diodes, either from photonics or solid state aproximations. For these technologies, implemented in high permitivity substrates with a very high effective thickness, the antenna radiation characteristics are poor, as explained in the introduction of this thesis and given details further on for each type.

In this first chapter, some planar antenas are designed in order to optimize the matching efficiency with PMs [75] and take advantage of all their characteristics such as ultra-wideband behaviour, high tunnability, high delivered power, good efficiency in the Terahertz band [76], and operation at room temperature. The wavelength employed for the lasers is in the 1550 nm band, the most common, due to the easyness in integration and manufacturing, and high tunnability devices available, in the optical communications range. Also the operating regime will be in continuous wave (CW), not being used in this thesis pulsed sources.

Several antenna topologies are employed, so individual characteristics can be optimized to match the properties and techniques of Terahertz devices, materials and manufacturing processes. These topologies include resonant elements, such as half-wavelength dipoles as well as self-complementary antennas, like log-periodic and log-spirals [77]. Other target for this chapter is to be able to achieve the same or higher radiated power (and therefore, efficiency) with smaller elements. The main reason of this goal is the later design of an array with the minimum interspacing possible, which will be limited by the radius of the optical fiber, and not being bounded by the size of the single element. On next sections, more details about the radiating elements employed before this work are given as a reference.

Once the isolated antenna is characterized, in a first approach for the array configuration, only one of the elements is illuminated, but all of them are biased. This is a first step for an imaging array, and it is neccesary to study the behaviour of the system: as the objective is to increase the final radiated

power, on further steps there will be more than one antenna radiating to implement a phased array or sub-arrays with the beam in boresight direction. The technique employed for the illumination of the devices consists on an array of optical fibers placed on a holder, having therefore a fixed distance between fiber centers. Further setup details are given in next sections for each of the array types. In this chapter, only PMs are use to generate the THz signal, as a continuous wave system. The final goal is to increase the radiated power (efficiency) in CW systems employing an array configuration.

Due to the geometrical characteristics of the PMs, the radiating elements must be designed in planar technology, printed over a high permittivity wafer. In addition to the high permittivity, the thickness of the substrate should be large enough in wavelengths to allow the device heat dissipation. Previous conditions lead to a poor directivity due to the EM fields diffusion through the semiconductor substrate. This forces the use of silicon lenses in order to improve the radiation pattern [76] and to act as an interface between the free space and the dielectric.

In all the simulations within this Chapter, only the permittivity is considered in the dielectric constant, i.e. the real part of it. Also, all the substrates are considered with no losses ($\mathrm{Im}\{\epsilon_r = 0\}$).

The work on the current and next Chapter is in the context of a research stage in Max Planck Institute for the Science of Light and FAU to improve the antenna efficiency and to optimize the dimensions of the already in use elements. The previous employed antennas inthe work scope of these institutions will serve as a reference to demonstrate that a miniaturization is possible with the same performance.

The Chapter is organized as follows: first of all, a brief introduction about PMs is presented, including n-i-pn-i-p [78] as well as interdigitated devices [68]. To continue with the topic of this thesis, narrow band (resonating) antennas are presented, such as dipoles, optimized for the use in one single frequency with a relatively small bandwidth. Once the design is optimized, it is introduced in an array configuration, allowing therefore the increase of total radiated power.

2.2 A brief introduction about photomixers

2.2.1 The n-i-pn-i-p photomixer

One of the most commonly used device for THz PMs is the called Antenna Emitters [78]. Continuous Wave (CW) generation by photomixing is based

on the THz-periodic generation of electrons and holes in semiconductors by the absorption of two laser beams with two different frequencies, as given by the formula $f_{\pm} = f_0 \pm f_{THz}/2$. The interference of both beams in the semiconductor composite with the appropiate band gap, results in the THz-periodic carrier generation. The emission of THz radiation using antenna-based emitter is originated from the collective current of the carriers generated within a small area and being fed into an antenna. In order to have successful results after the photomixing procedure, both beams should have the same polarization and electric field amplitude. If the same amplitude is not achieved for both laser beams, the power of the resulting THz wave will be reduced in expense of the performance of the system [75].

To achieve an acceptable THz power level it is required to limit the PM dimensions, smaller than the THz wavelength, reducing consequently the available area where the laser beam should be focused [76] due to the flow of currents inside, as in Fig. 2.1(b). The strongly focused laser beam leads to high carrier and current densities in detrimental to the efficiency of the device, limiting its maximum power available. For this reason, it is very important to design a PM whose dimensions are optimized [75].

Depending on the desired characteristics of PMs for each case, the concentration of the different compounds and number of layers is different. A general-purpose PM employed for THz generation is composed by three dielectric layers lying on a substrate required for heat dissipation. The top and bottom layers or n-layers, consist on a semiconductor material $In(GaAl)As$ with an $\epsilon_r = 12.25$ and a thickness of 400 nm and 600 nm respectively, as depicted in Fig. 2.1(a). These both layers have a conductivity σ of 3000 S/cm. The main layer, is a n-i-pn-i-p layer of thickness 600 nm and with the same permittivity but null conductivity. The substrate needs to be at least 300 μm thick to allow heat dissipation, employing GaAs, with an $\epsilon_r = 12.94$, for these kind of photomixers, depending also on the dark current and the optical power level employed on the experiment [75].

The currents flowing on the device, between top (mesa) and bottom conductor are represented in Fig. 2.1(b). These currents feed the radiating element attached to the device, so as to generate THz power, the small area PM is connected to an antenna that converts the AC current into THz radiation. Different types of antennas can be used for the THz power generation. In the next sections several typologies will be studied.

The designed antenna must be fitted to the PM input impedance, taken into account also the capacitance of the device. These two parameters will have a strong influence on the roll-off factor, given by Eq. (2.1) [75]. In this parameter is not included the effect of the contact resistance, not needed for

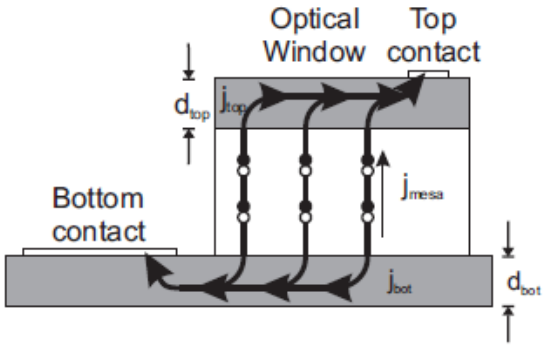

(a)

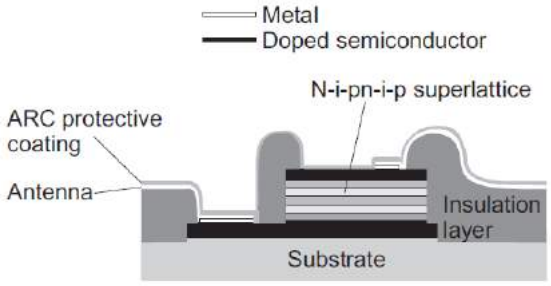

(b)

Figure 2.1: The n-i-pn-i-p photomixer (a) Currents on the PM [75] (b) Cut-thorugh a plasma processed PM.

the analysis accuracy on this case.

$$\nu_{\eta_{RC}} = \frac{1}{1 + (2\pi R_A C f)^2} \tag{2.1}$$

The roll-off factor, limits the power that the whole system radiates, by reducing the efficiency, especially at high frequencies. Due to the increase of the roll-off with the square of the operating frequency, one of the optimized solution is to design the antenna with the lowest possible impedance; this impedance is modelled with $R = 30\ \Omega$ and $C = 15.510^{-15}\ F$ [76]. More about the antenna design related to PM characteristics will be studied in next sections for each particular case of radiating element.

One of the great advantages of PMs is their large tunning range. These devices transform the beat of two lasers into a THz signal, and then into THz radiation with the aid of an antenna. It is enough to tune one of the lasers to obtain the desired frequency, having therefore an ultra-wide band

configuration. Commercial lasers are tunnable over 80 nm at 1550 nm of central wavelength, that corresponds to 10 THz of tunning rage. The roll-off has an important limitation factor, nevertheless, it has been demonstrated an efficient tunning range of 5 octaves [75]. In this case, the limiting factor in the system would be the antenna, that is why almost all systems are employing ultra-wideband elements. Also, resonant antennas are used on these systems for frequency tunning taking the highest power available at a single frequency.

When a planar impedance antenna is used, the reduction in efficiency with the increasing frequency is due to the PM roll-off. In the case of resonant antennas, if we had a resonant antenna for each frequency, they will follow the same waveform envelope for the efficiency as in broadband antennas but with higher level, given by the peaks at the tunned frequencies.

Another good advantage of these PMs is their high integrability: as they are semiconductor-based, they can be orders of magnitude smaller than any other Terahertz sources. Also, they can work at ambient temperature, not needing a cryostat like quantum cascade lasers [4], simplifying the experiments.

As PMs have many advantages, like room-temperature operation and ultra-wide band operation, they also have a great disadvantage for antenna design: they need to be manufactured over high permittivity substrates such as InGaAs, mentioned before, or GaAs due to heat dissipation and substrate properties, and explained in the introduction of this thesis.

2.2.2 The interdigitated photomixer

The interdigitated PM also converts the beat of two laser signals into AC current, feeding an antenna integrated with the device. Most of the antennas employed in this setup are designed to be either resonant or high input impedance antennas. The reason is that these kind of PMs have a very high impedance, so for being able to achieve a considerable efficiency, the antennas should be matched [68, 79].

These devices are manufactured in LT-GaAs or a similar semiconductor as InGaAs, and they have the same issue in terms of high permittivity substrate as n-i-pn-i-p PMs. In the scope of this thesis, the author will present a new antenna topology in Chapter 4, where more about this photomixer will be explained for the application developed.

2.3 Measurement setup

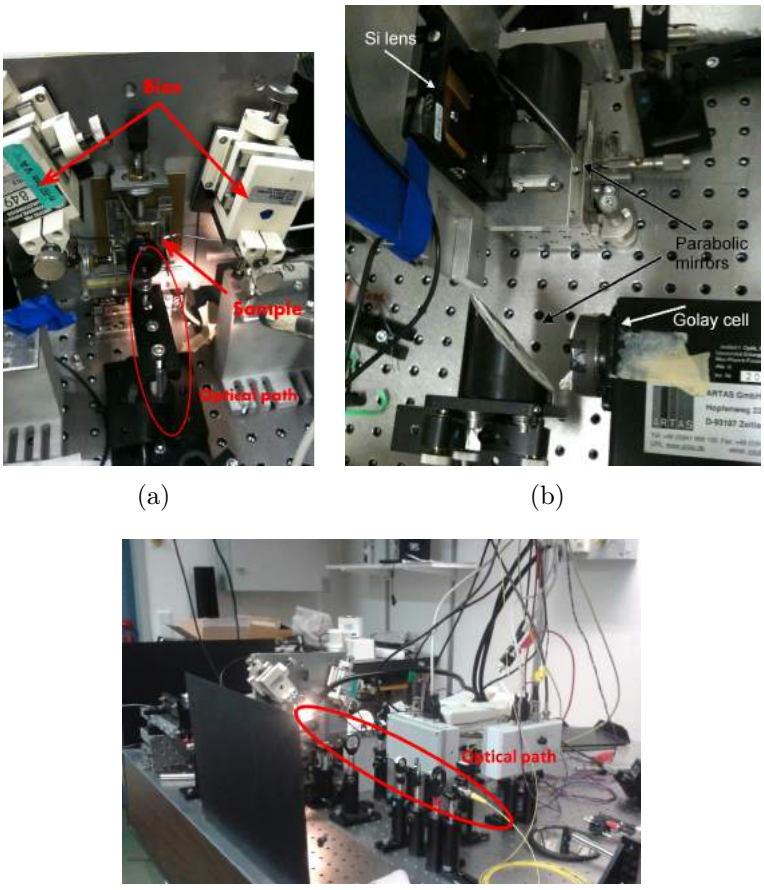

(a) (b)

(c)

Figure 2.2: Setup for THz antenna measurements: (a) Bias feeding and (b) complete setup.

In this Section, the measurement setup for the PM devices is detailed. It applies both to the current Chapter and also to Chapter 3.

To generate the THz signal, two lasers are employed, one is fixed with a 1545.9 nm wavelength while the second is tunnable between 1546.5 nm and 1558 nm in steps of 0.05 nm. The obtained frequencies will range from 66 GHz to 1.497 GHz (in steps of 6 GHz), due to the limits of the amplifiers. Beyond this frequency, the amplifiers are not behaving in linear regime and they generate noise due to espontaneous emission, so the PM is not illuminated properly.

Also, two polarizers are used to achieve the same amplitude and phase

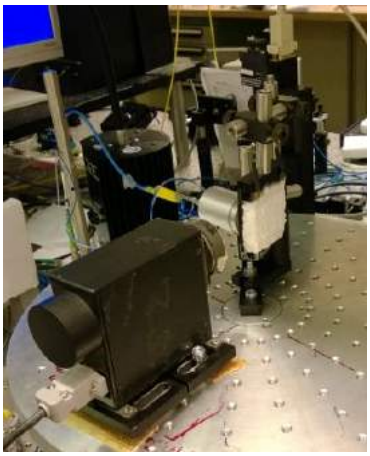

Figure 2.3: Setup to measure the radiation diagram

for both lasers. In all the measurements, a Si lens focus all the power into the focal point of a parabolic mirror, initial component of the system that directs all the power into a Golay cell, measuring all the radiated power with the aid of a lock-in amplifier as in the image in Fig. 2.2(a). The parameters of the Golay cell and the mirrors are attached in Appendix 6.2. Two needles are used for providing DC bias to the photomixwer through the antenna arms. The placement of the sample containing the PMs and the antennas, together with the bias devices and the optical path, is illustrated on Fig. 2.2(b). Also, in Fig. 2.2(c) it is shown the path for the laser on the setup.

All the devices will be set to a photocurrent A of $\approx 3\ mA$. The output power for each laser is tunned between 200 mW and 400 mW (power in the PUMP diodes) to adjust the photocurrent. To compare the effciiency of the devices and antennas with diferent geometries, the figure of merit P_{THz}/A^2 is shown in the figures. The power collected by the Golay cell is normalized to the photocurrent on the PM, also in terms of power, so no influence of the illumination of the devices is on the results and therefore the antenna performance can be evaluated.

A different setup is employed to measure the radiation diagrams of the antennas. In Fig. 2.3 the Golay cell is placed directly in front of the sample, without any parabolic mirrors to gather up all the power in a single point (focus of the mirror). The distance between the Golay cell and the sample is $\approx 9\ cm$. The resolution for measuring the beams with this setup is 3.17°, computed with the distance between the sample and the phase center of the Golay cell and the step of the sample holding. The patterns can be measured up to 400 GHz, due to the low power radiated and the sensitivity of the

Golay Cell.

2.3.1 Dielectric lenses

In these kind of systems is very extended the use of dielectric lenses to act as an interface betweeen the substrate and the air. With the antenna printed over InGaAs, most of the radiation is trapped on the substrate, due to the much lower radiation resistance of it ($Z_0 \approx 377\ \Omega$ vs. $Z_{substrate} \approx 104\ \Omega$). By the use of a high resistivity Si lens, the refraction index is similar to that of the substrate, so it prevents total internal reflection and energy diffusion due to the high mismatch in impedance between air and dielectric. This effect will be carefully explained in Chapter 3, where the substrate topology is optimized for avoiding this diffusion of energy.

The lenses employed in the experiments on the current Chapter are Tydex Si high resitivity half spheres with a dimater of 10 mm and a slab 700 μm thickness. It serves only as an interface between high permittivity material and air, having no focusing properties due to the hemispheric shape (with no dielectric slab comparable to the radius). In this way, the radiation pattern from the antenna+lens will be the same as for the antenna, but with no reflections on the air-InGaAs interface [80], allowing the study of the real radiation properties of the designed system.

Another important consideration is the Brewster angle. Due to the fact that with this type of antennas the beams have a broad 3 dB beamwith, it is desirable to take that into account, so the Brewster angle is higher than this beamwidth, and no more power is lost. For the air-Si interface, the Brewster angle is 74.5°, so the power contained in the beam out of the limits of that angle will be totally reflected by the Si-lens.

All the devices manufactured are represented on Appendix 6.2 with the mask employed in the processing. There are different types of antennas as well as PM devices. All the elements and their respective features and dimensions will be defined on the corresponding sections on this Chapter.

2.4 Log-spiral antennas

The log-spiral antenas are self-complementary antennas when designed with specific parameters such as the proper arm length and width. The most important characteristic of these antennas for this thesis is the constant input impedance (theoretical) not depending on frequency [77], when both the width of the arms and spacing between them are equal. Nevertheless, as

self-complementary antennas, they are supposed to be infinite but due to practical reasons they always are truncated, so the input impedance could not be constant over an infinite bandwith, both in the high and the low band. The truncation has effects on the low frequency limit, where the size of the element is comparable to the wavelength and the energy spreads throughout all the structure; at high frequencies, the limitation is due to the source feed itself because of the roll-off and also to the truncation of the spiral on the inner side to place the feed. The theoretical self-complementary impedance for InGaAs is $Z_0/2 = 16.7\pi\ \Omega$ (52 Ω), being Z_0 the characteristic impedance of the medium.

The main goals of this section are to improve the radiation efficiency by means of the improvement of the matching of the antenna to the PM, that is, to optimize the input impedance, as well as the radiation resistance to reduce the roll-off factor as much as possible, given by Eq. 2.1.

Also, another goal is to design an element as small as possible (without the DC bias filters) to implement it in arrays together with new substrate geometries detailed in next chapter, without loss of efficiency and therefore radiated power. The main design parameters for these antennas that sould be taken in consideration are: the radiation resistance, the input impedance and the losses in the dielectric materials. The feeding region should also be as symmetric as possible in order to have both arms of the log-spiral fed with completely symmetric currents.

All the simulations for these devices have been done with Microwave CST Studio [81]. The simulations were done setting an infinite InGaAs substrate, without losses as background properties of the simulation parameters, with a slab of air on top of the antenna. In this way, not only the effects of the thickness of the substrate are taken into account but also the lens performance, assuming its simulation as a semi-infinite substrate. It is acting as an interface between the high permittivity substrate and the air.

2.4.1 Single Elements

The first step is to simulate the single element in an isolated configuration. For this purpose, as mentioned before, the settings of the simulation should have been set to have as background material the InGaAs while the air is simulated with a slab on the opposite side of the antenna. In this way, the effect of the hemispherical lens is emulated as an infinite substrate. For the antenna excitation, the author employed a lumped port, agreeing with the PM input impedance at 1 THz.

The analytical expression of a log-spiral is defined by $r = k\exp(a(\phi - \delta))$ [82], where ϕ defines the number of loops of the spiral (i.e. 2π is a complete loop), k is the initial radius of the spiral, a is the growth rate and δ is the displacement between both arms. The second arm, has the same expression with the only difference that ϕ is shifted by π to obtain opposite arms.

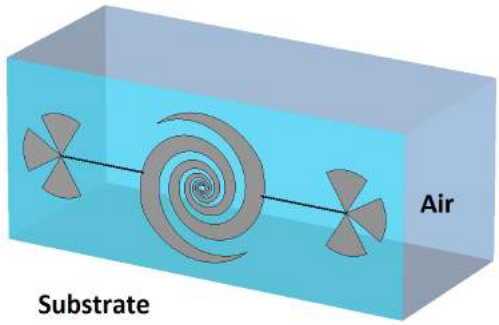

Figure 2.4: Single spiral simulated with CST.

One of the simulated log-spirals is sketched in Fig. 2.4. The arm terminations serve as an attenuator to reduce the backward waves at the end of the antenna, so no reflections back to the PM occur. The principle employed here is that the EM field is continuously attenuated due to the change of impedance of the equivalent transmission line. The connection pads are also a filter for the RF signal, not allowing the radiation from them; they behave as an open circuit in RF due to their characteristic impedance. In Fig. 2.4 it can also be appreciated the simulation background, what is set to air and the semi-infinite dielectric of high ϵ_r.

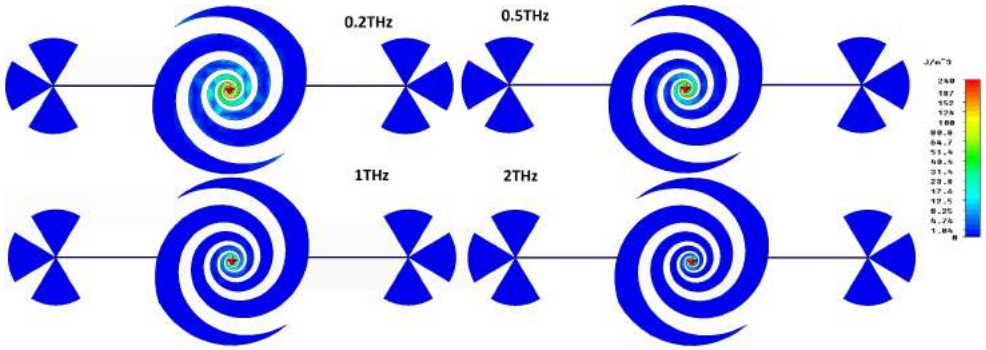

Figure 2.5: Electric Energy distribution in a log-spiral for different frequencies.

The distribution of the electric current density depending on the frequency is represented on Fig. 2.5. The EM field is concentrated on different

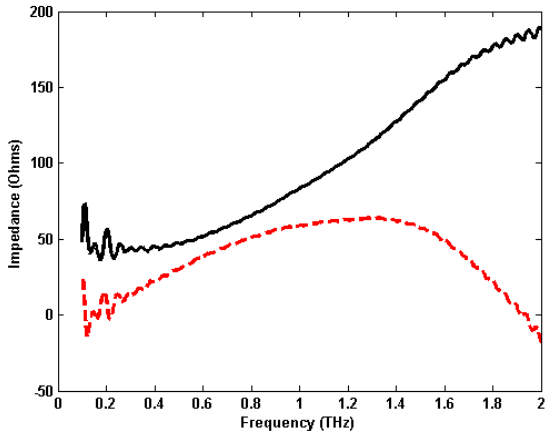

Figure 2.6: Input impedance of the CI-2 device, real (black-solid) and imaginary (red-dashed) parts, in Ω.

sections of the antenna arms based on the frequency simulated. The device under study for this case is CI-2, represented on the mask in Appendix 6.2. As the excitation goes up in frequency, the electric current density is more concentrated in the inner sections, where the dimensions are comparable to the wavelength. It is important to note that even for the lower frequencies ($\approx 0.2\ THz$) there is no coupling of the EM field to the DC bias pads. Regarding the planar impedance properties, in terms of electric current, this structure behaves as an infinite structure, at least, for the higher frequencies.

The input impedance is also simulated, and shown in Fig. 2.6, both the real and the imaginary parts. The impedance is oscillating up to 200 GHz, due to the total electrical dimension of the spiral: the wavelength at 200 GHz in an InGaAs substrate is 434 μm, while the total diameter of the spiral (CI-2) is 408.52 μm, so each arm is aproximately half wavelength, the self-complementary properties asume an infinite length, so the arms start to resonate at lower frequencies in the wavelength dimensions. From 300 GHz, the real part grows with a linear shape, up to 1.6 THz, where it starts to oscillate again: this effect is due to the truncation in the core sector of the spiral.

Previous works with the n-i-pn-i-p PM also employed log-spiral antennas [75]. These antennas will serve as a reference to compare the improvement in radiated power of the ones designed during this thesis. The measurements will be compared further in this Section. The design parameters of the reference spiral are: total diameter 1.19 mm (14.3 λ_r, $\lambda_r \approx 83.56\ \mu m$ at 1 THz), with 3π loops. These reference antennas correspond to the spirals marked as SC-#

Table 2.1: Parameters for the log-spiral antennas designed

Antenna number	Max. Diameter (μm)	k	a	δ	Max. ϕ
$CV-1$	305.94	6	0.2	1.8	5.7π
$CI-2$	408.52	8	0.2	1.8	5.7π
$EIV-2$	147.18	3	0.2	1.8	5.7π
$EIII-4$	204.26	4	0.2	1.8	5.7π
$EV-2$	305.94	6	0.2	1.8	5.7π
$Reference$	1174.62	–	–	–	3π

and SE-# on the mask in Appendix 6.2.

The parameters of some of the designed antennas are specified on Table 2.2, together with the reference. Each of the numbers corresponds to the number on the mask in Appendix 6.2, and also to the measurements shown on next Section.

Two examples of the proccessed antennas are shown in Fig. 2.7, with different arms width.

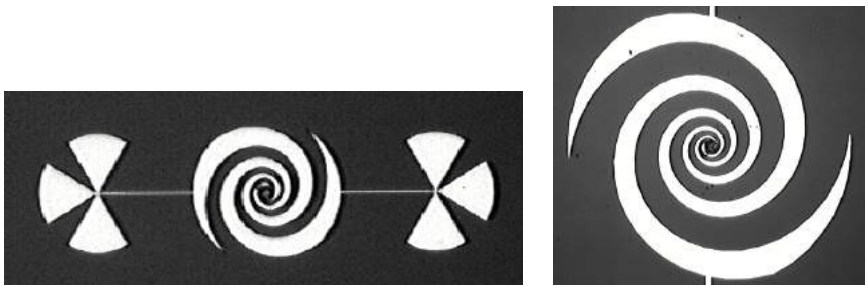

(a) (b)

Figure 2.7: SEM pictures of two log spiral antennas (a) with the bias filters and (b) detail of the spiral.

Different log-spiral designs have been measured, contained in mask number 1 attached in Appendix 6.2. The setup employed for the measurements was described in Section 2.3 on this chapter. To show the obtained results, the efficiency is compared to the reference antenna, implemented on the same wafer with the same PM devices. All the devices are fed with a 3 mA current on the laser, obtaining the maximum efficiency.

Two different sets of spirals are characterized in this thesis, set E and set C. The difference between both of them is the geometry on the PM window

for fiber illumination and the isolation for the litographic proccess between the antenna gold and the connection pads of the PMs [76]. The results are compared to their respective device with the reference spiral. The data shown in the figures are the THz efficiency of the system, measured in terms of P_{THz}/A^2, being A the photocurrent on the PM. This current is tunned with each of the lasers power to be set in 3 mA. An optimum polarization point was found for each measurement (DC bias).

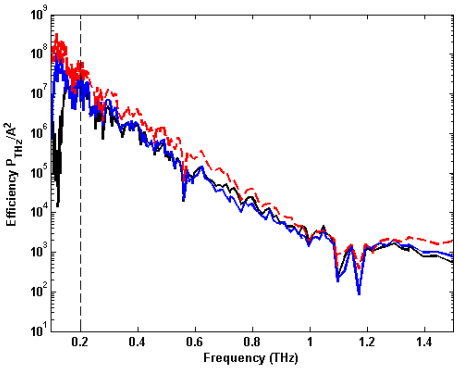

(a)

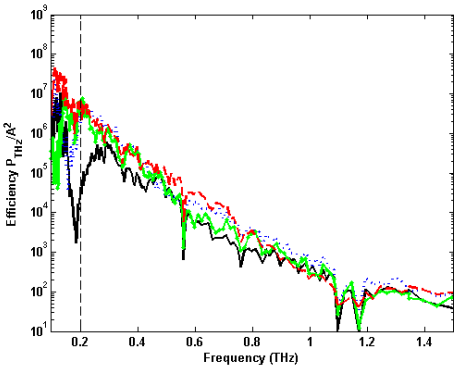

(b)

Figure 2.8: Measurements for different spiral antennas with two different PM topologies, reference antenna in dashed red.

Regarding Fig. 2.8(a), two different antennas are measured to compare them with the reference, with the device labeled C. In this case, the efficiencies for the three devices are similar, especially beyond 200 GHz, which is the low frequency limit of the antenna. The device represented with a blue line, corresponds to CI-2, while the spiral in black is CV-1. The second one is slightly smaller having therefore a higher cut-off frequency in the low limit.

This efficiency is above reference at some especific frequencies, not having significant difference. It can be considered that the performances are equal.

For the case of E devices, represented on Fig. 2.8(b), the results and conclusions are the same as for the previous case. The blue dots correspond to device EIII-4, green line is EV-2 and EIV-1 is the black solid line. This last device is also the one that will be employed for the array measurements on next Section. From this point, a device is the combination of antenna+PM. As for the previous case, the efficiency of the new designed antennas is close to the reference: the lower cut-off frequency for the smallest component is higher than for the other samples due to the miniaturization.

For both cases, the roll-off factor of the PM itself has a strong influence. The drop in the efficiency, and therefore, in the radiated THz power is of 5 orders of magnitude in the whole band. The high and low peaks in efficiency, that appears in all measurements are due to PM non-linearities and not to the antenna.

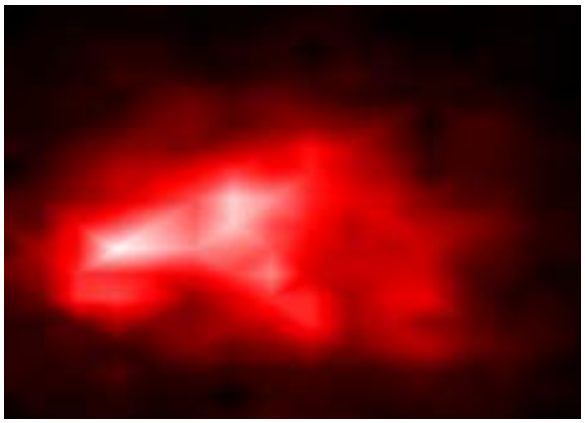

Figure 2.9: Radiaton pattern for the isolated element.

The radiation pattern for the single element EIV-1 has also been measured for comparison purposes with the array on next Section. The pattern is shown in Fig. 2.9. It is important to note that the precision to measure the pattern is low, and the beam is diffracted in a short distance, as detailed in Section 2.3. The measurements are done without any of the parabolic mirrors, gathering all the power in the Golay cell directly from the lens. The pattern shows one absolute maximum, and a high side lobe. This shape can be due to reflections on the measurement setup together with the low precision, as simulations do not throw these results either in Electric Energy distribution, in impedance terms or radiation pattern.

From both sets of measurements it can be concluded that a miniaturiza-

tion of one order of magnitude has been achieved for the same PM devices. This is an important achievement taking into account the future array implementation. Also, not only for the arrays but for the different substrate geometries that will be designed in Chapter 3.

2.4.2 Arrays

Having designed some optimized single element antennas in previous Section, achieving an important miniaturization compared with the reference spiral, the goal now is to increase the radiated power by designing an array of log-spirals. The interaction between the elements in form of mutual coupling either by radiation or by surface waves due to the high permittivity substrate is brought in line.

To design the array, several constraints must have to be taken into account beside the single element efficiency, like the minimum distance between elements, limited by the optical fiber diameter and therefore the positioning of these fibers. The diameter of the fiber is $D = 125\ \mu m$, allowing a minimum inerspacing of $D_{min} = 150\ \mu m$. For this first case, the minimum inter-element spacing is set to 160 μm.

Figure 2.10: Array of spirals.

The first stage on the array designing is the implementation of an *imaging array*. The basic configuration is: only one element will be illuminated with the lasers at the same time, therefore only one PM will be emiting. With this configuration, the mutual coupling between the elements [83] can be easily analyzed, as one antenna is emitting while all the other PMs are polarized, having therefore a dark current ($\approx 10^{-9}\ mA$) flowing through them with an active input impedance, as is defined in [84, 85]. Despite the system is in an emitting configuration, as the antenna elements are reciprocal, the results obtained can also be applied to a receiving configuration according to the reciprocity theorem [86] in terms of radiating element. However, this can not

be applied for n-i-pn-i-p devices, as at this moment they are unable to work in a receiving configuration.

The array presented in this section is a 5×5 array, so different situations for mutual coupling can be studied for later experiments. The corner 3×3 array has been measured, while the other elements can be considered symmetrical. On each measurement, only one antenna is illuminated with the two lasers, but all the other PM are biased. That means that there is some dark-current on them, but they are not generating any THz signal. This can be a simulation of the behavior of the system in an imaging array configuration.

The measurements for each of the elements together with the reference (isolated EIV-1) antenna are presented on Fig. 2.11. The position of the devices (Fig. 2.10) depends on the color: row number 3 is always represented in black, row 4 in red and row 5 in blue, while column 3 is solid, column 4 is starred and column 5 is dotted. The element number is also indicated in Fig. 2.10. For example, due to symmetry, the element $[4, 3]$ (black, starred) should be the same as the $[3, 4]$ (red, solid), which is the case in the measurements. This also serves as checking for the repeatability of the measurements.

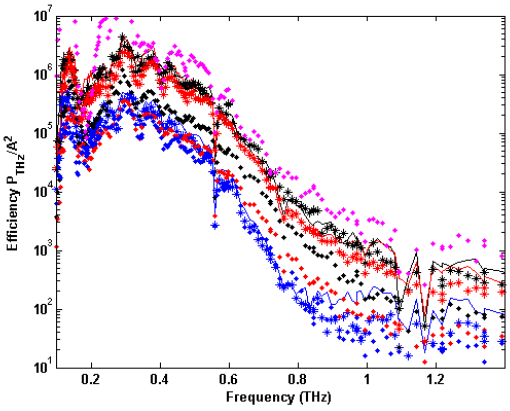

Figure 2.11: Measurements for the array of spirals of 5×5 elements.

Regarding the comparison with the isolated antenna (EIV-1), in dotted pink, the central element ($[3, 3]$) has the most similar performance, with no significat difference; this is also the case for the elements wich are embedded on the array (no edge elements). For the case of edge elements, the efficiency is slightly lower, having here a stronger effect regarding mutual coupling, or at least, with no symmetric geometry.

It is important to note that the Si-lens has not been refocused, being the

edge element of the array in an out-of-focus position in the system, having therefore a reduction in the efficiency in terms of lens focusing.

Another important consideration that should be taken into account is the low cut-off frequency limit of the element. While for the single device this frequency was beyond 200 GHz, in this case the operation band is broader than before. This effect is a well known mutual coupling consequence [87], already studied in travelling wave antennas: in an array configuration, one can design the elements with a smaller size in terms of wavelength due to the aperture efficiency of the whole system.

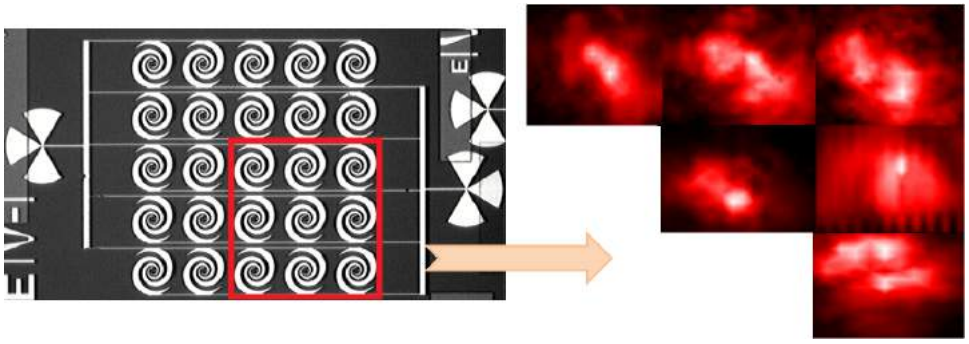

Figure 2.12: Radiaton patterns for the spirals array.

The radiation patterns have been measured at 300 GHz. For this measurement, the parabolic mirrors are not employed, as represented in Fig. 2.3, so the beam is not distorted, and the real pattern radiated by the device is shown; the hemispherical lens is not introducing any focusing distortion on the system. The Golay cell is rotated to measure the pattern shown in Fig. 2.12. Only the shape is measured for this case, to check the distortion for each of them. Also, the symmetric elements are not measured, having therefore 6 different patterns. It is important to remember that the precission for this measurements is not as accurate to differentiate correctly where the side lobes are and the nulls, but it is enough to give an idea of the patterns for an imaging configuration.

2.5 Log-periodic antennas

Another type of broadband devices designed are the log-periodic antennas. The goal is the same as for spirals, to achieve the maximum possible power with an array configuration. This Section is divided into single elements, including measurements, and the arrays designed.

Table 2.2: Parameters for the log-periodic antennas designed

Antenna number	Max. Diameter (μm)	$\#arms$	R_{first} (μm)	τ	σ
$EX-3$	300	7	150	0.5	$\sqrt{2}$
$E5-4$	200	4	100	0.7	0.87
$Reference$	710	5	355	0.7	0.7

2.5.1 Single Elements

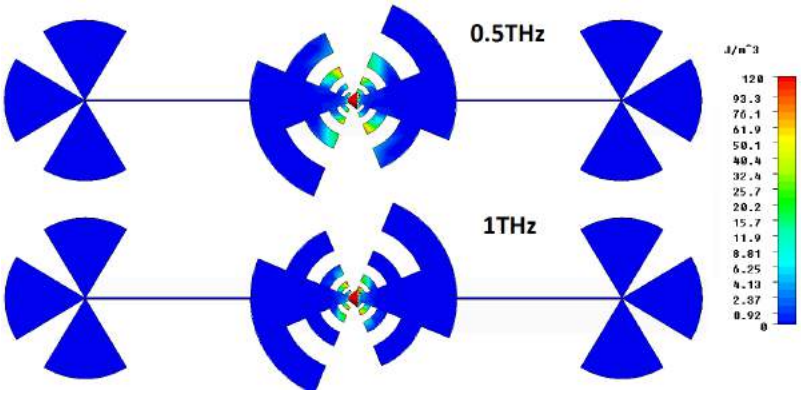

Figure 2.13: Electric Energy distribution in a log-periodic antenna for different frequencies.

As well as for the case of spirals, with the appropiate design parameters, they are self-complementary antennas [77]. The feeding region, where the PM is implemented, is also designed the most symmetric possible for the excitation of both arms on the same way, due to the complementary geometry of the arms. One of the simulated devices is shown in Fig. 2.13 together with the electric current density distribution. Also, the feeding lines are included on the simulation, to check their behavour as an RF choke. The simulation technique for modeling the lens as a semi-infinite substrate is also employed in this case.

Most of the power will be concentrated close to the PM, as swhon in Fig. 2.13. The substrate employed is also InGaAs, and they are implemented on the same wafer as the spirals fom previous Section, through the same manufacturing process, so the power obtained can be compared.

The designed devices, are compared in simulation with a reference device, already tested [76]. The design parameters of the log-periodic element are the number of arms, the first arm width, σ (ratio between the radius of the arm

(a)

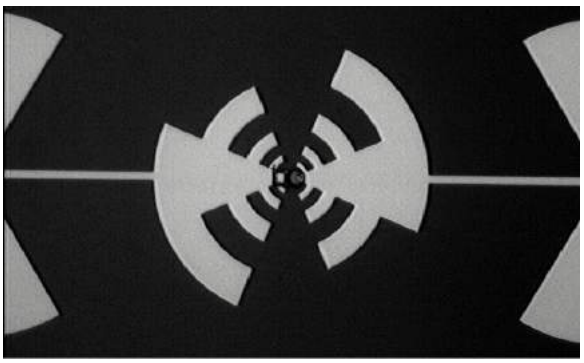

(b)

Figure 2.14: SEM pictures of two log periodic antennas (a) for a wide band of frequencies and (b) for a more restrictive and lower frequencies

and the spacing with the next one), τ (ratio between n and $n+1$ arm), as well as the total radius and the angle of the bow-tie in the center [77]. For the designed devices, the parameters are listed in Table 2.2.

The setup for the measurements of the log-periodic antennas is the same as for the spirals in previous sub-Section. For the single element case, two devices are shown together with the reference in Fig. 2.15. The difference in efficiency is almost null, only the smaller device, for which the cut-off frequency is higher as for the larger device. The solid blue line corresponds to the EX-3 device on Appendix 6.2 while the solid black matches the E5-4 element. A miniaturization of the element has been achieved too, with the aim of employing it in further array designs.

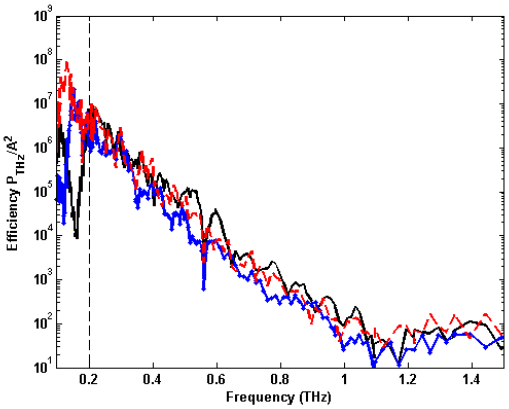

Figure 2.15: Measurement of different log-periodic antenna devices

2.5.2 Arrays

With the use of the element E5-4 measured in previous Section, another array has been designed this time with log-periodic elements. The spacing between each device is 210 μm, and all the PMs are biased while both lasers are focused on one of them with the optical fiber. This will allow the comparison of the spiral vs. log-periodic as well as the suitability for an imaging or a phased array. A SEM picture of the physical array is shown in Fig. 2.16, while the measurements are in Fig. 2.17.

The array is also in a transmitting configuration, but the results can be extrapolated to a receiving system to apply it to imaging arrays regarding antenna elements. Also, with transmitting configuration, the results are useful for a later implementation of a phased array regarding mutual coupling.

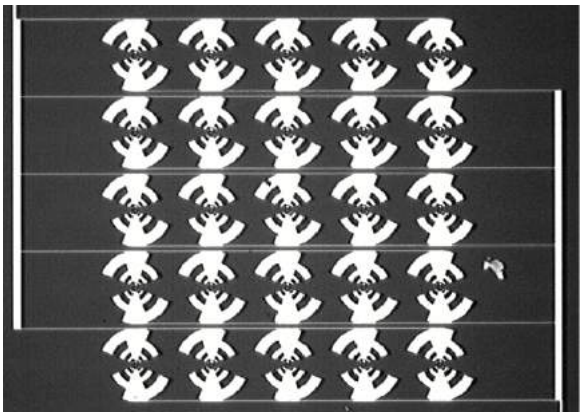

Figure 2.16: Array of logperiodic antennas.

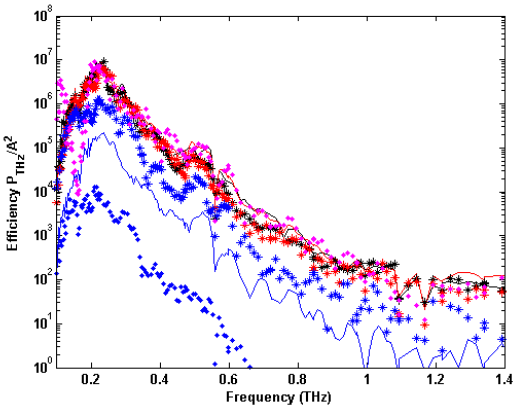

Figure 2.17: Measurements for the array of log-periodic antennas of 5×5 elements.

Not all the measurements for all the elements are shown in this case for the shake of clarity on the figure. As some of the elements are symmetrical, only one of the instances is depicted. It has been checked that the symmetry is kept the system as well as for spiral arrays, so the repeatibility of the measurements is also confirmed. As well as for the spiral antennas, the central elements are behaving as the single element isolated, while the edge antennas have their efficiency reduced. For this case, the effect is stronger as for the case of spirals, this can be due to a misalingment of the lens, as the strongest effect can be appreciated specially for the corner element.

2.6 Dipole antennas

To continue with the optimization of shapes adapted to the PMs, also narrowband antennas have been designed with the aim of impedance matching at least at a single frequency. The element employed is the half-wavelength dipole, already known in this type of devices due to the easiness of fabrication and the conjugate matching adaptation to these devices. For this element, only single devices have been designed, as the goal is to optimize the efficiency by means of the conjugate matching technique.

The main problem arised for this design is the impedance characterization of the device itself, changing with the DC bias, as well as whith the laser power and the mask processing. The equivalent circuit employed is the one provided by [76].

Different antenna elements have been simulated in order to apply the conjugate matching technique, as the impedance changes in the PM depending

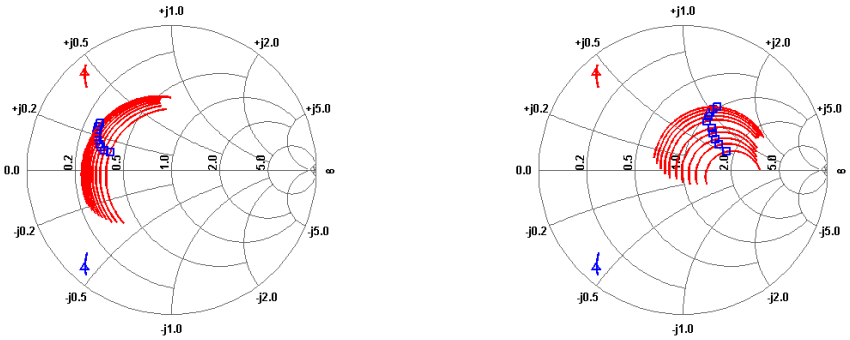

(a) (b)

Figure 2.18: Input impedance of the PM and matching conjugate, and parametric impedance varying the transmission line width (a) for a line length of 32 μm and (b) 45 μm, normalized at 50 Ω.

on the current [76], both varying the geometrical parameters of the transmission line from the dipole to the photomixer or by adding a reactance or capacitance on each case. All the dipoles have been designed to resonate around 600 GHz.

The characterization of the PM is described in the introduction of this Chapter, in Section 2.2.1. In Figs 2.18(a) and 2.18(b), two different parametric studies with a variation in the CPS transmission line between the PM and the dipole are shown. The set of curves represent a variation in the transmission line width with the point at 600 GHz represented with an square marker. The two impedance points with a triangle are, with negative reactance the input impedance of the PM and with positive reactance the matching conjugate, the goal impedance to achieve.

In Fig 2.18(a), the variation of the line width goes from 2 μm to 11 μm, choosing the last value for manufacturing as it is the closest to the matching conjugate of the PM. Due to manufacturing constraints in line width and gaps, it was decided not to introduce any stub to completely match the impedance, as the PM is not fully characterized, and it changes with frequency and with the type of semiconductor where it is processed.

To design the dipole, the equivalent circuit from [76] has been taken as a reference. The expected results are that the efficiencies, whatever is the design frequency, follow the envelope of the efficiency on broadband shapes (due to the roll-off of the PM) with an enhancement of the power in the resonating frequency due to the matching impedance. For each of the systems, it is added an RF choke filter, to polirize with a DC bias the PM. The size of

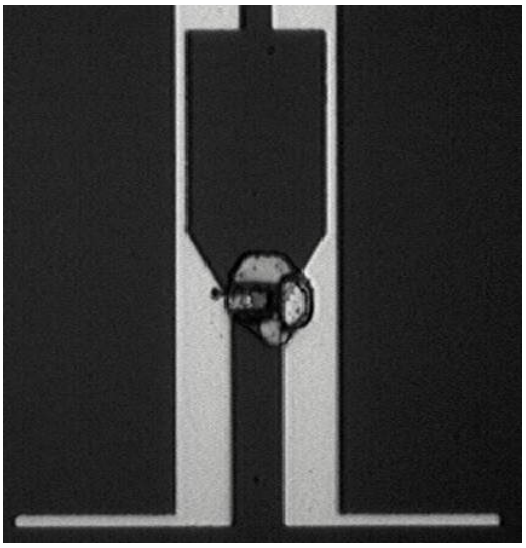

(a)

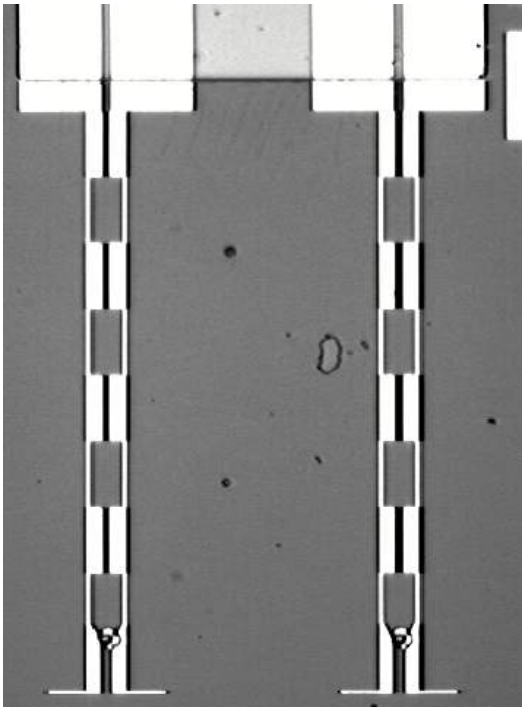

(b)

Figure 2.19: SEM pictures of dipoles (a) detail of a single dipole (b) two dipoles with their respective DC filters.

the measured dipole measured is 90 μm, aproximately half-wavelength at 600 GHz.

The setup for the measurements of the dipoles is the same as for previous Sections, employing also equal lens and mirrors. There have been measured two different devices as well as the reference spiral antenna to compare the results in Fig. 2.20.

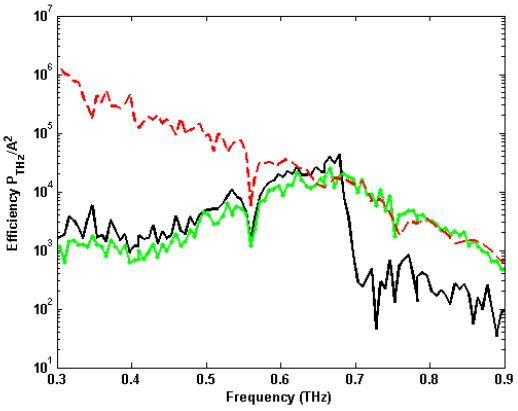

Figure 2.20: Measurements for two designed dipoles including the reference antenna.

The efficiency for the dipoles is lower than for the reference antenna, as expected, for all frequencies but for 680 GHz. Despite the design frequency was set in 600 GHz, the resonance has shifted. This shift can be due to the manufacturing imperfections, as well as to a change on the impedance due to the current on the PM. For both devices, corresponding to the labeled as E2 and E1 in Appendix 6.2, the efficiency is higher within the resonant frequency band, being demonstrated the expected behavior.

2.7 Conclusions, future lines and contributions

In this Chapter three types of antennas, two broadband and one resonating, have been presented with the aim of improving the efficiency on the range of the THz band and reduce the antenna dimensions for further developments. Both goals have been achieved regarding the single elements and also for the array configurations.

For the single elements, a reduction of one order of magnitude in the size of the antenna has been achieved, demonstrating the properties of the self-complementary antennas without a decrease of the efficiency in terms of

radiating power. This allows the implementation of an array configuration, with the possibility to illuminate both as an imaging array or as a phased array.

The possibilities for a continuation of this work are extended through a wide variety of lines. This is a demonstration of how to apply the current technology in the Terahertz range to classical array theory, thus, almost every research line in array theory could be applied to the Terahertz band, for example, beamforming: allowing the corresponding phase delays on each of the fibers, electronic scanning techniques can be applied to these working frequencies in a phased array.

Also, the interspacing of the different elements can be modified in order to create for example, a sparse array to reduce mutual coupling between elements. This is of special importance in broadband arrays, composed of log-spirals or log-periodic elements, where the size of each device is comparable to λ.

A straightforward configuration is the illumination with several optical fibers more than one PM, having therefore a phased array. If all the fibers are in phase, broadside radiation occur, having therefore a higher radiated power. Also, by changing the phase of each element consequently with the scanning angle, an scanning phased array is possible. These measurements are being performed nowadays in FAU (Friedrich-Alexander-Universitat Erlangen-Nurnberg).

The contributions of the content of this Chapter to international journals, conference papers and research stages are:

- A. Rivera-Lavado, L. E. García-Muñoz, S. Bauersmidth, S. Preu, S. Malzer, G. Dohler, B. Andrés-García and D. Segovia-Vargas, "Arrays and New Antenna Topologies for Increasing THz Power Generation Using Photomixers", *Journal of Infrarred, Millimeter and Terahertz Waves*, vol. 34, no. 2, January 2013.
- B. Andrés-García, L. E. García-Muñoz, S. Bauersmidth, S. Preu, S. Malzer, G. Dohler, L. J. Wang and D. Segovia-Vargas, "Gain Enhancement by Dielectric Horns in the Terahertz band", *IEEE Transactions on Antennas and Propagation*, vol. 59, no. 9, September 2011.
- Research stage during 5 months in Max Planck Institute for the Science of Light, May-September 2010.

CHAPTER 3

Dielectric Horns

The goal of this Chapter is to employ the antennas designed in Chapter 2 to fullfil the requirements for THz optimization and increasing the good radiation properties of the system as well to take advantage of the beam confination. The structure proposed is based on a horn antenna etched in the substrate and fed with a planar printed radiating element used for generation of terahertz radiation, designed for the 100 GHz to 2 THz range. For the proposed geometry, the energy distribution through the substrate is reduced towards an increase in the gain of the system of at least, 8 dB in a $1:10$ bandwidth. The structure has been measured showing the expected behavior in the low band.

During the last years, several techniques have been developed to optimize the radiated power, especially, at room temperature, employing photomixers. These techniques have been based either on the antenna gain increase [64], or in a a reduction of the matching loses [76, 64], the technique also employed in previous Chapter. As the photomixers are broadband devices, although their roll-off factor [72] strongly limits the output power, the main limiting constraint, in terms of bandwidth performance, is usually the antenna.

The mandatory use of a Si lens, forces the technology to evolve in a more efficient way, taking advantage of the thick substrate and design new shapes that maximize the efficiency.

The joint effect of the lens use drawbacks and the lack of high gain or large power generation devices for the THz range in planar technology is the

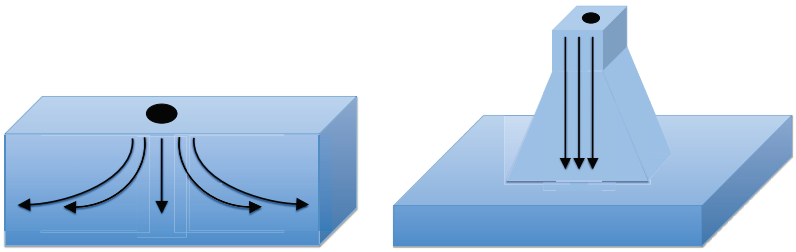

(a) (b)

Figure 3.1: (a) Energy distribution on a high permitivity substrate (b) proposed structure with the antenna on top.

driving force for new structure designs for the outcoupling of the generated THz radiation.

One example of these new structures is the use of micro-machined horns, fed with printed antennas over membranes, working in the millimeter wave regime [88]. In this example, the micro-machined horns are metallic air-loaded horns. They are also based on the idea of focusing the THz radiation to increase the final system gain.

From another point of view, the properties of antennas based on dielectric filled waveguides are well known. These structures reduce the energy spreading in the material, guide the power in a high efficient way, and feed the dielectric loaded horns or dielectric horns [89, 90, 91, 92].

Dielectric filled-horns have been widely studied [89, 90, 91, 92], as well as dielectric waveguides [86] in the previous years. These studies show good results in terms of cross-polarization levels, allowing a reduction in the size of the horns as well as the elimination of corrugations to achieve symmetric radiation patterns and good beam characteristics with a broad bandwidth. The use of semiconductor substrates can open new ways for implementing planar printed antennas in the THz range.

A dielectric semiconductor horn antenna etched on a high permittivity and thick substrate is proposed to focus the radiation, reduce the energy distribution and enhance the gain of the device in the broadside direction in the THz band. A sketch of this process is shown in Fig. 3.1. In the first case a conventional system is depicted, where the radiation has a strong diffusion through the substrate. In order to overcome this issue, a horn antenna is etched into the semiconductor as shown in Fig. 3.1(b). The energy diffusion is reduced in the substrate, focalizing all the radiation into the broadside direction.

The large thickness of the substrate and its high dielectric permittivity are now used in advantage to increase the efficiency of the dielectric horn in the THz range. For the experimental realization, the antennas are fed by n-i-pn-i-p photomixers [76], which provide high power at room temperature. This new structure also allows the use of a dielectric lens in the mouth of the horn, with which higher gains can be achieved with higher directivity and also eliminate reflection losses due to the dielectric-air interface.

This Chapter is organized as follows: in Section 3.1 theoretical results for the dielectric waveguide and horn are presented, while in Section 3.2 the results are particularized for the excitation of the system by an antenna. In Section 3.3 the experimental results and fabrication process are shown.

3.1 Dielectric waveguide and horn

3.1.1 Propagating modes on a dielectric waveguide

First of all, the modes propagating in a dielectric waveguide at THz frequencies (the minimum operating frequency will be 100 GHz) are calculated. A modal chart is represented in Fig. 3.2. It corresponds to an asymptotic case of a dielectric waveguide directed along Z, based on the assumption that the dimension in the X axis is infinite while the Y direction has the thickness of the substrate, h. The curves of Fig. 3.2 are the results of solving the characteristic equations (3.1) and (3.2) for β_y (propagation constant) and α_y (attenuation) for TE and TM modes respectively (even and odd) for a dielectric waveguide of InGaAs ($\epsilon_r = 12.9$) and $a = 180\ \mu m$ according to [86] at 200 GHz.

$$\begin{aligned} \alpha_y &= \frac{\epsilon_0}{\epsilon_d}\beta_y tan(\beta_y h) \\ \alpha_y &= -\frac{\epsilon_0}{\epsilon_d}\beta_y cotan(\beta_y h) \end{aligned} \tag{3.1}$$

$$\begin{aligned} \alpha_y &= \beta_y tan(\beta_y h) \\ \alpha_y &= -\beta_y cotan(\beta_y h) \end{aligned} \tag{3.2}$$

The first two modes that propagate in this waveguide are the TM_1 and TE_1 [86] modes, thus, the fundamental mode is the result of the combination of a TM and a TE, the hybrid HE_{11} [90, 86]. The Fourier transform of the

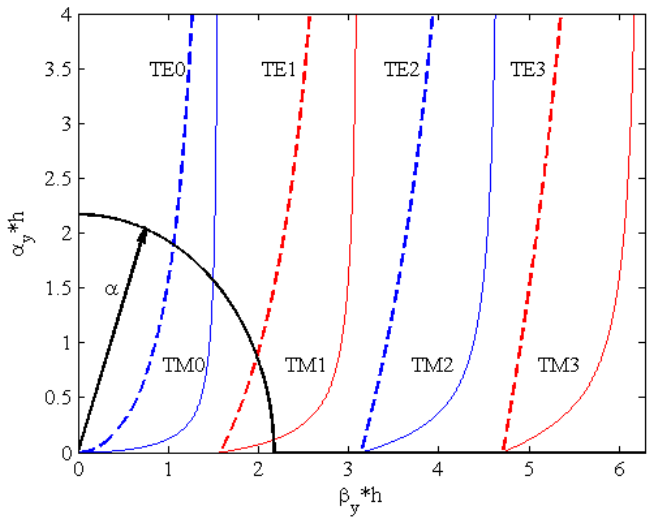

Figure 3.2: First four propagating modes for a dielectric waveguide of $\epsilon_r = 12.9$, and $a = 180\ \mu m$ at $200\ GHz$. TE (dashed) modes odd and even and TM (solid) modes odd and even.

fields for this mode in the dielectric waveguide aperture produces broadside radiation. We neglect the two first modes (TM_0 and TE_0) because they do not correspond to any guided mode [93].

For all the modes shown in Fig. 3.2, both TE and TM (of the same order) have the same cut-off frequency. Thus all the modes propagating in the structure are a combination of TE and TM, resulting in hybrid modes.

In some references [90, 94], through mode matching techniques and after some approximations to the problem of solving the modes that propagate in rectangular and circular dielectric waveguides, it is concluded that these structures allow hybrid modes propagation, with the fundamental mode being HE_{11}. This agrees with other works on this field [86, 89] about substrate waveguides and horns partially filled with dielectrics.

Due to the high dielectric constant, the single mode operation bandwidth is reduced in comparison with previous results [89, 91], and more power is coupled into higher order modes. This prevents the radiation from being highly directive [89] especially when the flare angle is large. Fig. 3.2 is used in this case for the design of the waveguides for Section 3.2, for not allowing the propagation of higher order modes.

Previous works on dielectric waveguides or loaded-dielectric waveguides have presented good results by reducing the cross polarization levels of un-

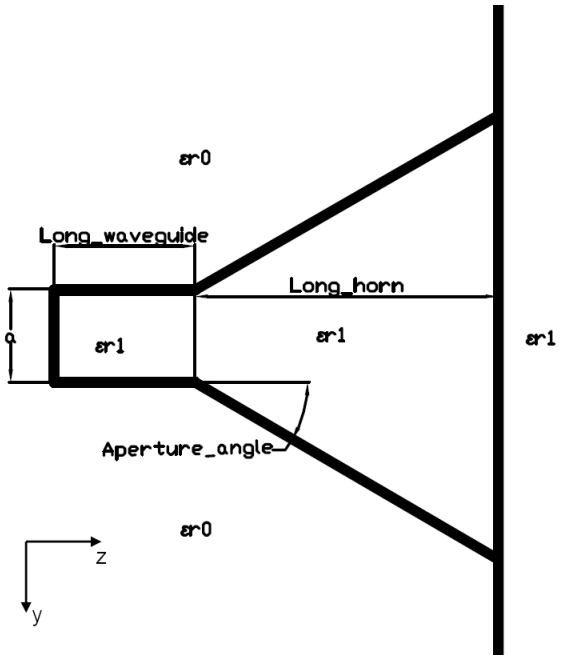

Figure 3.3: Sketch of the system: horn ended with an infinite substrate layer.

loaded horns thanks to the excitation of HE_{mn} higher order components [89]. In spite of the cross polarization reduction, the presence of these higher order modes also limits the bandwidth when the power coupled to them is too high [89].

Here, the dielectric waveguide is used to propagate the HE_{11} mode to improve the energy coupled from the mode to the dielectric horn. If we discard the slab, this coupling is less efficient in terms of the energy coupled to the fundamental mode.

3.1.2 Dielectric horn

The rectangular dielectric waveguide is open to form a dielectric horn as depicted in Fig. 3.3. In this figure, the antenna is printed on the left side of the dielectric slab, while in the right-hand side the substrate is infinite towards the Z direction.

In order to study the propagation in the dielectric horn, one can make the same assumption that in conventional horns. When the HE_{11} mode is propagating, the phase term for the spherical wave front in the mouth of the horn is added. Finally, the radiated fields are obtained as there is no change in the medium because an infinite dielectric is assumed [90].

According to previous studies [89, 90, 91], the HE_{11} mode can propagate in dielectric filled horns if an air-gap between the substrate and the metal walls were present [91]. In this paper we assume an infinite gap so the equations are still valid in the limit. Therefore, the HE_{11} mode or a combination of HE_{mn} modes can be excited in the horn. These modes will produce broadside radiation.

Regarding the broadband behavior of the dielectric horn, the operation frequencies are from the cut-off frequency of the dielectric slab that feeds the horn up to the limit when higher order modes are propagating in the structure with comparable power. Within higher frequencies, more energy is coupled to these higher order modes and not only to the fundamental HE_{11} mode, and the radiation is no longer broadside [89]. This is also strongly limited by the dielectric permittivity [89] where the energy into higher order modes is strongly coupled producing a reduction in the operating bandwidth in the upper limit.

3.2 Waveguide and horn excitation by a printed antenna

For the excitation of the dielectric waveguide, a planar printed antenna is employed, so the modes excited on each case can be identified by the set of modes that can propagate in the specific waveguide. The antennas employed in this paper are dipole and log-spiral antennas. The proposed feeding antennas are patterned in one of the ends of a dielectric slab that feeds the substrate horn as shown in Fig. 3.3. The dimension of the dielectric waveguide that feeds the horn is $a = 180\ \mu m$ and is the same in both cases, and is chosen according Fig. 3.2. This size only allows the propagation of the first two modes that compose the fundamental HE_{11} component. All the waveguides and horns considered in this paper have the same flare angle in both E and H plane.

For the generation of THz radiation a planar structure is employed. For the proposed system, a n-i-pn-i-p superlattice photomixer [76] on an InP substrate ($\epsilon_r = 12.9$) is used. The photomixer generates the current in the THz band that results from the beat of two monochromatic laser signals, as in the previous Chapter.

All the simulations are performed with CST 2010 [81] assuming an infinite dielectric along the Z axis in the mouth of the horn. This assumption is made to neglect the reflections from the air-InGaAs interface that would cause

bad quality radiation patterns. In Section IV, for practical implementation a high resistivity Silicon lens will be added to the system agreeing with this assumption. The polarization of the output field agrees with the one of the original antenna.

3.2.1 Dipole excitation

For the first case, a dipole excitation is studied. As it is linearly polarized, fewer modes than with the spiral feeding will be excited in the waveguide. The field excited by a dipole inside a dielectric horn is the fundamental HE_{11} mode. The half-wavelength dipole for the simulations is designed for a resonating frequency of 900 GHz, printed in the air-InGaAs interface of the dielectric.

The input impedance of the antenna does not change, compared with the case of the antenna over InGaAs without the horn, as the dipole can be considered as printed in the same air-InGaAs interface as for previous studies [76]. The main difference in the performance of the antenna lies in the radiation pattern characteristics: the 3dB beamwidth and the gain. Table 3.1 shows the result for the antenna gain in simulation, printed over a flat substrate and over the etched dielectric horn, using an infinite dielectric width. It can be seen that an increase in the gain of the antenna of 15 dB at 700 GHz results when a substrate pyramidal horn with an aperture of 737.2 μm in both E and H planes, a length of 900 μm of InGaAs ($\epsilon_r = 12.9$) and a flare angle of 28° This change in the radiation pattern is due to the focusing of the energy through the broadside direction reducing the diffusion of the energy into the substrate.

Fig. 3.4 shows the behavior for the gain of the antenna in terms of the aperture angle and the length when the excitation is the half-wavelength dipole. It has a maximum for each aperture angle, and an absolute maximum, as in the conventional metallic horns [86]. The maximum gain achieved is 22.5 dB with a single dipole feeding the dielectric slab. As long as the aperture angle is small enough (less than 35°), there is a strong increase in the gain of the system, especially when the length of the horn is more than 1.5 λ_{air}. Nevertheless, when the increase in gain is minimum, compared to a conventional system, this structure produces an increase of at least 4 dB in gain.

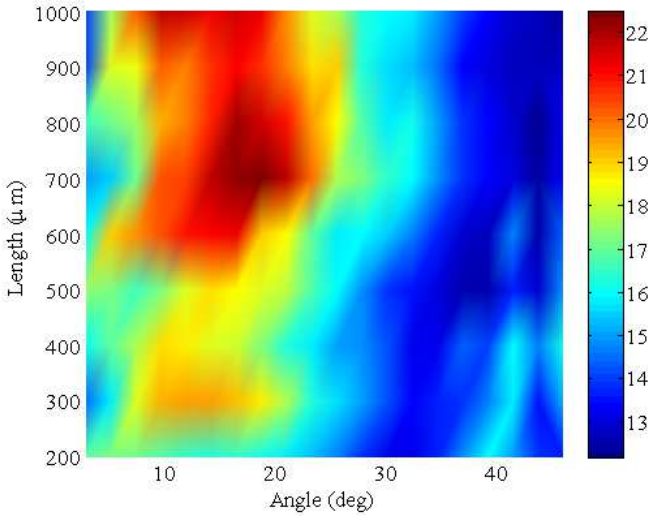

Figure 3.4: Gain in terms of aperture angle and length of the horn at 900 GHz.

3.2.2 Spiral excitation

In order to take advantage of the broadband characteristics of the dielectric horn and the photomixer used for THz generation, a spiral antenna printed on one side of a dielectric waveguide is used to feed the dielectric horn. This spiral is designed to work from 150 GHz to 3 THz [82], with a diameter of 150 μm. The size of the antenna should be the smallest possible in order to reduce the dielectric waveguide input aperture size, a. In this way the highest working frequency will be achieved. The size of the waveguide has also been chosen according to Fig. 3.2, allowing the propagation only of the first two modes (TE_1 and TM_1). The cut-off frequency of the waveguide is always below the dimensions of the antenna. Then, according to Eq. 3.3 and taking into account that the antenna is always larger in diameter than one half of the minimum wavelength in the dielectric, being m the mode order, and ϵ_d, μ_d, ϵ_0, and μ_0 the dielectric and vacuum permittivities and permeabilities respectively, and a the aperture size of the waveguide, the lower cut-off frequency will be given by the size of the antenna.

$$(f_c)_m = \frac{m}{2a\sqrt{\epsilon_d\mu_d - \epsilon_0\mu_0}} \tag{3.3}$$

It should be noted that the limiting factor for the upper frequency is the dielectric horn substrate due to the higher order modes propagating in the

Table 3.1: Gain comparison with dipole excitation

Frequency (THz)	Gain isolated (dB)	Gain with horn (dB)
0.5	6.96	19.43
0.6	7.07	21.38
0.7	7.62	21.36
0.8	8.30	20.23
0.9	8.12	19.04
1	8.95	18.21

Table 3.2: Gain comparison with spiral excitation

Frequency (THz)	Gain isolated (dB)	Gain with horn (dB)
0.5	8.27	15.54
0.6	8.41	19.85
0.7	8.46	18.89
0.8	8.72	22.18
0.9	9.11	22.29
1	8.56	23.08
1.1	9.21	20.60
1.2	10.09	18.60
1.3	9.25	20.60
1.4	9.58	21.70
1.5	10.59	21.40
1.6	10.60	24.90

substrate. This is due to the combined effect of a high dielectric constant with a wide aperture shape [89]. In addition, the coupled energy to these higher order modes is large. For the case of the spiral, the modes excited in the structure are two HE_{11} modes, shifted 90°. Then, the pyramidal horn substrate will also radiate circular polarization as the isolated spiral. The axial ratio for broadside direction is 0.6 dB at 1 THz in simulation.

Table 3.2 shows a comparison between the gains for the spiral system at different frequencies similar to the one shown for the dipole case. The length of the horn substrate has been set to 450 μm while the aperture angle to

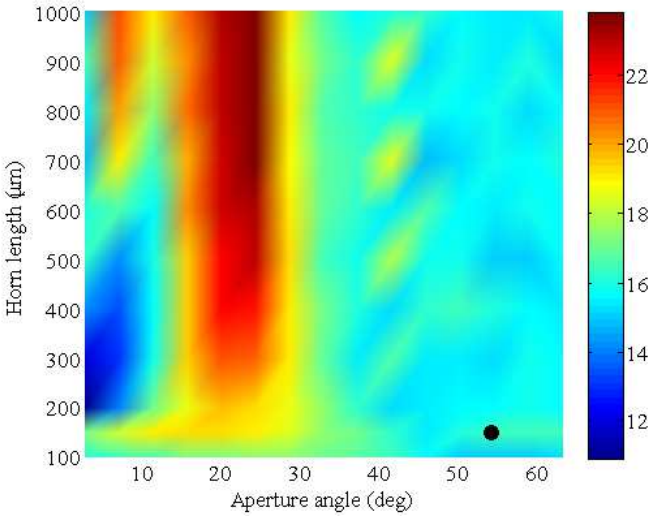

Figure 3.5: Gain for the spiral fed antenna in terms of aperture angle and length of the horn at 1 THz. The black dot represents the manufactured antenna for Section 3.3.

25°. There is an increase of 14.5 dB at 1 THz and more than 7 dB in the whole operation bandwidth. In this way, the broadband characteristics of photomixers, log-spirals and substrate horns are combined to build an ultra-wideband system. All these results are obtained with the simulation of the antenna over a semi-infinite substrate.

The gain of the system for different aperture angles and horn lengths at 1 THz is shown in Fig. 3.5. The maximum gain is achieved when the flare angle is 28°. It can also be appreciated that is almost independent with the length of the horn. The best values to achieve the maximum gain at 1 THz are: aperture angle of 28° and length of 850 μm. With these values, the working frequency band is centered at 1 THz and the horn is working from 0.2 THz to 2 THz.

3.3 Experimental results

The proposed structure has been manufactured to provide validation to the theoretical analysis following the same procedures as for Chapter 2. The excitation element employed used for THz generation is a spiral, printed over a 450 $\mu m \times 450$ μm dielectric slab which opens with a 54° angle and has a depth of 240 μm. The aperture of the horn on the other side is approximately

Table 3.3: Simulated gain comparison with spiral excitation for the manufactured antenna

Frequency (THz)	Gain isolated (dB)	Gain with horn (dB)
0.2	6.17	10.38
0.3	7.28	12.03
0.4	8.05	11.83
0.5	8.27	10.71
0.6	8.41	9.80
0.7	8.46	11.03
0.8	8.72	10.66
0.9	9.11	10.58
1	8.56	10.62
1.1	9.21	10.20
1.2	10.9	10.34
1.3	9.25	11.54
1.4	9.58	11.77

806 $\mu m \times 806$ μm (a SEM picture of the device is shown in Fig. 3.6(a)). The semiconductor dielectric substrate is InGaAs with an $\epsilon_r = 12.9$. Due to the fabrication process and etching limitations [95] the resulting angle is 54° for a horn length of 150 μm, this point is indicated in Fig. 3.5 with a black dot.

The final dimensions of the horn are not optimal for the application at 1 THz. The dielectric slab is not etched, so the antenna was directly printed on the mouth of the horn, not being optimal regarding the coupling of energy to the HE_{11} mode as mentioned in Section 3.2.

The results were compared with a reference of the same antenna, printed on the same wafer but without the substrate etching.

The measurements were made with the set up shown in Fig. 3.3 (b), using a hyperhemispherical 5 mm radius Si lens with a slab of 1080 μm, two parabolic off-axis mirrors with $f/D = 1$ and a Golay cell placed in the focus of the second parabolic mirror. It has been measured the power spectrum of the device from 100 GHz up to 1.5 THz. The efficiency defined as $Power_{THz}/(A_{photomixer})^2$ is shown in Fig. 3.7 with the spectrum of the reference antenna.

According to the simulations performed for the dimensions of the phys-

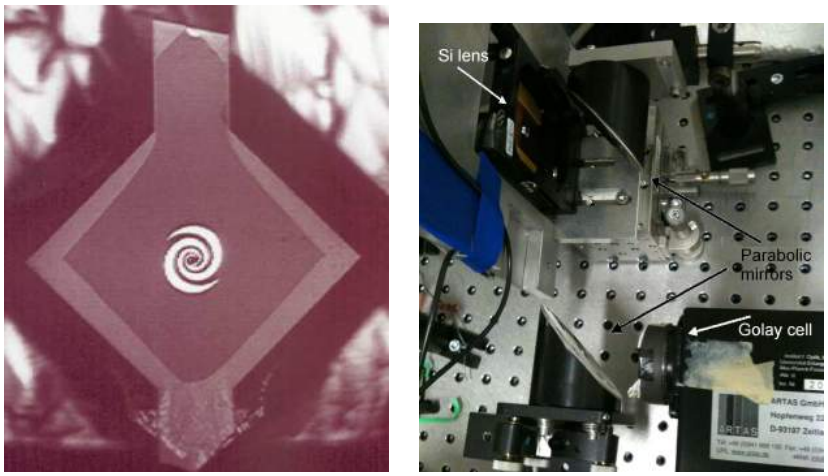

(a) (b)

Figure 3.6: (a) Measurement setup and (b) SEM image of the dielectric horn antenna processed with a depth of 150 μm and a 54 deg. flare angle.

ical horn after the etching, it provides 4 dB increase of gain at 200 GHz. The simulated gain comparison for the manufactured antenna is shown in Table 3.3 for different frequencies. Despite the horn is not optimal regarding the size, the gain of the sistem is still above the reference antenna in the whole band. This agrees with the results obtained from the measurements, where there is an increase in the efficiency in the 200 GHz - 400 GHz band, where the HE_{11} mode can propagate in the manufactured structure. The strong peak below 200 GHz is attributed to an artefact as the antenna used for these devices has a low frequency cut off at around 200 GHz (where the horn would work optimum).

For frequencies higher than 400 GHz, the horn is extremely big so the performance is not optimum, and higher order modes are propagating. In Fig. 3.8 we show the efficiency of the dielectric horn antenna normalized to the efficiency of the reference antenna in a logarithmic scale. This efficiency is higher than the reference antenna for nearly the whole band.

Regarding measurement tolerances, in Fig. 3.7 are also shown two different measurements for the antenna under test (AUT), this is the horn antenna. For all the cases, the system is setup in an alignment when the maximum power is received, disregarding alingment errors for all the measurments. The error obtained is below the difference for the horn-reference case, so the deviation is due to an improve on the efficiency for the horn antenna with respect to the reference.

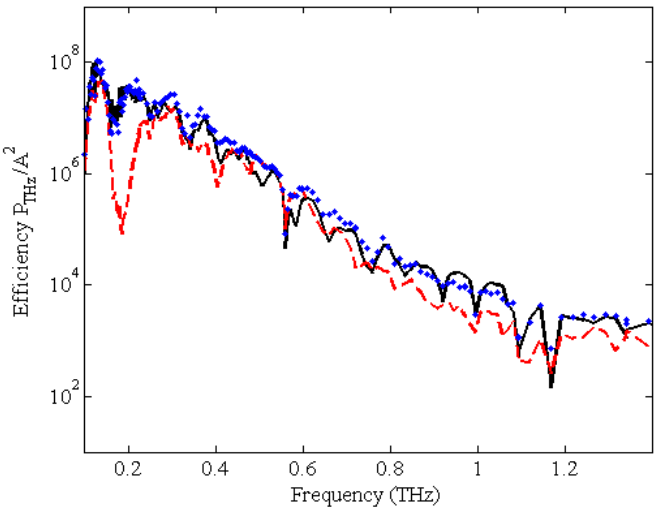

Figure 3.7: Power spectrum of two different measurements for the antena+horn (solid and dots) for showing measuring tolerances. Reference antenna (dashed) in logarithmic scale.

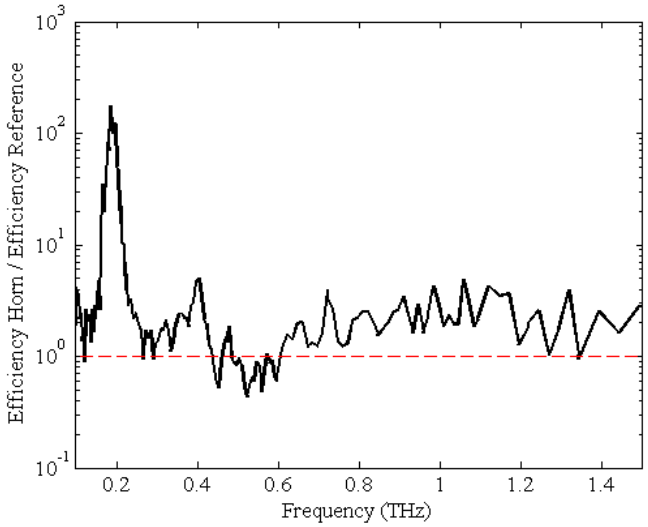

Figure 3.8: Power spectrum of the antenna+horn normalized to the reference antenna in logarithmic scale.

3.4 Conclusions, future lines and contributions

A new substrate horn antenna in the THz band has been developed. A horn substrate with a planar printed antenna over a dielectric slab propagating the HE_{11} mode has been used. The energy coupling to this mode is maximized through the dielectric slab. A 1 : 10 bandwidth has been achieved with a broadband log-spiral antenna. The measurements agree with calculations despite the frequency shift associated with manufacturing issues. At this moment new devices are being processed with a central frequency of 1 THz with a different mask set.

To continue with power enhancement, the devices developed on this Chapter are the basis for an array of horns. There are two possible directions: the first one is the optimization of the horn manufacturing, by obtaining different slopes on the substrate and including a section of waveguide at the begining of the structure, so the modes propagating in the struture are not diverged.

Another possible line will be the implementation of the element in an array of horns. As the devices will have a separation of more than one wavelength, the mutual coupling between them will be almost negligible, allowing the implementation of imaging arrays with symetric beam patterns and therefore scanning properties. Also, in combination of both lines, if the size of the horn could be reduced, the distance between the elements will be smaller, allowing the implementation of phased arrays.

The contributions of the content of this Chapter to international journals, conference papers and research stages are:

- B. Andrés-García, L. E. García-Muñoz, S. Bauersmidth, S. Preu, S. Malzer, G. Dohler, L. J. Wang and D. Segovia-Vargas, "Gain Enhancement by Dielectric Horns in the Terahertz band", *IEEE Transactions on Antennas and Propagation*, vol. 59, no. 9, September 2011.
- Belén Andrés García, Luis Enrique García Muñoz, Sebastian Bauerschmidt, Sascha Preu, Stefan Malzer, Gottfried Dohler, Linjun Wang and Daniel Segovia Vargas, "Dielectric Horn Antennas in the Terahertz Band", *URSI 2011*, Madrid, Spain, 2011.
- B. Andrés-García, L.E. García-Muñoz, S. Bauersmidth, S. Preu, S. Malzer, G. Dohler, L. J. Wang, D. Segovia-Vargas, "Dielectric Horn Antennas in the Terahertz Band", *EuCAP (European Conference on Antennas and Propagation)*, Rome, Italy, 2011.
- A. Rivera-Lavado, L. E. García-Muñoz, S. Bauersmidth, S. Preu, S. Malzer, G. Dohler, B. Andrés-García and D. Segovia-Vargas, "Arrays

and New Antenna Topologies for Increasing THz Power Generation Using Photomixers", *Journal of Infrarred, Millimeter and Terahertz Waves*, vol. 34, no. 2, January 2013.

- Research stage during 5 months in Max Planck Institute for the Science of Light,in collaboration with FAU, May-September 2010.

CHAPTER 4

New Designs for Tapered Slot Antennas

4.1 Introduction

A huge issue in the generation of THz radiation to free space, as explained in the introduction of this thesis, is to achieve a high, or at least, acceptable efficiency with a reduced cost and easyness in integration with planar feeds. One of the most common approach is the use of a Si lens, that symmetrizes the beam and fullfils the function of medium impedance matching, as employed in the first block of this Thesis.

The goal on the current Chapter is to develop antennas that allow getting rid of the Si lens and also achieving a high gain, symmetric radiation patterns and are printed over a planar substrate in order to reduce the cost and to facilitate the integrability with devices such as photomixers or diodes. One of the best candidates to meet all of these requierements are tapered slot antennas, first appeard in [97, 98, 111].

Tapered Slot Antennas (TSA's) have been widely used as ultra-wide band radiating elements since they were introduced [111]. Their use as the individual elements in ultra-wide band arrays has been underpinned by their ease of fabrication in either microstrip or coplanar strip technology. The Square Kilometer Array (SKA) project is one of the most recent examples where TSAs have been employed in a dense array for Radioastronomy in low frequency bands (200 MHz - 1 GHz [99, 100]). TSAs are also versatile candidates for application as antennas in the low THz (0.3 THz - 3 THz). Their use can

reduce the effect of the increasing transmission losses and low efficiency in planar antenna systems due to the use of dielectric lenses [101, 68]. Studies of TSAs printed on an ϵ_r substrate have been reported in [102, 103, 104], in which application of the Method of Moments (MoM) yielded a comprehensive prediction of the TSAs properties. Semianalytic numerical methods such as FDTD (Finite-Difference Time-Domain method) or FEM (Finite Element Method) have been developed to study the TSAs in a dense array configuration [87, 105, 106].

One of the main limitations of these antennas is the thin substrate where they should be manufactured, when there are needed in the THz regime. As a goal for this chapter, is to study the possibility of new topologies to allow the construction of TSAs in the THz range. In [97, 98] guidelines based on experimental results for the design of LTSAs (TSA antennas with a linear shape aperture) employing coplanar-strip technology with a substrate of permittivity ϵ_r are given, and the so-called Yngvesson limit is introduced which provides an experimental maximum thickness for the dielectric, for which the LTSA operates efficiently. If the effective thickness of the substrate is given as $t_{eff} = t(\sqrt{\epsilon_r} - 1)$ where t is the actual substrate height, then the range for acceptable operation in terms of beam symmetry of a TSA has been experimentally found to be $0.005 \leq t_{eff}/\lambda_0 \leq 0.03$. For a substrate thickness above or below these bounds the performance of the LTSA is degraded in terms of efficient end-fire radiation [97, 98]. This limit is especially critical at very high frequencies, as mentioned before, especially in the terahertz regime [101], where the antenna dimensions are sometimes electrically larger than the Yngvesson limit because of manufacturing considerations [97]. In [101, 107] the authors discuss LTSAs suspended on membranes, printed over EBGs, as well as novel configurations allowing thicker substrates. Even though in both of these studies as well as in [97, 108] it was implied that a theoretical effort is underway to explore the radiation mechanism of this class of antennas in detail, nevertheless no progress has been reported to date in the literature related to this topic. This situation is the main motivation behind the analysis here, whose objective is provide a theoretical understanding of radiation mechanism of the antennas, essential for their employment in the THz band.

Previous approaches have also been developed for the analysis of the TSA antennas in terms of propagating electromagnetic modes. The work in [102] is noteworthy in that a field formulation in the antenna slot was employed. The analysis is based on dividing the complete LTSA into multiple flared slots and using a transmission line approach. In that analysis it was concluded that the radiation of a dielectric free LTSA is due to a TEM mode with all its field components aligned with the slot plane. In [109, 110], a modal analysis

based on conical transmission lines was undertaken which concluded that the radiation properties of the LTSA depend only on the TEM and other TE modes contained in the slot plane. However, when the same study is applied to a LTSA on a dielectric substrate, the authors divide the antenna up into a series of radiating slots and in the analysis apply a variational formulation [110] to calculate the field in the aperture. The study however did not include higher order modes in the analysis.

In the first section of the current chapter, LTSAs are analyzed, as equivalent to TSAs without loss of generality. A vivaldi antenna is no more than including an exponential profile instead of a linear aperture in the antenna [111]. The theoretical approach proposed for understanding the radiation mechanism in this thesis is based on the assumption that the LTSA is equivalent to a sectoral horn antenna (or equivalently a flared waveguide) filled with dielectric, with two Perfect Magnetic Conductor (PMC) walls and two dielectric-air interfaces (a direct transition between the ϵ_r substrate and the ϵ_0 open substrate) as shown in Fig. 4.2.

Also, in this chapter we include some applications of the method to real cases. With this method, the electromagnetic behaviour of the antennas is fully explained with a theoretical understanding of the radiation mechanism.

Linking the TSA design with the issue of THz signal generation, as feeds for the radiating devices, photomixers are used, as there are needed sources for the practical manufacturing and demonstration of the developed theories. Photomixing is a well established technique for signal generation in the millimeter and submillimeter bands [8]. The huge bandwidth offered by a single photomixer (from DC to several Terahertz) could potentially revolutionize several applications which require large bandwidth and high resolution. The progress made in the material optimization has lead to carrier trapping times below 1 *ps* [112] at moderate bias voltages, which is essential for fabrication of photomixers in the Terahertz range.

Usually, photomixers are used to excite a large variety of antennas, both resonant and broadband structures like dipoles, bowties and log-periodic spirals. Due to the insufficient directivity of these antennas, it is often necessary to collimate the beam, using a so-called lens substrate, which usually has an extended-hemispherical form. Another reason for the use of this type of substrate is that no power is lost in surface modes [113]. The substrate with the photomixer device is sometimes glued to the substrate lens whose dielectric constant is chosen to be similar to that of the photomixer substrate (which is usually a III-V compound semiconductor[114], [115]). This fact avoids reflection in the interface between both media. Nevertheless, since the Terahertz beam is collimated in the lens-substrate to free-space interface, power is lost

due to the reflection in the interface. Due to the relatively high dielectric constant of the lens-substrate ($\epsilon_r \approx 13$) the reflection losses in this interface are roughly 30%.

Since broadband antireflection coatings in the THz band are difficult to process, specially on curved substrates, it is not easy to avoid the power lost due to reflection losses on the lens-substrate to free-space interface. This fact, together with the complex adjustment of the lens substrate relative to the radiating antenna (coma and spherical aberrations might occur if not properly adjusted) is one of the motivations of this approach.

It is proposed the design of an antenna removing the substrate lens and preserving all the properties of high directivity, low beamwidth, broadband, high impedance and high gaussicity, with the use of a TSA.

First of all, a theoretical analysis is developed with the aim of explaining the propagation characteristics of these atennas. Further on, several applications are presented, demonstrating the theory in the first part of this Chapter. All of them fully agree with the method giving some explanation to previous theories too.

4.2 Theoretical analysis of a TSA

On the scope of this thesis, a theoretical analysis for antennas of TSA type has been developed. The fundamentals lay on finding the mode responsible for the radiation and can propagate through the structure. It is assumed a simplified model that contains and provides an explanation to all the experimental limits obtained in previous works only by means of trial and error [97, 98]. The model that the theory is based on assumes a dielectric slab, where two of the boundaries are modelized as PMC while the other two opposite boundaries have an open condition (air). The structure is presented in Fig. 4.1.

With this model, two hard and two soft conditions are considered in the structure analysis, therefore, the differential equation system can be solved based on waveguide theory [86]. This equations will be described in Section 4.2.1 The hypothesis of placing the two PMC walls on the boundaries of the dielectric slab agrees both in radiation properties and in field components with those existing in a TSA, as will be demonstrated on further sections. Several LTSA type antennas have been analyzed, employing different numerical methods to avoid a method-conditioned result, such as CST Microwave Studio [81], Fecko [116] and HFSS [117]. All of them show equal results regarding the X, Y and Z components of the electric and magnetic fields. These simulations are detailed in Section 4.2.2.

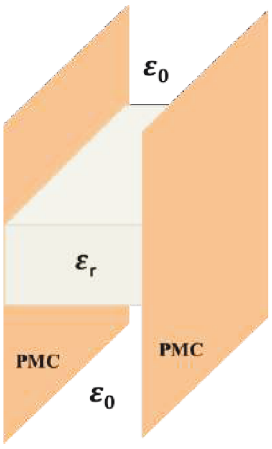

Figure 4.1: Dielectric slab with the model boundary conditions

The structure on Fig. 4.1 is modeled as in waveguide theory, and validated in next sections by means of simulations and applications with new topologies. The results thrown by this theoretical model are then compared to the electric and magnetic fields on the LTSA, agreeing with the hypothesis on this section. A linear TSA will be employed from now on for the sake of conciseness and clarification.

4.2.1 Equivalent modal analysis of the dielectric waveguide

This Section presents an analytic study of the modes propagating through a dielectric waveguide with two walls in the form of PMC boundaries (see Fig. 4.1) and two walls with open boundary conditions (dielectric-air interface). These modes will be identified with the modes that propagate through the LTSA presented in the previous section. The process will identify a mode chart of the equivalent structure with the radiating modes on a TSA. As an hypothesis it is assumed that the structure is able to support an hybrid mode distribution. These hybrid modes are characterized by using both odd and even modes [86]. Hereafter, this notation will be followed, and will not be repeated for conciseness. All the examples are calculated at 30 GHz with a slot width (W) of λ_0 and different heights as a first approach. The coordinates origin is placed on the center of the slot for the Y axis and on the left corner for the X axis.

Even modes

For even modes, the phase constant along the X axis is defined as $k_x = l\pi/W$. Then, the longitudinal field components in the core and in the cladding of the structure are given by (4.1) and (4.2) respectively, where k_y is the propagation constant along Y axis, and A_{TM}, A_{TE}, B_{TM} and B_{TE} are the constants obtained from the boundary conditions.

$$\left.\begin{array}{c} E_{z,n} = A_{TM} cos(k_x x) sin(k_y y) \\ H_{z,n} = A_{TE} sin(k_x x) cos(k_y y) \end{array}\right\} \tag{4.1}$$

$$\left.\begin{array}{c} E_{z,m} = B_{TM} cos(k_x x) exp(-\alpha_y y) \\ H_{z,m} = B_{TE} sin(k_x x) exp(-\alpha_y y) \end{array}\right\} \tag{4.2}$$

Thus, the complete set of fields in the core is given by (4.3) and (4.4) for E and H fields.

$$\begin{aligned} \vec{E_n} = A_{TM} & \begin{bmatrix} \frac{j\beta_z k_x}{\chi_n^2} sin(k_x x) sin(k_y y) \\ -\frac{j\beta_z k_y}{\chi_n^2} cos(k_x x) cos(k_y y) \\ cos(k_x x) sin(k_y y) \end{bmatrix} + \\ + A_{TE} & \begin{bmatrix} \frac{j\omega\mu k_y}{\chi_n^2} sin(k_x x) sin(k_y y) \\ \frac{j\omega\mu k_x}{\chi_n^2} cos(k_x x) cos(k_y y) \\ 0 \end{bmatrix} \end{aligned} \tag{4.3}$$

$$\begin{aligned} \vec{H_n} = A_{TM} & \begin{bmatrix} \frac{j\omega\epsilon_n k_y}{\chi_n^2} cos(k_x x) cos(k_y y) \\ \frac{j\omega\epsilon_n k_x}{\chi_n^2} sin(k_x x) sin(k_y y) \\ 0 \end{bmatrix} + \\ + A_{TE} & \begin{bmatrix} -\frac{j\beta_z k_x}{\chi_n^2} cos(k_x x) cos(k_y y) \\ \frac{j\beta_z k_y}{\chi_n^2} sin(k_x x) sin(k_y y) \\ sin(k_x x) cos(k_y y) \end{bmatrix} \end{aligned} \tag{4.4}$$

Also the complete set of fields in the cladding is given by (4.5) and (4.6) for E and H fields.

$$\begin{bmatrix} sin(k_yh) & -exp(-\alpha_yh) & 0 & 0 \\ \frac{j\omega\epsilon_nk_y}{\chi_n^2}cos(k_yh) & \frac{j\omega\epsilon_m\alpha_y}{\chi_m^2}exp(-\alpha_yh) & -\frac{j\beta_zk_x}{\chi_n^2}cos(k_yh) & \frac{j\beta_zk_x}{\chi_m^2}exp(-\alpha_yh) \\ \frac{j\beta_zk_x}{\chi_n^2}sin(k_yh) & -\frac{j\beta_zk_x}{\chi_m^2}exp(-\alpha_yh) & \frac{j\omega\mu k_y}{\chi_n^2}sin(k_yh) & \frac{j\omega\mu\alpha_y}{\chi_m^2}exp(-\alpha_yh) \\ 0 & 0 & cos(k_yh) & -exp(-\alpha_yh) \end{bmatrix} \begin{bmatrix} A_{TM} \\ B_{TM} \\ A_{TE} \\ B_{TE} \end{bmatrix} = 0 \tag{4.7}$$

$$\begin{aligned} \vec{E_m} = B_{TM} & \begin{bmatrix} \frac{j\beta_zk_x}{\chi_m^2}sin(k_xx)exp(-\alpha_yy) \\ \frac{j\beta_z\alpha_y}{\chi_m^2}cos(k_xx)exp(-\alpha_yy) \\ cos(k_xx)exp(-\alpha_yy) \end{bmatrix} \\ + B_{TE} & \begin{bmatrix} \frac{j\omega\mu\alpha_y}{\chi_m^2}sin(k_xx)exp(-\alpha_yy) \\ \frac{j\omega\mu k_x}{\chi_n^2}cos(k_xx)exp(-\alpha_yy) \\ 0 \end{bmatrix} \end{aligned} \tag{4.5}$$

$$\begin{aligned} \vec{H_m} = B_{TM} & \begin{bmatrix} -\frac{j\omega\epsilon_m\alpha_y}{\chi_m^2}cos(k_xx)exp(-\alpha_yy) \\ \frac{j\omega\epsilon_mk_x}{\chi_m^2}sin(k_xx)exp(-\alpha_yy) \\ 0 \end{bmatrix} + \\ + B_{TE} & \begin{bmatrix} -\frac{j\beta_zk_x}{\chi_m^2}cos(k_xx)exp(-\alpha_yy) \\ \frac{j\omega\beta_z\alpha_y}{\chi_m^2}sin(k_xx)exp(-\alpha_yy) \\ sin(k_xx)exp(-\alpha_yy) \end{bmatrix} \end{aligned} \tag{4.6}$$

$$\begin{aligned} \omega^2\mu[\frac{\alpha_y}{\chi_m^2}cos(k_yh) - \frac{k_y}{\chi_n^2}sin(k_yh)]\cdot \\ \cdot[\frac{\epsilon_nk_y}{\chi_n^2}cos(k_yh) + \frac{\epsilon_m\alpha_y}{\chi_m^2}sin(k_yh)] = \\ = (\beta_zk_x)^2(\frac{1}{\chi_n^2} - \frac{1}{\chi_m^2})^2\frac{sin(2k_yh)}{2} \end{aligned} \tag{4.8}$$

$$\begin{cases} k_x^2+k_y^2+\beta_z^2=\omega^2\mu\epsilon_n \\ k_x^2-\alpha_y^2+\beta_z^2=\omega^2\mu\epsilon_m \end{cases} \rightarrow k_y^2 + \alpha_y^2 = \omega^2\mu(\epsilon_n - \epsilon_m) \tag{4.9}$$

$$\alpha_y = \sqrt[2]{\omega^2\mu(\epsilon_n - \epsilon_m) - k_y^2}; \chi_n^2 = k_x^2 + k_y^2 \tag{4.10}$$

$$\beta_z = \sqrt[2]{\omega^2\mu\epsilon_n - k_x^2 - k_y^2} \tag{4.11}$$

$$\chi_m^2 = k_x^2 - \alpha_y^2 = k_x^2 + k_y^2 - \omega^2\mu(\epsilon_n - \epsilon_m) \tag{4.12}$$

When the boundary conditions are applied to the E_z, H_x, E_x and H_z components, the matrix equation in Eq. 4.7 is obtained. As it is clear from this equation, that the determinant of the matrix must be 0 for extracting the non trivial equation. This is a well known phenomenon in guided waves with dielectric boundaries. This couples together the coefficients A_{TE} and A_{TM}. From this matrix, the characteristic equation is given by Eq. 4.8, and can be solved as shown in Eq. 4.9, where α_y, β_z and χ_m^2 are given by Eqs. 4.10, 4.11 and 4.12.

The coefficients for the TE and TM components are obtained once the characteristic equation has been solved. Then, the rank of the matrix for the continuity condition drops to 3 and it can be assumed $A_{TM} = 1$.

Odd modes

Once the even mode solution has been obtained, the odd equations are solved in a similar way. Then for the odd mode distribution the phase constant is set to $k_x = \frac{l\pi}{W}$ with $l \neq 0$. The longitudinal field components of the structure are given by Eq. 4.13 in the core and as Eq. 4.14 in the cladding.

$$\left.\begin{aligned} E_{z,n} &= A_{TM} cos(k_x x) cos(k_y y) \\ H_{z,n} &= A_{TE} sin(k_x x) sin(k_y y) \end{aligned}\right\} \tag{4.13}$$

$$\left.\begin{aligned} E_{z,m} &= B_{TM} cos(k_x x) exp(-\alpha_y y) \\ H_{z,m} &= B_{TE} sin(k_x x) exp(-\alpha_y y) \end{aligned}\right\} \tag{4.14}$$

Thus, the complete set of fields in the core is given by Eq. 4.15 for the E-field and as Eq. 4.16 for the H-field.

$$\begin{aligned} \vec{E_n} = A_{TM} & \begin{bmatrix} \frac{j\beta_z k_x}{\chi_n^2} sin(k_x x) cos(k_y y) \\ \frac{j\beta_z k_y}{\chi_n^2} cos(k_x x) sin(k_y y) \\ cos(k_x x) cos(k_y y) \end{bmatrix} + \\ + A_{TE} & \begin{bmatrix} -\frac{j\omega\mu k_y}{\chi_n^2} sin(k_x x) cos(k_y y) \\ \frac{j\omega\mu k_x}{\chi_n^2} cos(k_x x) sin(k_y y) \\ 0 \end{bmatrix} \end{aligned} \tag{4.15}$$

$$\begin{bmatrix} cos(k_y h) & -exp(-\alpha_y h) & 0 & 0 \\ -\frac{j\omega\epsilon_n k_y}{\chi_n^2} sin(k_y h) & \frac{j\omega\epsilon_m \alpha_y}{\chi_m^2} exp(-\alpha_y h) & -\frac{j\beta_z k_x}{\chi_n^2} sin(k_y h) & \frac{j\beta_z k_x}{\chi_m^2} exp(-\alpha_y h) \\ \frac{j\beta_z k_x}{\chi_n^2} cos(k_y h) & -\frac{j\beta_z k_x}{\chi_m^2} exp(-\alpha_y h) & \frac{j\omega\mu k_y}{\chi_n^2} cos(k_y h) & \frac{j\omega\mu\alpha_y}{\chi_m^2} exp(-\alpha_y h) \\ 0 & 0 & sin(k_y h) & -exp(-\alpha_y h) \end{bmatrix} \begin{bmatrix} A_{TM} \\ B_{TM} \\ A_{TE} \\ B_{TE} \end{bmatrix} = 0 \tag{4.19}$$

$$\begin{aligned} \vec{H_n} = A_{TM} & \begin{bmatrix} -\frac{j\omega\epsilon_n k_y}{\chi_n^2} cos(k_x x) sin(k_y y) \\ \frac{j\omega\epsilon_n k_x}{\chi_n^2} sin(k_x x) cos(k_y y) \\ 0 \end{bmatrix} + \\ + A_{TE} & \begin{bmatrix} -\frac{j\beta_z k_x}{\chi_n^2} cos(k_x x) sin(k_y y) \\ -\frac{j\omega\mu k_y}{\chi_n^2} sin(k_x x) cos(k_y y) \\ sin(k_x x) sin(k_y y) \end{bmatrix} \end{aligned} \tag{4.16}$$

Also the complete set of fields in the cladding is given by Eq. 4.17 for the E-field and by Eq. 4.18 for the H-field.

$$\begin{aligned} \vec{E_m} = B_{TM} & \begin{bmatrix} \frac{j\beta_z k_x}{\chi_m^2} sin(k_x x) exp(-\alpha_y y) \\ \frac{j\beta_z \alpha_y}{\chi_m^2} cos(k_x x) exp(-\alpha_y y) \\ cos(k_x x) exp(-\alpha_y y) \end{bmatrix} + \\ + B_{TE} & \begin{bmatrix} -\frac{j\omega\mu\alpha_y}{\chi_m^2} sin(k_x x) exp(-\alpha_y y) \\ \frac{j\omega\mu k_x}{\chi_n^2} cos(k_x x) exp(-\alpha_y y) \\ 0 \end{bmatrix} \end{aligned} \tag{4.17}$$

$$\begin{aligned} \vec{H_m} = B_{TM} & \begin{bmatrix} -\frac{j\omega\epsilon_m \alpha_y}{\chi_m^2} cos(k_x x) exp(-\alpha_y y) \\ \frac{j\omega\epsilon_m k_x}{\chi_m^2} sin(k_x x) exp(-\alpha_y y) \\ 0 \end{bmatrix} + \\ + B_{TE} & \begin{bmatrix} -\frac{j\beta_z k_x}{\chi_m^2} cos(k_x x) exp(-\alpha_y y) \\ \frac{j\omega\beta_z \alpha_y}{\chi_m^2} sin(k_x x) exp(-\alpha_y y) \\ sin(k_x x) exp(-\alpha_y y) \end{bmatrix} \end{aligned} \tag{4.18}$$

$$\begin{aligned}\omega^2\mu[\frac{\epsilon_m\alpha_y}{\chi_m^2}cos(k_yh)-\frac{\epsilon_nk_y}{\chi_n^2}sin(k_yh)]\cdot\\ \cdot[\frac{\alpha_y}{\chi_m^2}sin(k_yh)+\frac{k_y}{\chi_n^2}cos(k_yh)]=\\ =(\beta_zk_x)^2(\frac{1}{\chi_n^2}-\frac{1}{\chi_m^2})^2\frac{sin(2k_yh)}{2}\end{aligned} \tag{4.20}$$

On rearranging the terms, the matrix in Eq. 4.19 contains all the boundary conditions to obtain the characteristic equation of 4.20.

These boundary conditions, as for the even modes, are applied to the E_z, H_x, E_x and H_z components, Eqs. 4.21, 4.22, 4.23, 4.24.

$$E_z : A_{TM}cos(k_yh) = B_{TM}exp(-\alpha_yh) \tag{4.21}$$

$$\begin{aligned}H_x : A_{TM}[-\tfrac{j\omega\epsilon_nk_y}{\chi_n^2}sin(k_yh)]+\\ +A_{TE}[-\tfrac{j\beta_zk_x}{\chi^2}sin(k_yh)]=\\ =B_{TM}[-\tfrac{j\omega\epsilon_n\alpha_y}{\chi_n^2}exp(-\alpha_yh)]+\\ +B_{TE}[-\tfrac{j\beta_zk_x}{\chi^2}exp(-\alpha_yh)]\end{aligned} \tag{4.22}$$

$$\begin{aligned}E_x : A_{TM}[-\tfrac{j\beta_zk_x}{\chi_n^2}cos(k_yh)]+\\ +A_{TE}[-\tfrac{j\omega\epsilon_nk_y}{\chi_n^2}cos(k_yh)]=\\ =B_{TM}[-\tfrac{j\beta_zk_x}{\chi^2}exp(-\alpha_yh)]\\ B_{TE}[-\tfrac{j\omega\mu\alpha_y}{\chi_n^2}cos(k_xx)exp(-\alpha_yh)]\end{aligned} \tag{4.23}$$

$$H_z : A_{TE}sin(k_yy) = B_{TE}exp(-\alpha_yh) \tag{4.24}$$

4.2.2 Full-wave simulation of the LTSA antenna and the proposed equivalent model

This section will present the simulation results with Ansoft HFSS [117] software (FEM approach) in order to study and understand the electromagnetic fields both in a LTSA and in the equivalent flared waveguide (sectoral horn) loaded with dielectric. The results obtained with CST Microwave studio [81] (FDTD approach) for the LTSA itself are the same as those obtained with HFSS, reducing the errors due to the numerical method selected, therefore only the first are displayed due to clarifying purposes and conciseness. Fig. 4.3

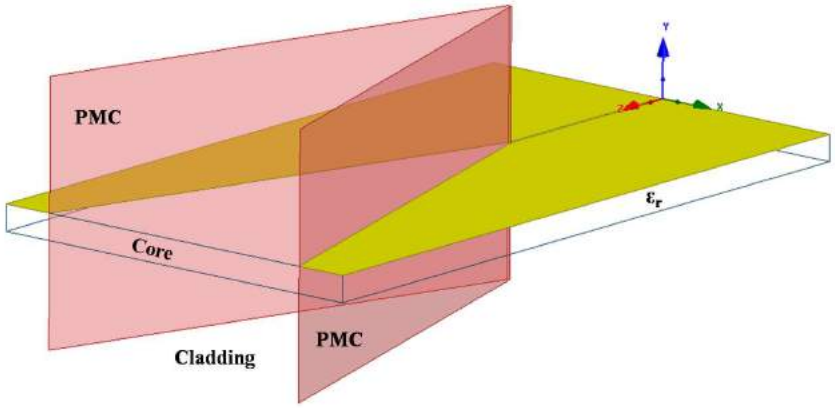

Figure 4.2: Equivalent model of the TSA with PMC walls.

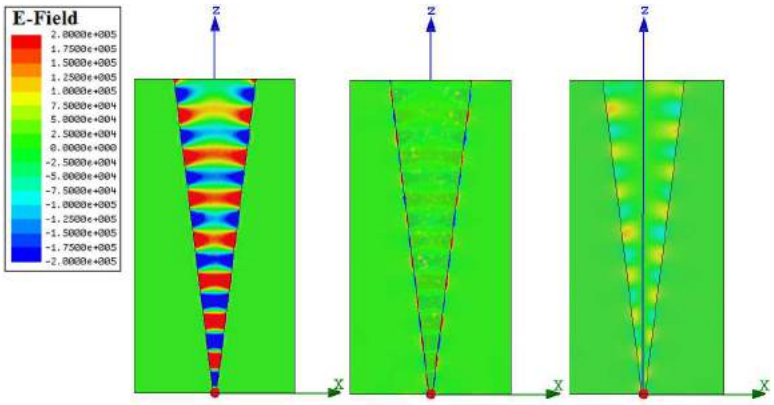

Figure 4.3: E-field components for a LTSA: Ex, Ey,Ez (HFSS).

shows the three X, Y and Z components of the E-field in the antenna while Fig. 4.4 shows the corresponding H-field components. The LTSA was excited through a lumped port for characterization of the real modes.

For comparison purposes with the E and H fields for the actual LTSA, an equivalent structure is simulated where the dielectric in the slot is bounded with two PMC walls, as plotted in Fig. 4.2 and whose field components are shown in Figs. 4.5 and 4.6 respectively.

From the figures, it can be concluded that there are no substantial differences between these two proposed configurations. All the three field components have the same distribution and relative intensity. This confirms the hypothesis that the electromagnetic field in the LTSA has the same structure

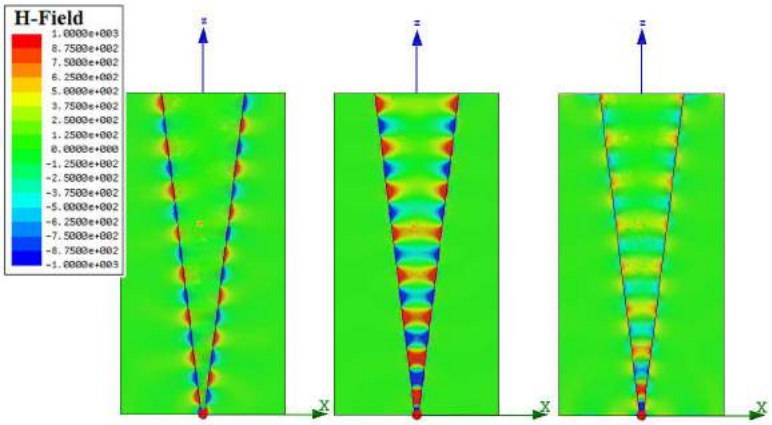

Figure 4.4: H-field components for a LTSA: Hx, Hy,Hz (HFSS).

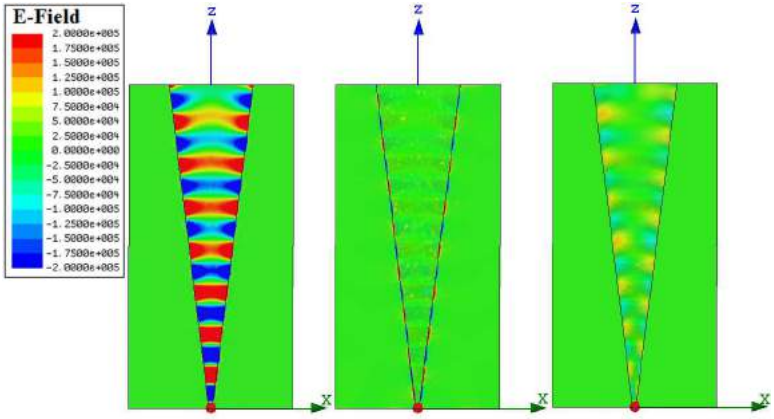

Figure 4.5: E-field components for a LTSA with PMC walls: Ex, Ey,Ez (HFSS).

as the electromagnetic field in a dielectric slab bounded by two PMC walls.

Physically, this hypothesis can be understood as follows: because of the thin substrate, the magnetic fields under the conductor must be orientated parallel to the electric conductor as it is illustrated in Figs. 4.7 and 4.8, so that the slot will appear to have PMC walls. In both cases it can be appreciated that the main components of the E-field are the X and the Z component, while the Y component is significantly weaker, which agrees with the assumption of the boundary condition of a PMC wall. In the physical LTSA system, the magnetic field is affected by the current flowing in the real thin electric conductor (PEC) at the edge of the slot, which locally resembles a current carried by a wire placed along the aperture edge. The

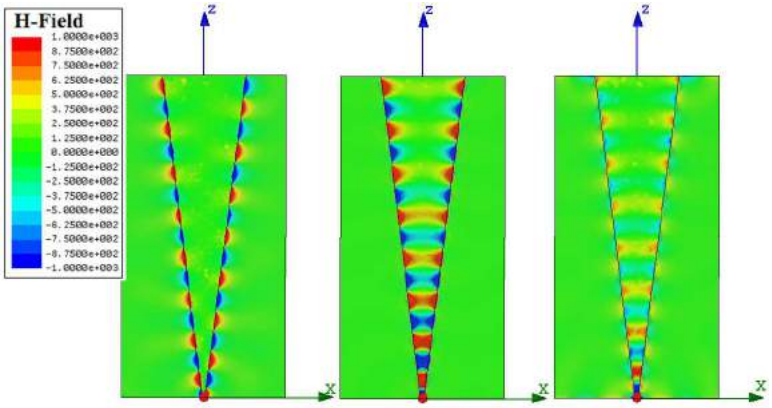

Figure 4.6: H-field components for a LTSA with PMC walls: Hx, Hy,Hz (HFSS).

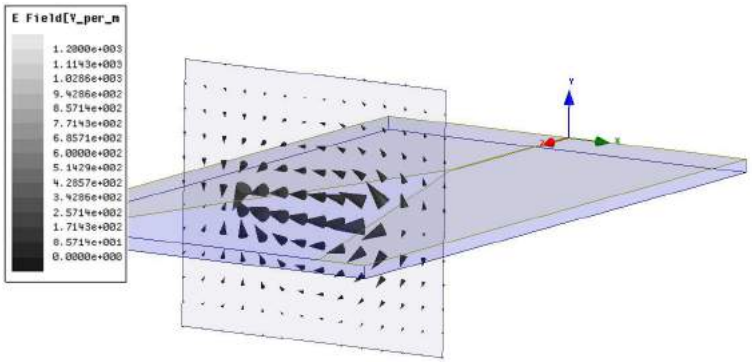

Figure 4.7: E field extracted from HFSS [117] on a plane perpendicular to the structure where the aperture is 1/2 of the final aperture.

direction of the magnetic field must be circumferential around this current, locally forcing it to point perpendicularly at the direction of the vertical plane whose orientation and location is defined by the edge of the electric conductor. This of course is consistent with the assumption of the PMC boundary, and plotted in Figs. 4.7 and 4.8.

4.2.3 Modes in the LTSA antenna

With the equations developed in Section 4.2.1 the different modes defined are presented in the current Section, and also associated with the modes that propagate in a LTSA according with the explanation above. As a proof of concept an analysis of a LTSA based on an $\epsilon_r = 2.56$ substrate ($\epsilon_n = 2.56$,

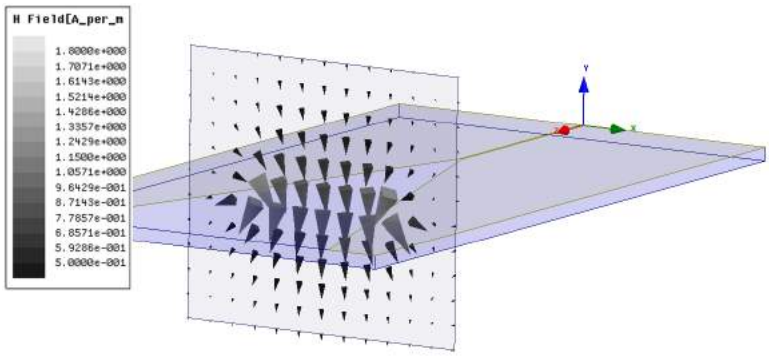

Figure 4.8: H field extracted from HFSS [117] on a plane perpendicular to the structure where the aperture is 1/2 of the final aperture.

$\epsilon_m = \epsilon_0$) working at 30 GHz is considered. The solutions obtained for the attenuation and propagation constants (α_y, k_y), and the $k_x = 0$ ($l = 0$) and $k_x = \pi/W$ ($l = 1$) cases, are shown in Fig. 4.9. The figure represents the modes for each variation of k_y. The first subindex is equal to l ($k_x = l\pi/W$) while the second subindex has either of the values 0, 2, 4,... for the even modes and 1, 3, 5,... for odd modes, where the solutions to the transcendental equations 4.8 and 4.20 are arranged according to their increasing values [86]. When $k_x = 0$ ($l = 0$), all the modes are TM_{0n}, as it is deduced from Eqs. 4.1, 4.2, 4.13 and 4.14. The first mode with real solution is the odd TM_{00}. In the same sense as discussed in [93], it is a solution to the equations but it can not be a guided mode. The next solution throws the even TM_{01} mode (illustrated in Fig. 4.10). However, it will not be considered compatible with the modal configuration of a LTSA due to the alignment of the fields and its radiation diagram. According to previous Section, the alignment of the fields on TM_{01} do not correspond to a LTSA configuration: the H-field of the mode is aligned in the X axis as given by Eq. 4.4, whereas the main component of the actual LTSA H-field is aligned in the Y direction (Figs. 4.7 and 4.8). Thus there will not be any coupling of energy to this mode. The physical model discussed in Section 4.2.1 also agrees with this, the currents at the edge of the electric conductor are incapable of exciting the TM_{01} mode in the substrate, as also seen in Figs. 4.7 and 4.8. Similarly, also the other modes for $k_x = 0$ cannot couple to the excitation field and currents because of their alignment, as deduced from the equations on Section 4.2.1.

For the case of $k_x = \pi/W$ ($l = 1$), on the other hand, all the modes are hybrid and can propagate through the structure, according with simulations in Section 4.2.2. The first mode that propagates is the HE_{11} mode. The same dominant hybrid mode propagation has previously been reported about other

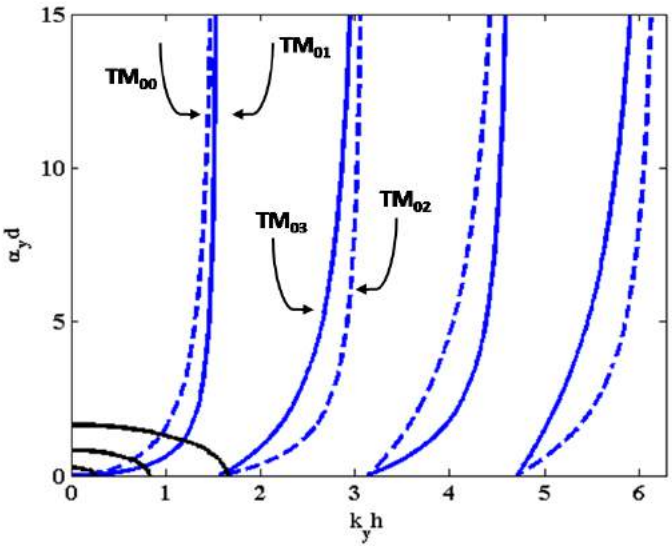

(a)

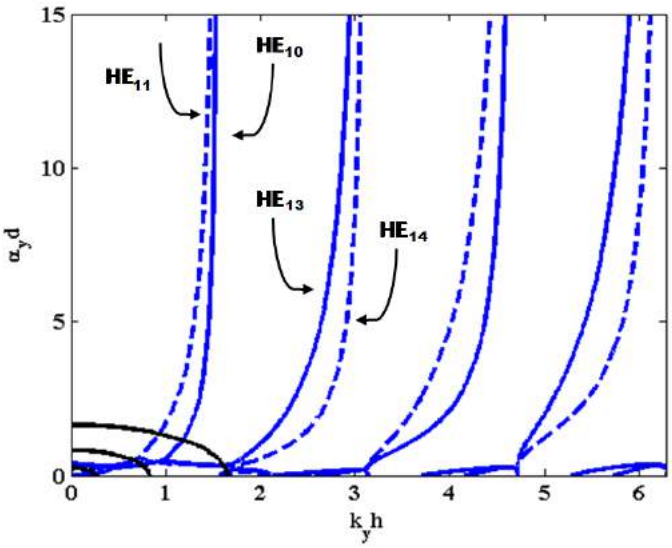

(b)

Figure 4.9: Mode charts for the attenuation and propagation constants (α_y, k_y), for (a) $k_x = 0$ ($l = 0$) and (b) $k_x = \pi/W$ ($l = 1$) (dashed = odd, continue = even).

structures based on dielectric waveguides [89, 118, 119, 120]. Thus, the HE_{11} is the fundamental mode for the structure, and the fields are shown in Fig.

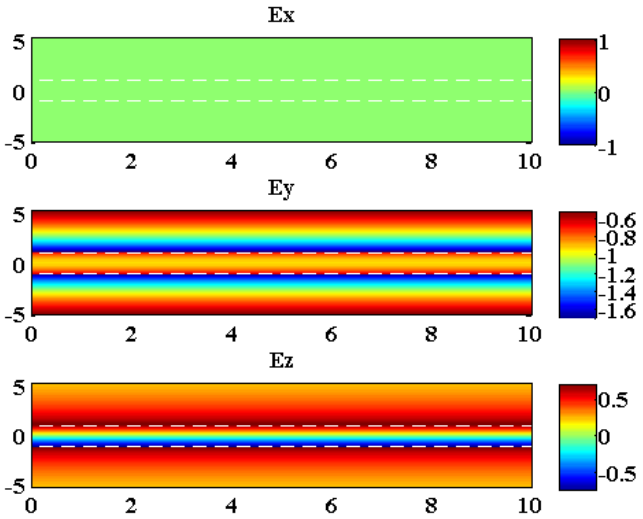

(a)

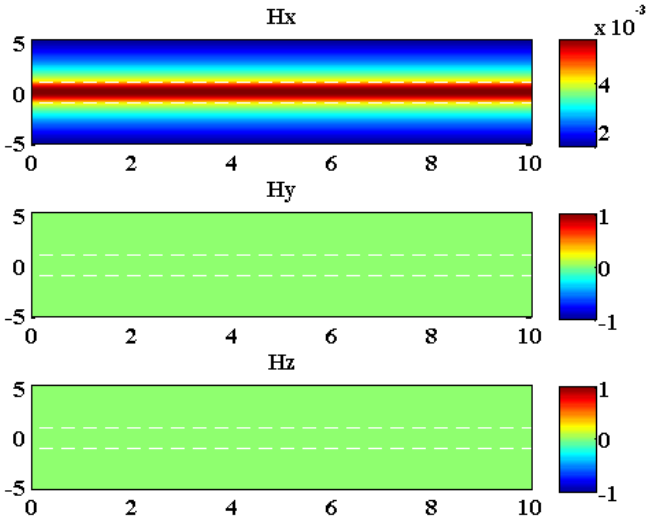

(b)

Figure 4.10: TM_{01} mode (magnitude on the left part in V/m and A/m, phase in radians on the right part).

4.11. This is also the first odd hybrid mode that propagates in the dielectric waveguide with PMC walls. The symmetry of this mode agrees with the field distribution inside the dielectric of a LTSA, shown in Figs. 4.7 and

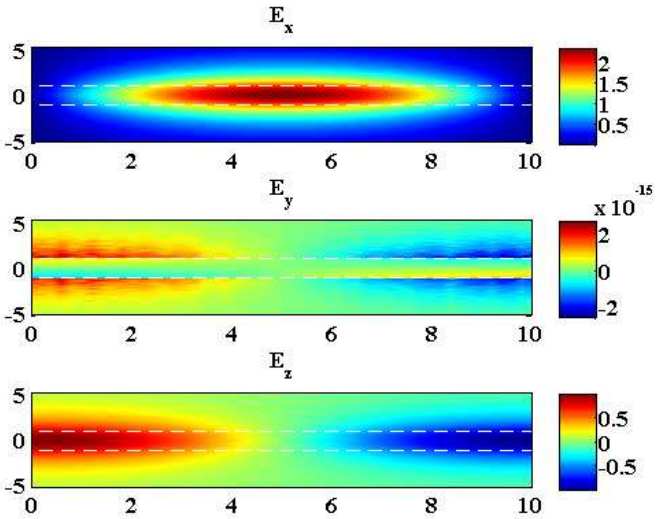

(a)

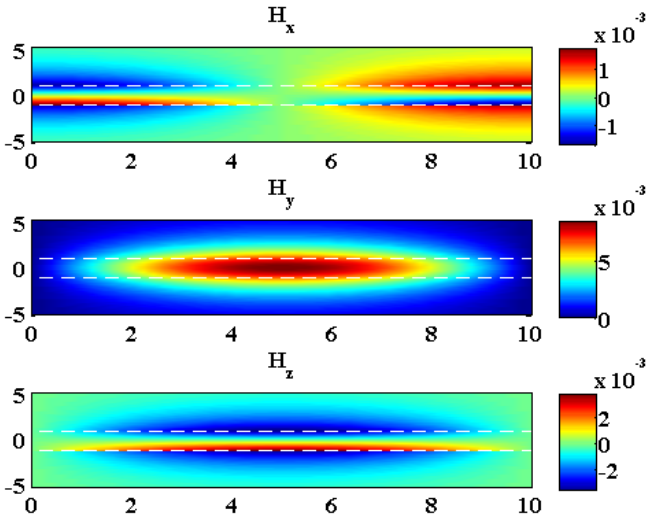

(b)

Figure 4.11: HE_{11} mode (magnitude in V/m or A/m on the left side and phase in radians in the right side).

4.8, and is consistent with the physical understanding of the LTSA as the mode is excited by the currents flowing at the edge along the aperture of the electric conductor. We can therefore assume that the antenna is equivalent

to a sectoral horn whose cross-section is a waveguide of the form discussed above in Section 4.2, i.e., a slab of dielectric between perfectly conducting magnetic walls and two dielectric-air interfaces and it is analogously treated to the way PEC sectoral horns are treated in horn theory [89, 119].

For fields propagation along the LTSA, it is assumed that the fields at the aperture will have the phase curvature determined by the slab length and shape of the sector, and no further scattering of the modes occur, as happens in metallic horns. This is consistent with the improvement of performance reported in the literature in Section 4.1 [89, 119]. The radiation pattern of such a sectoral horn is an end-fire pattern as in a LTSA antenna (Figs. 4.12 and 4.13). Thus, it can be concluded that a LTSA will support a hybrid HE_{11} mode that will produce an end-fire radiation pattern. The radiation pattern can then be calculated by the Fourier Transform of the fields present in the aperture.

The next propagating mode for the case of $k_x = \pi/W$ ($l = 1$) is the HE_{10}. The field distribution in this case, being an even mode, is not compatible with the field distribution on the antenna since it does not have the same symmetry, thus it can not be excited by the currents flowing along the electric conductor edge.

In a similar way to HE_{11}, the modes with $k_x = l\pi/W$ ($l \neq 0$), that are hybrid modes that can propagate through the structure. However, other secondary modes, such as the TM_{01}, HE_{10} or HE_{12} that in theory could propagate in the structure, are not excited by the currents flowing along the edge. As the width of the slot increases when the fields are away from the throat, other higher order hybrid modes with higher values of l that can propagate could be excited. Although all these modes can propagate through the LTSA depending on the number of the constant k_y, the number of allowed solutions that satisfies the transcendental equation increases. However for correct operation of the LTSA only one value of k_y should be allowed i.e. the substrate should be thin so only one solution can propagate.

The conclusion therefore is that when this antenna works properly, most of the power is coupled to the HE_{11} mode. On the other hand when either the working frequency increases, the dielectric permittivity is higher or the substrate is thicker, then power coupling to the higher order modes HE_{1n} (n odd and n>1) becomes possible and the antenna will radiate not only with an end-fire pattern. All the three variations mentioned correspond to an increase of the effective thickness described by [97, 98] and go beyond the limit for end-fire radiation.

The degradation of the radiation for this antenna when the substrate is

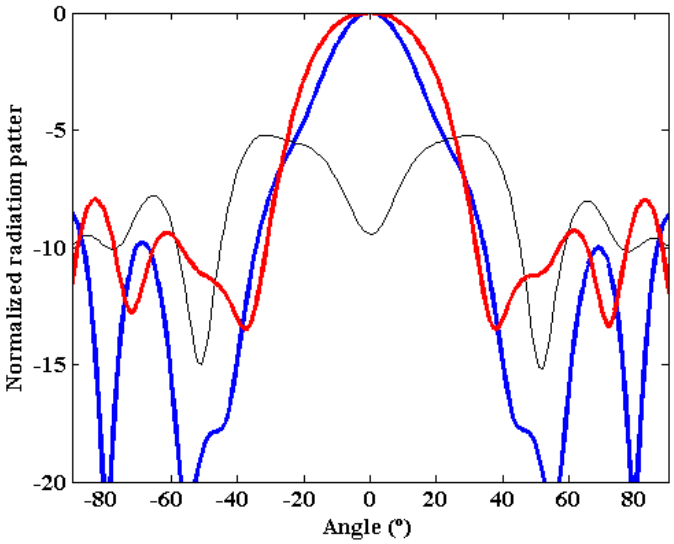

Figure 4.12: E plane radiation pattern for $t_{eff} = 0.03\lambda_0$ (blue), $t_{eff} = 0.08\lambda_0$ (red) and $t_{eff} = 0.16\lambda_0$ (black)

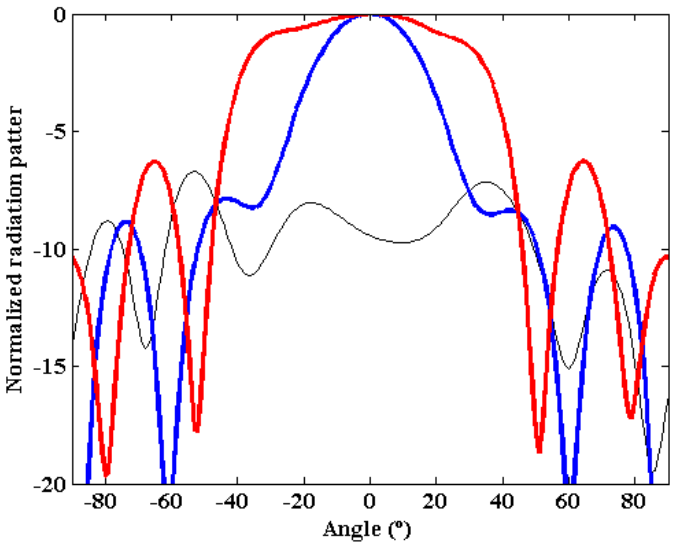

Figure 4.13: H plane radiation pattern for $t_{eff} = 0.03\lambda_0$ (blue), $t_{eff} = 0.08\lambda_0$ (red) and $t_{eff} = 0.16\lambda_0$ (black)

thicker is exemplified in Figs. 4.12 and 4.13 for E and H planes respectively. These simulations correspond to effective thickness of $0.03\lambda_0$, $0.08\lambda_0$ and $0.16\lambda_0$ respectively. The plots illustrate how the Yngvensson limit arises. This

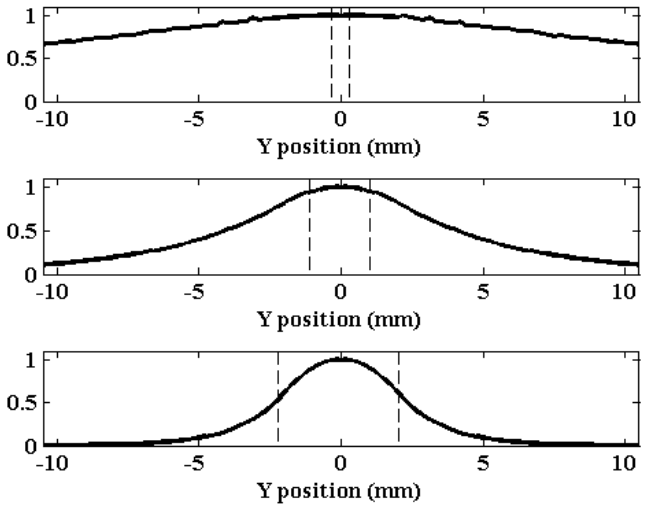

Figure 4.14: H_y component of the field in the center of the waveguide, represented by dashed lines.

limit predicts a degradation of the pattern beyond $0.03\lambda_0$. As the substrate gets thicker, the directivity decreases and the beam becomes less symmetric. In Figs. 4.12 and 4.13 we show that the radiation is degenerated for the case of $0.08\lambda_0$ with respect to $0.03\lambda_0$, but the antenna still have an end-fire radiation. This also corresponds to the second solution in Fig. 4.9. For this second case, the only propagating mode is still the fundamental but the attenuation constant α_y has increased. As the substrate gets thicker, the directivity decreases and the beam becomes asymmetric. When the substrate is thick enough to allow higher order modes (third example in Fig. 4.9) the energy couples to this modes, giving a non end-fire radiation pattern as a result, as for $0.16\lambda_0$.

The field is much more confined in the vertical Y direction normal to the dielectric-air interface when the substrate is thicker, since the attenuation factor $exp(-\alpha_y)$ associated to the fields drops dramatically with Y. Actually, the Yngvesson limit cuts in quickly as the radiation pattern symmetry begins to degenerate. The variation of this attenuation constant is not strong within the limits. This phenomenon is illustrated in Fig. 4.14.

Regarding the field distribution in the center of the slot, plotted in Fig. 4.14, the assymetry of the beam as the substrate gets thicker [97] can be justified. The field distribution is symetrical from the center of the slot in both Y directions. When the thickness of the substrate increases, the magni-

tude of the field distribution extrictly inside the slot, is exponential, causing therefore the asymmetry on the beam, even if only the fundamental mode is propagating.

If it is made a more detailed analysis, it can be seen that in the dielectric core itself, at the aperture, the field varies as $cos(k_y y)$ function (Fig. 4.14), and therefore drops by a factor of $cos(k_y h)$ between the center of the slab and the edge (in the vertical Y direction). For thin slabs the value of $cos(k_y h)$ is not much different from the maximum of unity and therefore the field extends over significant area into the free space volume in either sides of the slab. When the substrate gets thicker, $k_y h$ approach $\pi/2$ so the field at the edge is a small fraction of the maximum, effectively confining the field on the slab. That implies that the radiation pattern becomes much broader in the H-plane with dielectric slab thickness resulting in an asymmetric radiated beam. For the particular example we are using in this manuscript, the Yngvesson limit gives a value for $k_y h = \pi/12$ so according to Eq. 4.17, the term $cos(k_y y)$ will vary between 1 and 0.96. That means that the tapered field in the Y direction only drops to 96% of its maximum strength at the dielectric-air boundary. It then falls off as $exp(-\alpha_y)$ outside, because the attenuation constant is small, the field extends well into the free space region. The value of y that corresponds to this value of k_y is also $\pi/12$, giving a variation of 76% in energy. This fact constitutes an analytic explanation to the Yngvesson limit, also agreeing with the asymmetrization of the beam when the substrate is thick.

It also helps to explain the introduction of periodic holes in the substrate of a TSA [107]. The effective dielectric permittivity is reduced so the Yngvesson limit can be satisfied. More power is coupled into the HE_{11} mode and less power to the higher order modes.

Finally, the radiation mechanism presented in [102, 103, 104] and [109, 110] of a LTSA without dielectric can also be explained due to a TEM and a TE mode (there was no E_y component). This can be demonstrated thanks to the hybrid mode theory by considering the HE_{11} mode to degenerate into a TEM mode without any E_y component as was shown in [109, 110].

An analytic explanation of the electromagnetic radiation mechanism of a LTSA antenna has been presented. This work has been applied to a LTSA without any loss of generality and just for simplicity in comparison with the TSA. This is valid since the difference between the TSA and the LTSA is the design of the edge that mainly affects the performance of the radiation pattern (gaussicity and symmetry of the E and H planes). In next sections, several applications for this method are presented.

4.3 Applications to practical cases

After the theoretical analysis, some applications have been developed based on designing methods for waveguides and in the previous theory. The main asumption is that the antenna does not work once the structure allows the propagation of more than the fundamental mode due to its electrical dimensions. Some techniques for suppressing the high order modes are: modifying the structure to eliminate high order generated modes; cancel main components; add filters on the antenna, etc.

As the main drawback of photomixers is their implementation on high permittivity substrates, the need of thin wafers of a few micrometers for this kind of antennas makes difficult its implementation. Also, while the antenna needs a very thin substrate, the photomixer needs a fairly thick support structure, not only due to the robustness of the system but due to heat dissipation and efficiency of the device. The best solution is to optimize the performance of the feed device itself, and develop some methods for canceling undesired propagation modes as explained before. On most examples, these photomixers are used in the practical implementation of the structures, while in others, diodes implemented on high permittivity substrates are also employed.

4.3.1 Wedge antenna

The first solution is based on the idea of implementing the feed of the antenna, an interdigitated photomixer, in a high permittivity substrate, while the antenna itself is printed over a wedge of a low permittivity plastic material, such as PVC or Teflon ©, to allow the radiation of the TSA. This solution complies with the requirements for both devices: photomixer implemented over high permittivity and thick substrate and antenna over low permittivity and effective thickness.

The effective thickness of the photomixer substrate, is calculated with Eq. 4.30 taking into account a photomixer processed III-V compound semiconductor ($\epsilon_r \approx 13$), with a typical thickness of several hundreds of microns. The value is 1.72 λ_0 at 1 THz, which results to be much higher than the limit predicted in previous studies [104, 97]. As a consequence the substrate prevents TSA antenna type from end-fire radiation.

$$t_{eff} = t(\sqrt{\epsilon_r} - 1) \tag{4.25}$$

One could argue that the photomixer substrate might be thinned to few microns in order to fulfill the thickness condition. The thinned photomixer

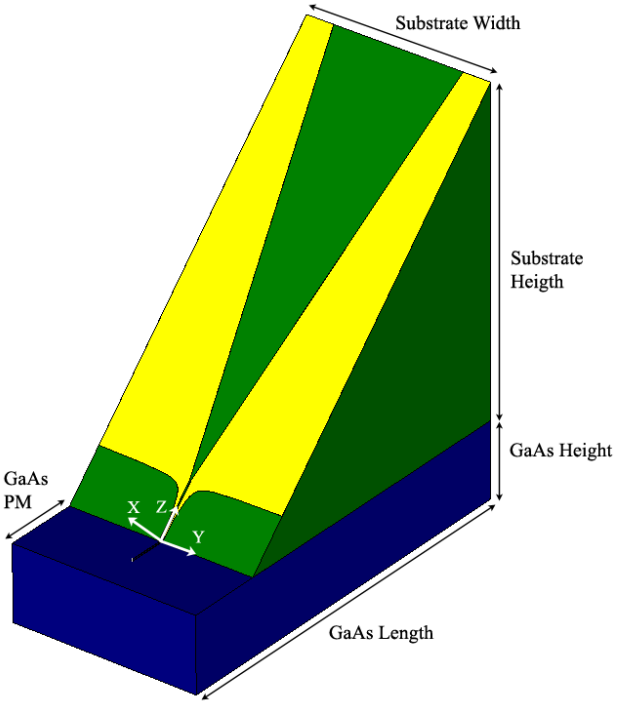

Figure 4.15: Complete structure.

substrate could be then glued on a low dielectric permittivity substrate. Unfortunately, since the photomixer is illuminated by a relatively large optical power (several tens of mW) [115] in an active area of a few microns, in order to optimize thermal flow it is necessary to avoid thermal interfaces in the regions underneath the photomixer (i.e. several microns under the illuminated surface). As a consequence the substrate thinning option should be discarded.

The fact that the photomixer substrate is a III-V compound semiconductor causes an important difficulty for the use of a TSA as a radiating element: it is mandatory to isolate the photomixer and antenna substrates, otherwise the wafer would act as a substrate of the antenna thereby preventing from end-fire radiation. This constraint can be overcomed by processing the TSA over a wedge of a low loss polymer material (Polymethylpentene TPX) with $\epsilon_r = 2.2$ as shown in Fig. 4.15. Two goals are satisfied with this geometry: first, the wedge acts as a substrate for the TSA and second, it prevents the radiation from the TSA from "seeing" the photomixer substrate.

The elevation angle of the wedge is of special relevance. If this angle is small, the proper isolation from the photomixer substrate is not achieved,

being affected by its properties and preventing radiation due to the high effective thickness specially in the high band. Also, a secondary lobe appears due to the radiation over the photomixer substrate. On the other hand, if the elevation angle is large, the thickness of the TSA substrate becomes higher, also preventing radiation of the TSA. If the elevation angle is near 90^o, the thickness of the substrate tends to be larger than the previously explained limit, but due to the excitation of the photomixer, that is performed by a pigtailed optical fiber, blockage and perturbations on the radiation pattern might occur, since the maximum of the radiation diagram will be directed to the optical fiber path.

The chosen elevation angle for the wedge substrate is 45^o. With this angle, the radiation patterns with the lowest Side Lobe Level (SLL), highest directivity and lowest misalignment of the main lobe depending on frequency are achieved over a wider bandwidth according to simulations. Within the TSA radiating area, the t_{eff} ranges from $0.17\lambda_0$ $(50,7mm)$ to $1.4\lambda_0$ $(408,3mm)$, which in fact exceeds in a factor between 50 and 1000 times the limitation stated before. Clearly, due to this novel design, the substrate thickness limitation has been overcomed, making it possible the practical manufacturing of a photomixer-fed tapered slot antennas at Terahertz frequencies.

Once the substrate effective thickness limitation has been solved, some design issues arise due to the characteristics of the technology employed. First of all, due to the different antenna and photomixer substrates, it is necessary to design a feeding region that maximizes the energy flow from the generator to the antenna. In addition to the maximization of the energy delivered to the antenna: since the kind of photomixers employed have input impedance of the order of several $K\Omega$, it is desirable to achieve an input impedance as high as possible.

The geometry chosen for the feeding region determines the input impedance and the energy delivered to the TSA. The shape of the feeding region has an influence over the radiation characteristics of the antenna. Fine adjustments in the geometric parameters of the feeding region have no significant influence on the radiation pattern. The constraints for the design of this region are the angle of the wedge where the TSA is printed, and the requirements of the photomixer (detailed below).

The illumination of the photomixer is performed by a single mode fiber optic which is pigtailed to the device by an optical UV curing adhesive. The fiber optic contains the two wavelengths whose shift in frequency is generated in the photomixer. The dimensions of the fiber impose a limitation on the distance at which the wedge must be placed from the feed device: at least a distance equal to the radius of the optical fiber, to allow the mechanical

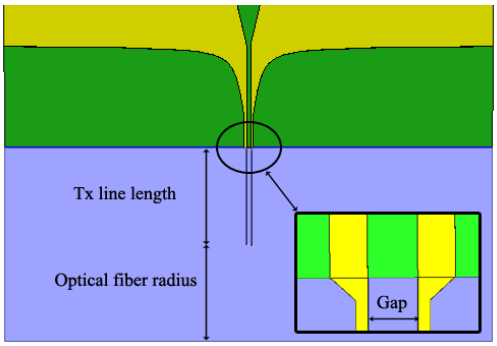

Figure 4.16: Detail of the feeding region. Transmission line length=100 μm, optical fiber radius=100 μm

alignment.

The high photomixer impedance causes a mismatch when coupling to antenna, which has an input impedance of hundreds of Ohms. Due to this reason, the design of the transmission line must be accomplished according with this feature. The typical input impedance of a tapered slot antenna depends on the geometry of the feeding region and also on the substrate dielectric constant and effective thickness [103], and is around 200 Ω for this case, so the highest possible input impedance must be achieved, preserving the radiation characteristics of the antenna in order to have the lowest possible mismatch. This should be done in the most broadband possible, to exploit the broadband radiation properties of the antenna.

In addition, an optimal transition in the coplanar strip (CPS) transmission line should be designed for coupling the power from the CPS on the photomixer substrate to the CPS on the TSA substrate. Regarding the practical manufacturing of this transition, due to alignment purposes between both CPS, a minimum metallization width of 3 μm has been considered.

In order to ease the CPS transmission line transition, a taper has been implemented in the CPS coming from the photomixer substrate, as illustrated on Fig. 4.16. This taper structure minimizes the losses and at the same time the radiation efficiency and TSA input impedance are maximized. It allows at the same time to facilitate the integration procedure between the wedge and the photomixer substrate.

The design of the transmission line on the high permittivity substrate will limit the radiation efficiency of the antenna due to radiation losses, so it is desirable that the length of the transmission line is maintained as short as possible. As stated before, the photomixer pigtail imposes a minimum length

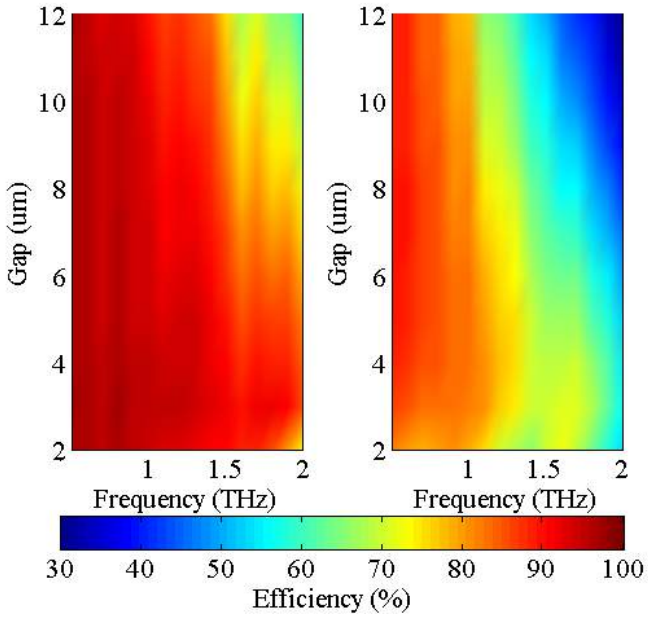

Figure 4.17: Radiation efficiency in terms of the gap variation and frequency, for the whole structure (right) and for the LTSA over the plastic substrate only (left).

for the CPS transmission line equal to one radius of the fiber (62.5 μm). In order to have some margin and since due to capillarity the optical adhesive smears out several tens of microns around of the pigtail position its allowed 100 μm for the CPS transmission line length (see fig. 4.16). For a CPS line, the lower the gap between lines and the lower the line width, the higher the characteristic impedance of the line [121]. Nevertheless, for this application, is necessary to design the CPS also paying attention to the high radiation losses, which lower radiation efficiency of the structure.

A parametric study of the two free design parameters of the CPS has been carried out. The gap and the line width, were chosen in order to: first, minimize the looses on the substrate and second, to maximize the input impedance. Figures 4.17 and 4.18 shown both parameters in terms of the frequency and the variation of both the gap and the line width. In both figures, the radiation efficiency is shown for the whole structure (CPS and TSA) and only the portion of the structure on wedge substrate. For this study, a constant linewidth was employed, i. e., same linewidth for both the CPS photomixer substrate and the wedge substrate.

When considering the TSA without the CPS on the photomixer substrate,

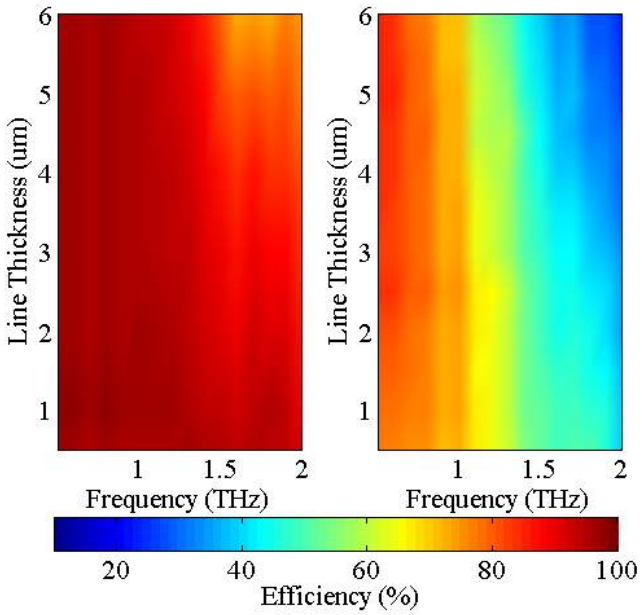

Figure 4.18: Radiation efficiency in terms of the line width variation and frequency, for the whole structure (right) and for the LTSA over the plastic substrate only (left).

it is clear from Figures 4.17 and 4.18 that changes in the line width and the gap of the CPS on the wedge substrate have almost no influence on the radiation efficiency –which lies over 80% in almost the whole band. When simulating the structure with both substrates, the line width and the gap play a major role in the radiation efficiency, since these parameters determine the radiation losses in the CPS on the photomixer substrate.

As the gap decreases, the input impedance increases [121]. A minimum gap has been chosen which preserves the efficiency. With a gap of 4 μm, the input impedance is maximized whereas the radiation losses over the maximum bandwidth are minimized. The radiation characteristics of the antenna are maintained.

Regarding the line width, it should remain as thin as possible. The width of the CPS lines on the photomixer substrate has been chosen to be 1 μm. Smaller values influence negatively the yield in the lithographic process and might trigger electromigration. As explained before, there should be a minimum width of 3 μm in the transmission line on the junction between CPS on the photomixer and wedge substrates. This has been achieved by including a taper (see Fig. 4.16) in the last section of the CPS on the photomixer

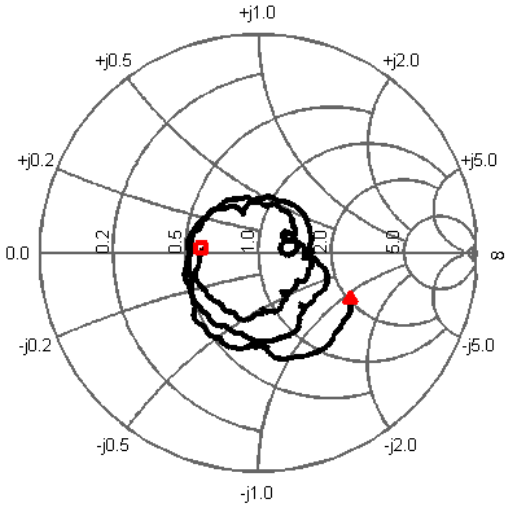

Figure 4.19: S_{11} parameter normalized to 75 Ω. Ending point: 2 THz (square), Starting point: 0.6 THz (triangle).

Table 4.1: Feeding region parameters.

Parameter	Value (μm)
Line Gap	4
Line Width GaAs	1
Line Width Substrate	3
Transmission line length in GaAs	100
Optical fiber radius	100

substrate.

A constant width line can not be applied to this design due to the high losses and the low input impedance that result, especially in the high band.

The details of the feeding region are shown in Fig. 4.16. The relevant parameters are listed in Table 4.1.

In order to provide a soft transition from the CPS to the TSA, a tangential shape has been employed. The curve defining this shape is given by Eq. 4.26, where the smoothing factor in the denominator corresponds to the profile of the taper.

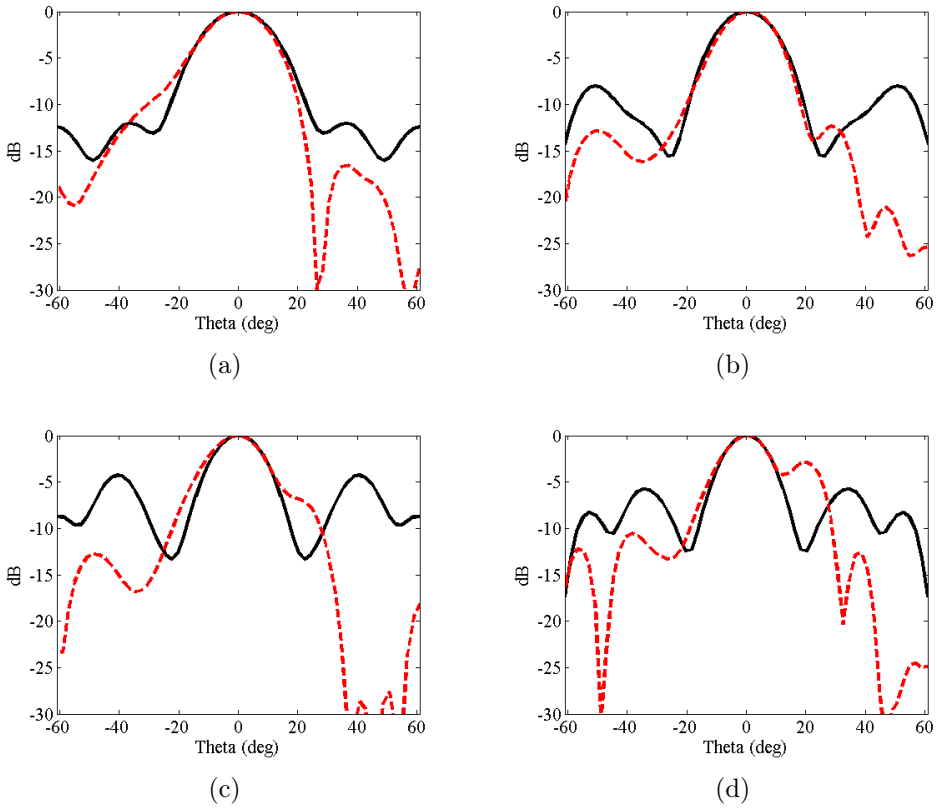

Figure 4.20: Normalized radiation patterns for the E (solid) and H (dashed) planes. (a) 1 THz, (b) 1.2 THz, (c) 1.4 THz and (d) 1.6 THz.

$$y = \frac{Taper\_Width}{\frac{\pi}{2}} arctg\left(\frac{x - gap - Tx\_line\_width}{Smoothing\_factor}\right) \tag{4.26}$$

If the smoothing factor is low, the transition from the line to the TSA becomes more abrupt. This factor has been optimized in order to minimize the losses and maximize the radiation efficiency.

With the parameters detailed before, the input impedance of the TSA over the operation bandwidth is shown in Fig. 4.19. The real part is between 150 Ω and 50 Ω, over the whole operation band, being 100 Ω at the central frequency. This input impedance is two orders of magnitude below the output impedance of the photomixer. Regarding the imaginary part, it oscillates around 0 Ω, which is typical for this type of antennas.

Once the feeding region is designed, the remaining parameters correspond to the shape of the antenna. These parameters define only the radiation

Table 4.2: LTSA parameters.

Parameter	Value
Length	3.5 λ_0
Aperture angle	19^o
Total width	1.67 λ_0
Substrate height	2.8 λ_0
GaAs height	200 μm
GaAs length	3.5 λ_0
GaAs PM	200 μm

characteristics of the TSA and do not have any influence over the input impedance, which is determined by the feeding region.

The main goals for the shape optimization are: maximum operation bandwidth, symmetrization of the radiation patterns in the maximum possible bandwidth and achieve the maximum gain in the operation frequency band.

For optimizing the gain, a linear shape for the TSA has been selected [97]. The remaining goals are achieved with the optimization of the parameters of the LTSA, as the length, aperture angle and total width. With these parameters, the frequency range of operation is set up, and also the main characteristics of the radiation patterns, as the -3 dB beamwidth, and the minimization of the SLL.

The length of the LTSA (3.5 λ_0) has been chosen by optimizing the operation on the widest frequency range possible, including 1 THz as a central frequency. With this length, the lowest secondary lobes, specially in the H plane are achieved.

The aperture width is set to 1.17 λ_0 and the total width (substrate width in Fig. 4.15) to 1.67 λ_0. These last two values also set up the operation band of the TSA. If the aperture angle is reduced, the operation frequency band shifts to upper frequencies [97].

Symmetric radiation patterns at -3 dB levels have been achieved from 1 THz to 1.8 THz. In Fig. 4.20 the radiation patterns at four of these frequencies are shown. The -3 dB beamwidths for both main planes of the antenna in the whole operation band are shown in Fig. 4.21. These beamwidths can be modified by adjusting the shape of the TSA according to [97]. This design achieves one octave with a broadband symmetric radiation pattern, (ranging from $0.9 - 1.8$ THz). There is an asymmetry in the H-plane in the radiation

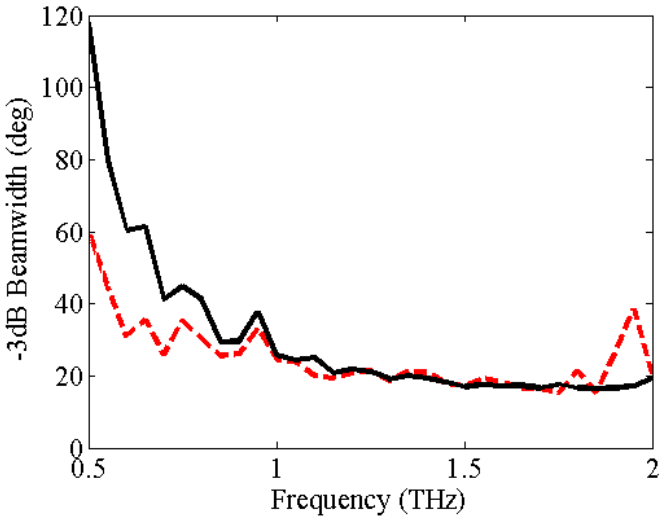

Figure 4.21: $-3\ dB$ beamwidths for the E (solid) and H (dashed) planes in terms of the operation frequency.

patterns. This asymmetry arises from the thickness of the wedge substrate. It produces a secondary lobe in the high band of the antenna. Nevertheless, it remains below $-5\ dB$ in the whole operation band.

The gain of the antenna is shown in Fig. 4.22, whose maximum is 14.2 dB at 1 THz. The radiation efficiency is also shown, and it has been optimized with the feeding region parameters for 1 THz.

The operation frequency band goes from 0.6 THz to 2 THz with end-fire radiation patterns. These upper and lower limits are given by the shape (i.e. the aperture angle), due to the worse radiation characteristics. The frequency range of operation is set up with these parameters in order to achieve symmetric end-fire radiation patterns, both in the high and in the lower band.

At Terahertz frequencies, the use of the Quasioptical approach is important in terms of the system design [122]. The gaussicity of the antenna is analyzed as defined by [80, 123] and listed in Eq. 4.27 on its far field expression, where $F(\theta, \phi)$ is the electric field in the far-field pattern of the antenna. The coupling efficiency is defined as the inner product between the radiation pattern and the fundamental gaussian-beam pattern in the angular domain. More about this topic will be described in Section 5.2 together with acceleration and numerical methods.

$$\nu_{Gaussicity} = \frac{|\int\int[\epsilon_{co}F(r,\phi)]e^{(\theta/\theta_0)^2}e\sin(\theta)\mathrm{d}\theta\mathrm{d}\phi|^2}{\int\int|F(\theta,\phi)|^2r\mathrm{d}r\mathrm{d}\phi\int\int e^{-2(r/w(z))^2}r\mathrm{d}r\mathrm{d}\phi} \tag{4.27}$$

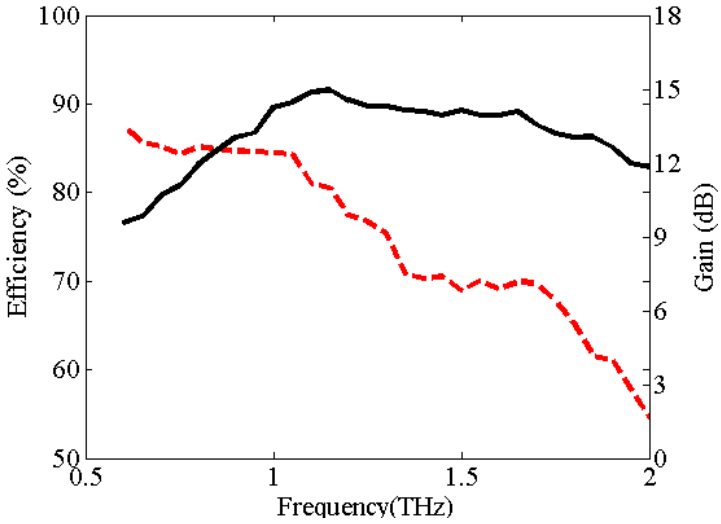

Figure 4.22: Radiation efficiency (dashed) and Gain (solid) in terms of the frequency

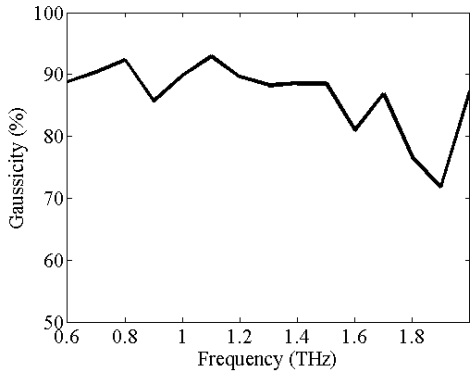

Figure 4.23: Gaussicity for the different operation frequencies

The results for this efficiency are shown in Fig. 4.23. The gaussicity of the beam is over 85% over the whole operation frequency band. The maximum value is achieved at 1.1 THz with 93% gaussicity, agreeing with the maximum gain and symmetrical patterns frequencies.

Due to manufacturing and measuring limitations, and equipment available at that moment, the antenna has been implemented on a prototype at 50 GHz as central frequency in detection regime. For this prototype a commercial schottky diode has been employed for detection.

The measurements have been made in an anecoic chamber, measuring

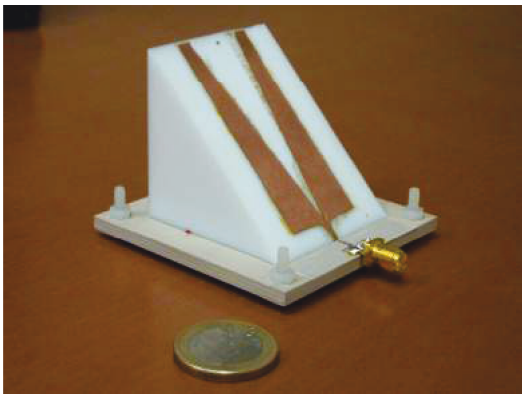

Figure 4.24: Prototype at 50 GHz

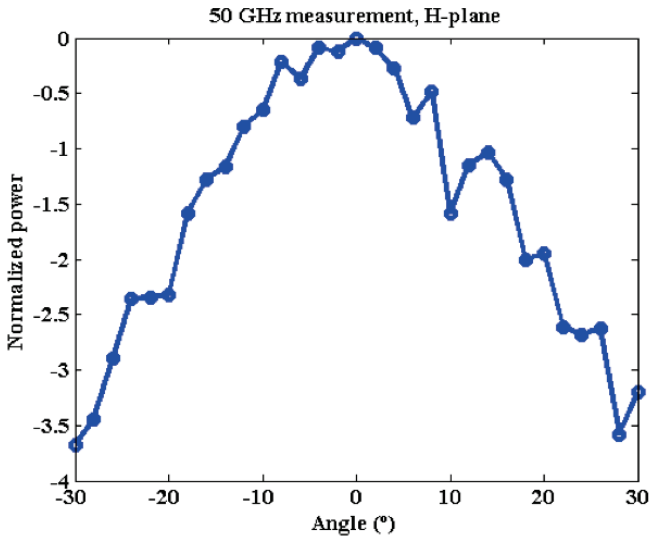

Figure 4.25: H-plane measurements for 50 GHz

the DC power received when transmitting at 50 GHz. Due to the rotational system employed for measurement, only the H-plane has been characterized, showing the results in Fig.4.25. The radiation pattern of the H-plane wich is the most critical due to the architecture of the device is demonstrated to be symetric, allowing the use of this solution in a higher frequency regime.

4.3.2 TSA over an EBG substrate

In the current Section, an application of the previous theory is developed by means of cutting off modes that propagate on a thick substrate too, but

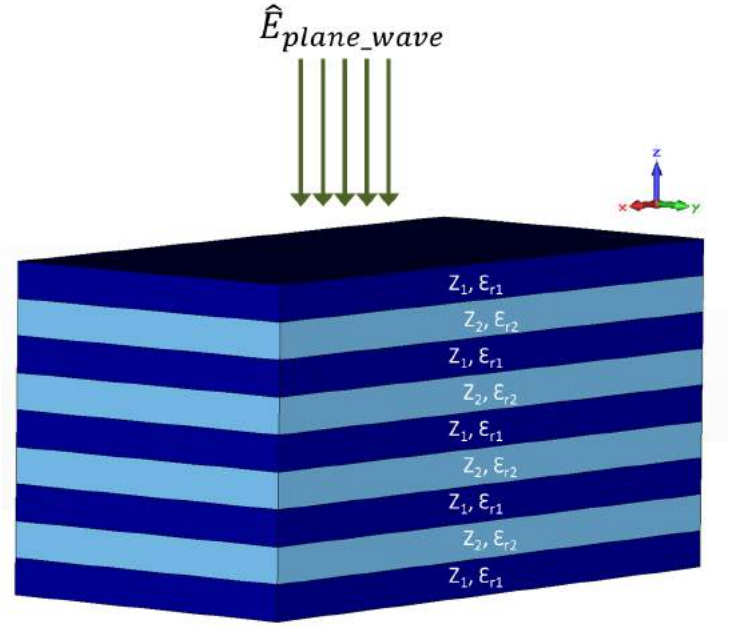

Figure 4.26: Example of an EBG structure

with an Electromagnetic Band Gap (EBG) aproximation. The theory for this application can be understood from two perspectives: the reduction of the effective ϵ_r of the substrate, or the behaviour as an EBG of the structure, cutting off the vertical component of the modes on the substrate. It is important to note that these kind of structures should have its cut-off frecuency within the operating frequency of the antenna. The drawback of this solution is the extremely narrow band operation of these kind of structures, that only operate in a very restrictive range of frequencies when tunned.

The geometry of the design is based on placing several layers of dielectric on top of each other with different dielectric permittivities and thickness, as shown in Fig. 4.26, alternating two effective thickness of the layers as a periodic structure. In this Figure, there are considered combinations of ϵ_r and thickness, having therefore a different Z_0 on each layer, that repeats periodically [124, 125]. Several structure types are studied with the aim of characterizing the behavior of the structure. For this purpose, the reflection coefficient is calculated according to Eq. 4.28. The simulation has been performed with CST Microwave studio [81] and the electric field results on the illumination of the structure with a plane wave, as illustrated in Fig. 4.26. The electric field probes (one on each axis) are located in the Z^+ direction, in order to compute the reflection coefficient of the structure [124, 125].

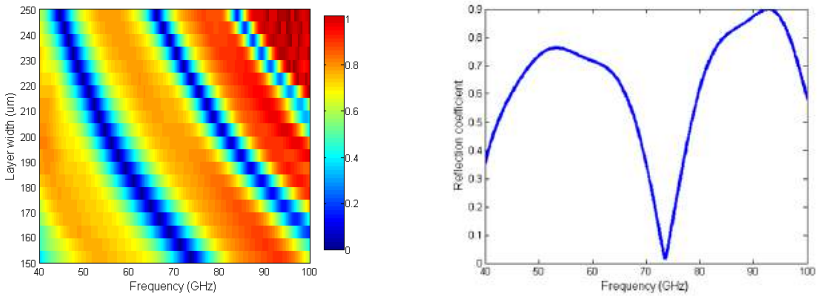

(a) (b)

Figure 4.27: Reflection coefficients for 3 periods of stacking layers with $\epsilon_{r1} = 12.9$ and $\epsilon_{r2} = 2.2$ in terms of frequency and substrate width

$$\Gamma = \frac{E^-}{E^+} \tag{4.28}$$

The theory explained in Section 4.2 also matches the hypothesis of an EBG behaviour. The high order modes, that have a strong transversal component are the ones responsible of the non-end fire radiation of the TSA antenna. With this EBG, these components are eliminated, having no modes with this field configuration. The transversal direction agrees with the dicrection where the EBG is composed ($\hat{z}$). According to the previous theory, this component is suppressed, so all the power is concentrated again on the fundamental mode, allowing end-fire radiation. To show this characteristic, the vertical component of the $\vec{E}$ field is plotted on Figs. 4.30 and 4.31, as an example. These fields will be explained later with more detail for the specific structure.

Different parametric studies have been performed to obtain the behavior of the structure as an EBG, specially to compute precisely the working frequency band and to check the theoretical results obtained by previous authors [124, 125]. The variation parameters are Z_0, by changing the thickness, ϵ_r of each of the layers and also the number of periods. It is expected that the narrowband properties of the structure are strengthen by the increasing periodicity [126], so the selectiveness of the resulting filter is higher and also with more resonances within the band, while the main operating frequencies will be set by a trade off between the Z_0 of each layer and the number of periods. Two examples of these parametric studies are shown in Figs. 4.27 and 4.28.

For the case of Fig. 4.27, where the stacking is composed of three periods,

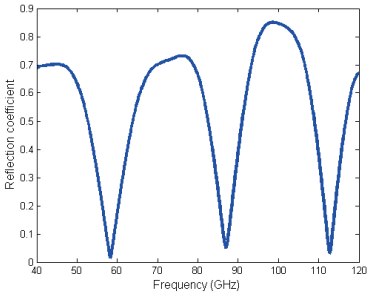

(a) (b)

Figure 4.28: Reflection coefficients for 6 periods of stacking layers with $\epsilon_{r1} = 12.9$ and $\epsilon_{r2} = 2.2$ in terms of frequency and substrate width

4 layers of $\epsilon_r = 12.9$ and 3 layers of $\epsilon_r = 2.2$, there are two possible operation bands, with one resonating frequency. The first between 45 GHz and 65 GHz and the second between 80 GHz and 100 GHz, considering a reflection coefficient of more than 0.5. The coefficient of Fig. 4.27(b) corresponds to a layer thickness of 150 μm.

In Fig. 4.28 another example is shown, in this case with a period of six layers, 7 corresponding to $\epsilon_r = 12.9$ and 6 layers to $\epsilon_r = 2.2$. For these conditions, there is one resonance more (if we focus on the same band as for the 3 periods case) and the operation bands are reduced in bandwidth: the first one is between 65 GHz and 80 GHz and the second between 95 GHz and 105 GHz.

These simulations are an example of how the reflection coefficient behaves in frequency and with the variation of the layer thickness. The selection of these two substrates lays in the easyness to find a feed for the antenna manufactured in a very high permittivity substrate [79] and the several Teflon substrate options avalilable for microwave applications. These materials can be replaced by similar ones with analogous properties.

Another tunning parameter is the variation on the thickness ratio between the high and low permittivity substrate, i.e. in the previous example, the ratio was 1 : 1, but this can be modified to achieve the desired impedance on each layer and the reflection coefficient on the bands. All these results are obtained for frequencies centered in 80 GHz, when the thickness of each of the layers is comparable to the wavelength, so the results could be applied to practical cases as described in next section.

With this setup, the operating frequency band is still narrow, but the tolerances to component mismatch are higher. In next sections, it will be

demonstrated that an antenna printed on an homogeneous equivalent substrate with the effective ϵ_r and thickness would not radiate in an end-fire configuration as its well beyond the theoretical physical limits.

As the objective of this Section is to design a TSA with a higher overall dielectric thickness, the EBG structure from previous studies will be employed as the substrate for several TSAs, including array configurations and different shapes of the antenna to compare performances.

Due to manufacturing purposes, the chosen working frequencies would be in the [60 - 100] GHz band, therefore simulations are also carried out within these frequencies and the antenna is feed with a CPS line adapted to 50 Ω. Two TSA shapes are used: vivaldi (with an exponential aperture) and linear (LTSA).

The substrates chosen to accomodate the frequencies selected are Rogers® 3010 and Rogers® 4450F. These materials are 0.127 mm and 0.202 mm thick and have $\epsilon_{r1} = 10.2$ and $\epsilon_{r2} = 3.52$ respectively. These substrates can be found on the market and are easy to proccess. Also, the characteristics of Rogers® 4450F (Prepeg) allows the stacking and gluing of all the layers. The antennas were printed on copper on the outer layers of the dielectric.

The reflection coefficient for this strucutre between 60 GHz and 100 GHz is shown in Fig. 4.29. The operating frequencies for this particular stacking are between 65 GHz and 85 GHz where the reflection coefficient is 1 or close to this value (at least more than 0.5). If the frequencies are those that $\Gamma > 0.6$, the obtained bands are $62 - 86$ GHz and $108 - 120$ GHz. Beyond 120 GHz the antenna is not simulated due to the upper limit bandwidh of the schottky diode.

According to previous works [97], the aperture of a TSA should not be larger than λ_{eff}, where λ_{eff} is the effective wavelength on the substrate to obtain the best performances in terms of directivity and symmetrization of the beam. Also, the length of the TSA should not be larger than 12 λ_0 taking into account the wavelength on air. Several designs have been simulated to obtain the best performance on the $[62 - 86]$ GHz band. To calculate λ_{eff} on the stacked layer substrate, ϵ_{eff} and t_{eff} are also calculated, taking into account both substrates as in Eq. 4.29 and Eq. 4.30 [97] respectively. For the stacking used in this thesis, the resulting $\epsilon_{eff} = 6.58$. If the same antenna is simulated with a substrate of the same width and the equivalent ϵ_r, it does not radiate in any of the bands under study. The simulations are not showed here due to conciseness.

$$\epsilon_{eff} = \epsilon_{r1}\frac{thickness_1 * 4}{total\ thickness} + \epsilon_{r1}\frac{thickness_2 * 3}{total\ thickness} \tag{4.29}$$

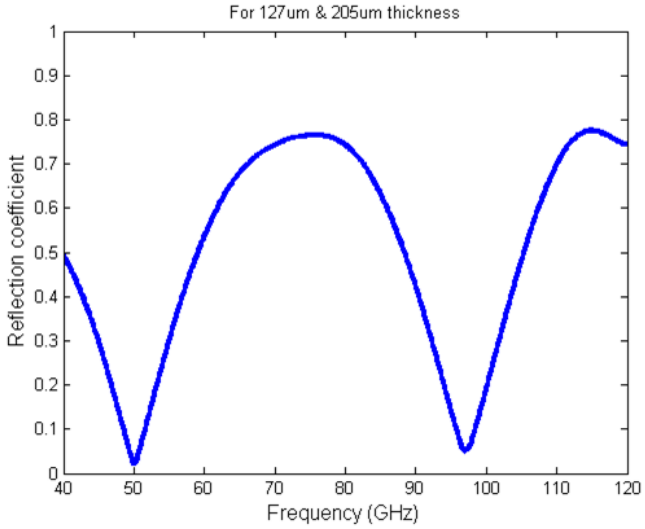

Figure 4.29: Reflection coefficient for the EBG of 7 layers (3 periods)

$$t_{eff} = (\sqrt{\epsilon_r} - 1)t/\lambda_0 \tag{4.30}$$

As the final implementation of the prototypes is based on an homodyne scheme with a schottky detector, for simulation purposes it is used a discrete port to feed the CPS line. The input impedance of the line is designed for 50 Ω over the high permittivity substrate. The manufacturing method employed is micromachinning.

Going further with the design and taking advantage of the isolation and component suppression of the EBG, two TSA antennas are printed on the substrate, one on each side. This way, an array structure can be implemented within the same device and the size of the element would be lower. This configuration is implemented in a linear array, having therefore a $2 \times N$ array device. The behaviour of this structure is studied to compare it with the single element behaviour.

This work is framed in a research stage of 6 months in University of California, San Diego, where the facilities for measurement and manufacturing were available. The expertise of the group from UCSD helped in the development of this concept on TSAs.

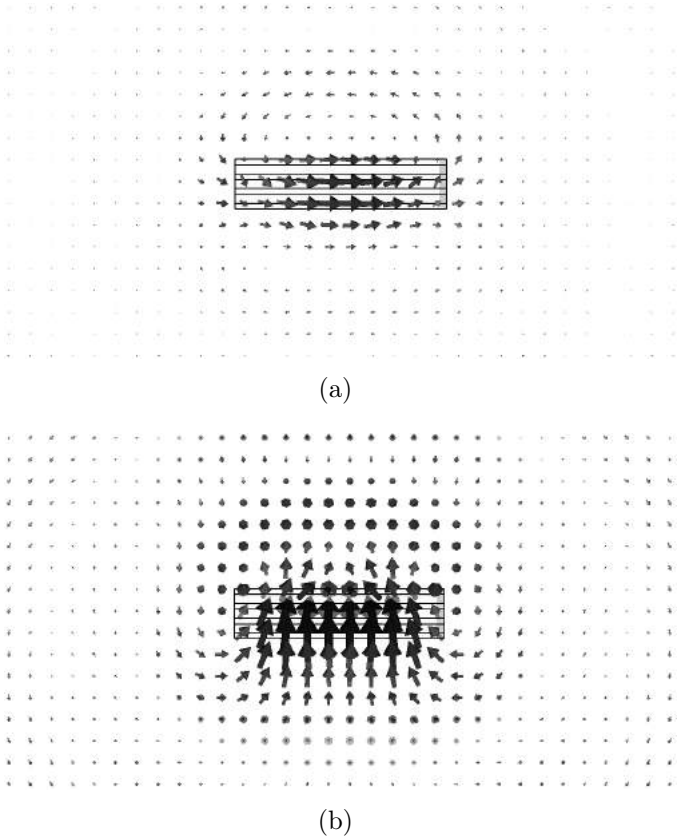

(a)

(b)

Figure 4.30: Fields on the aperture of a LTSA printed over an EBG at 70 GHz (a) E-field (b) H-field.

Single element one-sided

In order to illustrate the performance of the structure, a LTSA printed over several layers of commercial dielectrics in high frequencies, from 50 GHz to 100 GHz, with the materials specified above. The aperture of the LTSA is 0.8 λ_0 at 90 GHz and has a 3.38 λ_0 length. The simulations have been done with CST Microwave studio [81]. The obtained fields in the aperture are shown in Figs. 4.30 and 4.31 where the EBG is supressing the vertical component or not respectively.

With more detail, in Fig. 4.30, the modes propagating in the structure agree with the modes in Section 4.2, where the vertical component must be zero or close to zero on the E-field when the LTSA is radiating with an end-fire configuration. Furthermore, in Fig. 4.31, where the EBG does not have its properties as modes suppresor, a higher order mode is propagating, appreciated on the E-field configuration. The radiation properties of this

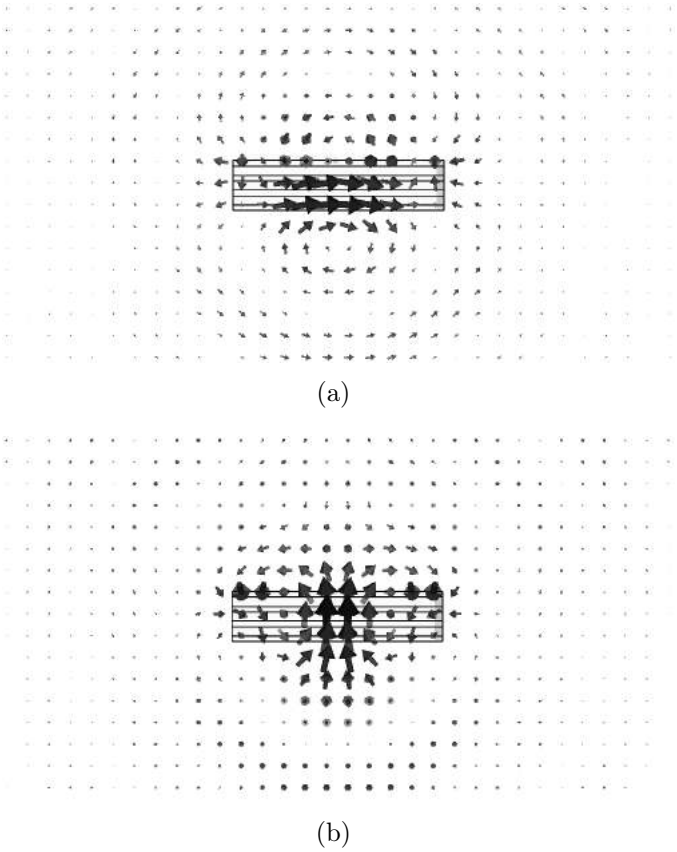

(a)

(b)

Figure 4.31: Fields on the aperture of a LTSA printed over an EBG at 90 GHz (a) E-field (b) H-field.

structure in these two frequencies are shown in Fig. 4.32 together with the simulated structure to serve as a reference and in both frequencies, 70 GHz and 90 GHz. The radiation pattern at 70 GHz is radiating end-fire, with a single main lobe, while at 90 GHz the radiation is not end-fire anymore. The dimensions of the EBG are within limits of the typical design parameters, but not the overall effective thickness of the substrate which is well beyond the limits predicted in [97] for the resulting ϵ_{eff}

The first attempt to implement the described structure is a single antenna over the EBG studied above. Several prototypes have been manufactured with the aim of validating the simulations in both shapes, linear and vivaldi. This element will be the baseline for all other devices composed by more than one antenna, in an array configuration.

The Schottky diode mentioned in previous Section is employed. The feeding region of the antenna must be designed in order to accomodate both the

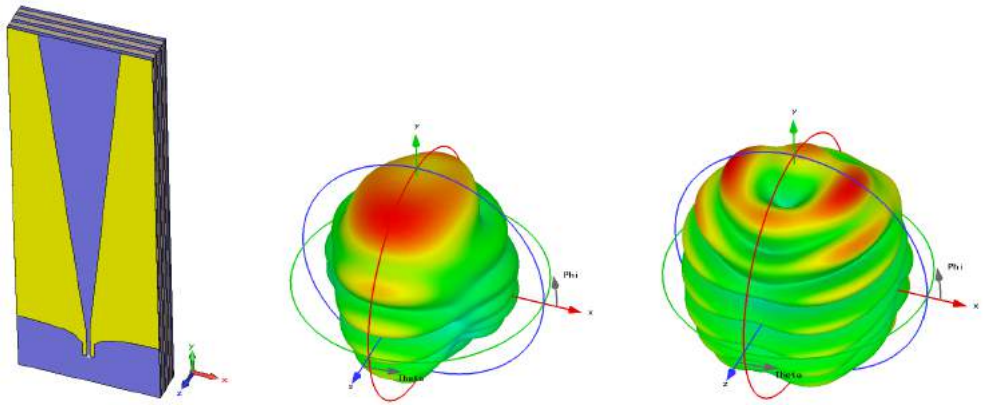

(a) (b) (c)

Figure 4.32: (a) Simulated structure and Far Field at (b) 70 GHz and (c) 90 GHz

dimensions of the diode and the conjugate input impedance to reduce the mismatch as much as possible. The most optimal feeding of the TSA antenna is the CPS line when functioning with a diode of around 50 Ω impedance. The minimum spacing between the lines is fixed by the diode dimensions of 265 μm to be able to bond the terminals to both of the lines. As studied by [121], the minimum gap between the lines, the higher the impedance. There is also a limitation regarding the thickness of the copper lines due to manufacturing purposes, which is 100 μm. With this constraints and having in mind the diode impedance, the resulting CPS line is depicted in Fig. 4.33(a).

As a transition between the TSA antenna and the CPS line, a curve based on a tangential functions is used due to the need of a smooth transiton to both conductors of the antenna. The curve equation is defined in Eq. 4.31, where C and $smooth\_factor$ are constants based on the transition smoothness and $offset$ is related with the antenna total width.

$$Y = C * \arctan\left(\frac{X - offset}{smooth\_factor}\right) - offset \tag{4.31}$$

For the single element, some measurements have been performed to validate simulations. First of all, the change of shape on the antenna, strongly influences the performance of the EBG performance. The end-fire radiation is only achieved at some of the working frequencies of the EBG. The range employed fot the TSA length is between 2 λ_c and 4 λ_c, while the aperture is between 0.7 λ_c and 1.2 λ_c, where $\lambda_c = \frac{c}{90GHz}$.

The simulated input impedance of the antenna in Fig. 4.32(a) is shown

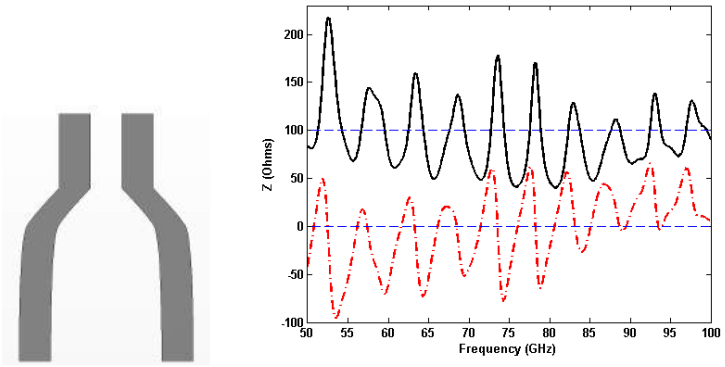

(a) (b)

Figure 4.33: (a) Feeding CPS line transition for TSA antennas and (b) Real (solid) and Imaginary (dashed) part of input impedance

in Fig. 4.33(b) with a discrete port simulating the Schottky diode employed as excitation at the beginning of the CPS line. This antenna is the same as for the fields in Figs. 4.30 and 4.31. The real part of the impedance is oscillating around 100 Ω while the imaginary part is centered in 0 Ω. This is in accordance with the characteristic impedance of travelling wave and ultra wide band antennas [83].

Some examples of the simulated radiation patterns are in Figs. 4.32 for the antenna with aperture of λ_0 and 3.5 λ_0 long, with λ_0@100GHz. Fig. 4.34 shows a picture of one of the manufactured antennas, in this case, a Vivaldi TSA, with an exponential aperture and a reference to compare the size. The two wires connected to each of the arms of the antenna are the contacts for the DC bias of the schottky diode.

Single element double-sided

The next design is composed by two antennas printed on one side of the dielectric EBG structure each. The antennas are excited both with the Schottky diode employed in previous section, and during measurements, only one of them is in receiving configuration, while the other is passive and not biased, having in the terminals of the antenna the equivalent resistance of the diode. It behaves as a resistance, terminating the CPS line of the TSA antenna. The measurement setup is the same as employed in previous Section. The same EBG composite structure has been employed as for the single antenna.

In Fig. 4.35(a) the geometry of a Vivaldi element is shown, together with

Figure 4.34: Manufactured Vivaldi over an EBG at 80 GHz

the radiation pattern obtained at 80 GHz in Fig. 4.35(b). The pattern for the other side is the same, as the structure is symmetrical. There is a small asymmetry on the pattern regarding the Z axis, as even the EBG is acting as a high order mode suppresor, the properties for wave propagation are not the same as for the air.

Linear array

In order to increase the radiated power in the THz range, set as the goal of this thesis, the topology of the same structure is tested in an array configuration. Within this experiment, the antennas are working with an homodyne detection scheme, nevertheless the antenna concept of TSA array with an EBG can be checked due to the reprocity theorem of antennas.

The first configuration developed in an array scheme is the single sided system. For this test also Vivaldi and linear TSAs are employed for simulation and measurement, and several prototypes have been manufactured. The structure can be seen in Fig. 4.36(a), with the three elements, and the EBG substrate in the background. In Fig. 4.36(c) the radiation patterns for two elements, one corner and the central element, of a 1×3 array are presented. The elements of the array are connected (side by side). The radiation for the corner element is deviated towards the direction of the center of the array, happening also in classical array configuration with conventional substrates in this antena, when it is not an infinite array and the mutual coupling is strong [87]. The elements are excited one by one, therefore only one of the antennas is receiving, while the other two are loaded with the lumped port impedance (50 Ω). The simulations are shown at 80 GHz, there is a shift in frequency regarding the single element array, being common for this type of

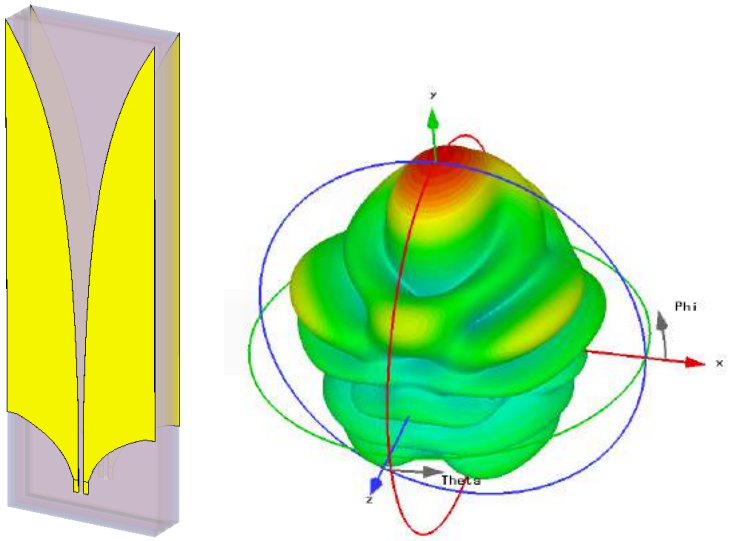

(a) (b)

Figure 4.35: (a) Example of a double Vivaldi antenna over an EBG substrate (b) simulated far field 70 GHz.

compositions [87].

Two pictures of arrays are shown in Fig. 4.37 with a reference for size comparison, for a 5 and 9 elements systems. These systems have not been measured due to time limitations on the stage when this work was scheduled.

Measurements

The measurements on this section intend to validate the EBG substrate designed before. Two antennas have been measured, one single and one double sided, in this way the performance of the EBG substrate can be checked as well as the isolation between the two antennas in the double-sided configuration. The feed for the elements is a GaAs Beam Schottky diode $MA4E2037$, in an homodyne receiving configuration. With this device, it is possible to measure the radiation pattern of the structure, checking therefore the suitability of the EBG to these type of antennas. The diode is polalirzed with 0.6 V, and connected to a lock-in amplifier. The measurement set-up and polarizing circuit scheme for this experiment is illustrated in Fig. 4.38(a), where the lock-in amplifier is connected in parallel to the diode.

The series resistance with the diode is 940 $K\Omega$, while the voltage is variable around 0.6 V to allow a DC polarization voltage on the schottky diode

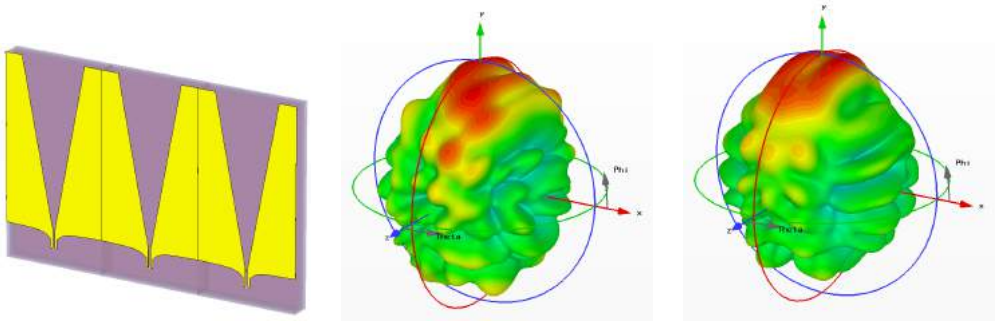

(a) (b) (c)

Figure 4.36: 1×3 array of LTSAs and radiation patterns @80 GHz: (a) structure simulated, (b) corner element and (c) central element.

(a) (b)

Figure 4.37: Manufactured arrays at 80 GHz (a) Vivaldi and (b) LTSA

of 0.3 V. The diode impedance is close to zero according to the element datasheet.

There have been measured two different antennas. The first one isolated, single sided with a width of 3.15 mm and length of 15.10 mm, corresponding with Fig. 4.39(a). The two curves represent the E-plane for two different frequencies 70 GHz and 75 GHz. The difference in the level as well as the noise in the measurement are due to the measurement system setup, in an optical table more suitable for higher frequencies. From the Figure, a broadside radiation, witout deformation of the beam is obtained, as it was the intention to demonstrate according the previous theory.

The second antenna measured is the double sided Vivaldi, with a width

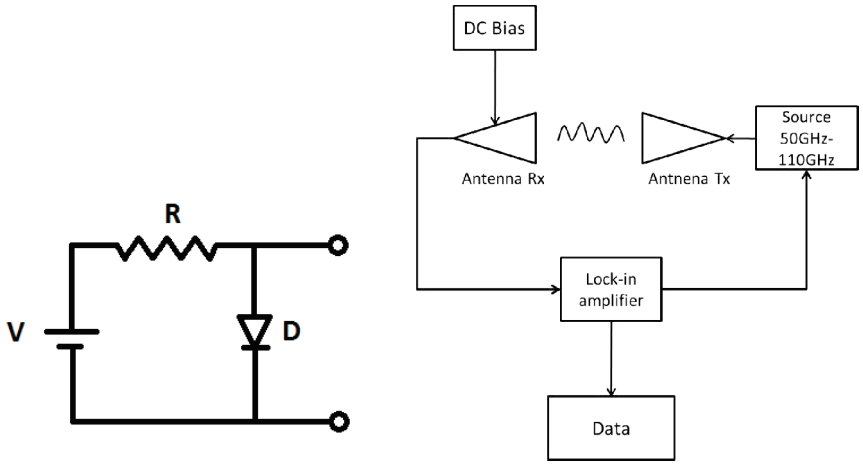

(a) (b)

Figure 4.38: (a) Polarizing cirtuit and (b) set-up for pattern measurement

of 3.92 mm and length of 13.07 mm, corresponding with Fig. 4.39(b). For this case only one measurement on the E-plane at 80 GHz was taken due to time limitation of the anecoic chamber. There is a maximum in the broadside direction, having therefore demonstrated the fundamental mode operation of the TSA again.

4.3.3 Superstrate antenna

The last application presented for the TSA modes theory is the TSA embedded between two identical substrates. From now on, one will be called substrate and the other superstrate. The main idea is to supress the transversal components of the electric field, as in previous examples. With the aid of symmetry, the electric field on both of the substrates is on the same direction with opposite sign, being cancelled on the far field, and therefore allowing end-fire radiation.

The LTSA employed on these simulations is tunned in the Terahertz range, as the main application is to serve as the radiating element for photomixers [79]. Being the central frequency on 1 THz, with $\lambda_0 = 300$ μm on air, the length of the LTSA is 4 λ_0 and the aperture width is 0.64 λ_0. The material employed for the substrate and the superstrate is GaAs ($\epsilon_r \approx 12$) due to the similarities with the photomixers wafers compounds. An example of this structure is plotted in Fig. 4.42.

The fields on the structure in simulation are shown in Fig. 4.40. On

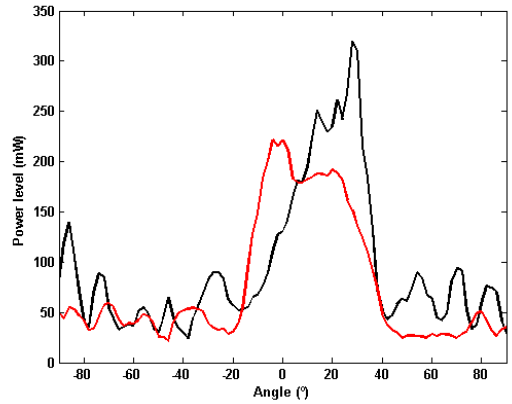

(a)

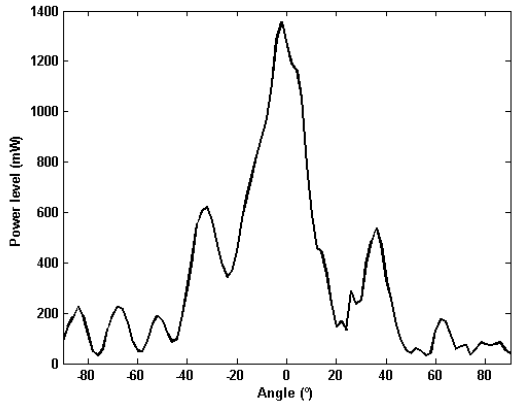

(b)

Figure 4.39: Measurements in E-plane for EBG antennas (a) Single sided at 70 GHz (black) and 75 GHz (red) and (b) Double sided at 80 GHz

Fig. 4.40(a), it is shown the E-field at 1 THz. The horizontal components, responsible for the propper radiation of the LTSA, are sum in phase, as they are completely symmetric, while the vertical (transversal) components are of the same magnitude but in opposite phase, being the modes to be eliminated. The overall contribution in the vertical component is zero, as the structure is completely symmetric. Regarding the H-field, represented on Fig. 4.40(b), the disired effect is the same as in previous applications and agrees well with the theory of previous sections. The vertical component is added in phase while the hortizontal component is in opposite phase and they are mutually cancelled.

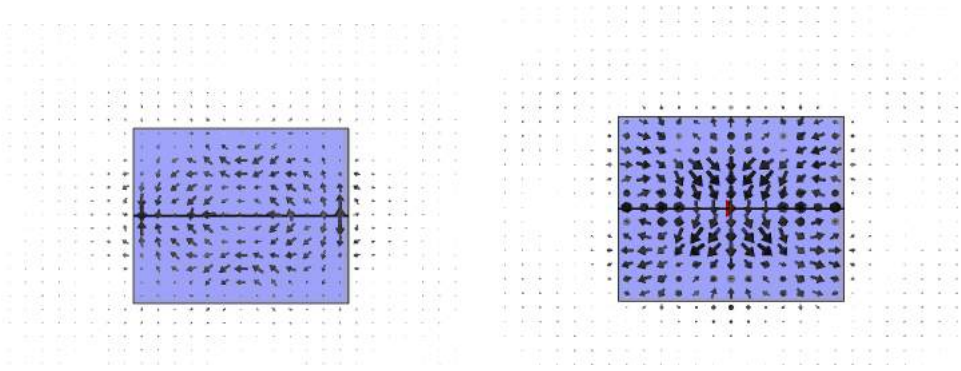

(a) (b)

Figure 4.40: (a) E-field on the antenna aperture at 1 THz (b) H-field on the antenna aperture at 1 THz

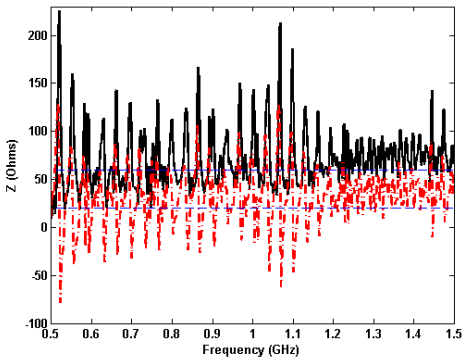

Figure 4.41: Input impedance of an LTSA with superstrate, Real (solid) and Imaginary (dashed) parts.

The theory behind this application is valid when both of the substrates are completely symmetrical to allow the corresponding components to be added and substrated in phase. Regarding the input impedance of the antenna, the simulation is carried out with a discrete port, simulating a diode on the antenna feeding region. The obtained impedance is shown in Fig. 4.41. The real part is centered around 60 Ω while the imaginary part is around 20 Ω. The oscillations are due to the typical impedance of travelling wave antennas, as in previous section [83].

The resulting radtion patterns from this configuration are shown in Fig. 4.42 together with an example of the structure. The patterns are plotted at 1 THz in both $3-D$ and in polar coordinates. The symmetry of the radiation pat-

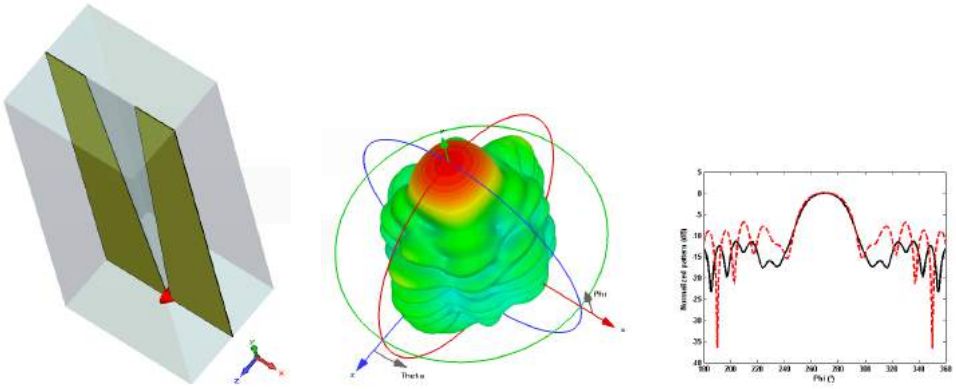

(a) (b) (c)

Figure 4.42: (a) Simulated LTSA with superstrate (b) Radiation pattern (c) normalized pattern on E- and H-plane.

Table 4.3: LTSA with superstrate directivities

Frequency (THz)	Value
0.7	8.10
0.9	7.13
1	7.81
1.1	9.05

tern is achieved, agreeing with the field configuration plotted in Fig. 4.40, maintaining therefore the propperties of a conventional LTSA.

The working frequency range of this antenna is from 0.7 THz to 1.3 THz. A summary with the directivities at different frequencies is in Table 4.3.

4.3.4 Conclusions, future lines and contributions

A theory with a physical meaning of the propagation in a tapered slot antenna has been developed on this chapter. Together with the theory, some applications as proof of concept have been studied, simulated and measured with positive results.

The modal decomposition of the propagating EM fields on the TSA allows the study of the different topologies, and to adjust and design the appropiate substrates and geometries to allow only the modes responsible for the end-fire radiation to propagate in the structure. The fundamental mode of the

structure is an hybrid mode HE_{11}, with two PMC walls and two dielectric-air discontinuities. The main component of the E- and H-fields on the structure are tangential and perperdicular respectively. Knowing the fields propagating in the structure, also the BME coefficients can be computed, including the gaussicity of the beam. This will be a key input for next Chapter analysis.

Some aplications of this theory were developed within the scope of this Thesis: a wedge antenna, an EBG TSA and a substrate-superstrate embedded antena. The wedge antenna is designed to be fed with interdigitated PM over a high-permittivity substrate. The simulations were performed in the THz band, while a prototype was manufactured at 50 GHz, with equivalent substrates and obtaining end-fire radiation.

The second example for this theory is the EBG antenna. The concept is based on the suppression of the perpendicular component of the E-field (the direction where the EBG operates) therefore the second order mode that couples energy and does not have end-fire radiation does not propagate. Added to the single element configuration, a double sided antenna and also arrays have been designed. Only the single and double elements were measured due to time limitations on the time stage (on the scope of UCSD stage in 2010-2011). The results obtained shown a satisfactory operation in the low-THz band.

The thrid case is the superstrate antenna. To continue with the supression of the second order mode for the Electric field, the superstrate aims for cancelling this component present in the structure, having therefore only the fundamental mode for operation, as a proof of concept.

As a straightforward line to continue this research is the implementation of new structures based on the modal theory. As occurs in waveguides, some discontinuities can be designed to prevent propagation of higher order modes and eliminate them. This solution is based on classical mode suppression on dielectric waveguides; the main idea is to etch the dielectric substrate where the antenna is printed, within the radiation slot of the TSA itself. Keeping in mind the final goal of this Thesis, of increasing the total radiated power, arrays with more elements can be implemented as well as optimized. These studies can serve as a first step for new topologies of these types of antennas. It is importat to validate the low-frequency results with prototypes in the THz band.

Also, in some of the examples of the new structures for the TSAs, the QO approximation (BME) of the feed has been computed. This is in line with next Chapter fundamentals. This coefficients will allow the analysis of larger systems that can not be analyzed in a full wave simulation with a

conventional personal computer.

The contributions of the content of this Chapter to international journals, conference papers and research stages are:

- B. Andrés-García, L.E. García-Muñoz, A. Murphy, J. Montero-de Paz, M. Midrio, V. González-Posadas, D. Segovia-Vargas, "New Approach to the Radiation Mechanism of Tapered Slot Antennas", *Submitted for publication.*
- B. Andrés-García, L. E. García-Muñoz I. Cámara, R. Gusten and D. Segovia-Vargas, "Antenna in the Terahertz Band for Radioastronomy applications", *EuCAP (European Conference on Antennas and Propagation)*, Barcelona, Spain, April 2010.
- B. Andrés-García, L.E. García-Muñoz, I. Cámara-Mayorga, D. Segovia-Vargas, and R. Gusten, "Ultrawideband Antenna Excited by a Photomixer in the Low Terahertz Band", *Progress in Electromagnetic Research*, vol. 114, pp. 1-15, 2011.
- Research stage during 6 months in Univeristy of California, San Diego, October 2010-March 2011.

CHAPTER 5

Numerical Methods for Analysis Acceleration

5.1 Introduction

In previous Chapters, several techniques for improving the radiated power in the THz band have been presented. In line with optimization techniques, the current Chapter aims for the optimization of simulation time and resources in THz systems, specially in large arrays.

In the current situation, commercial software is not fully optimized for THz analysis or for example the combination of large and small structures in the same model, that can combine different analysis methods for optimum analysis. As far as the author's knowledge, numerical methods that also take into account different types of mutual coupling between elements in large structures have not been developed for the examples presented on this thesis.

Two main lines have been developed:

- Quasioptical analysis (QO)
- Method of moments (MoM)

The main motivation for both of them is to optimize the computation time and resources that would be needed to analyze THz systems.

The Chapter is organized also in two main Sections, depending on the numerical technique employed. In Section 5.2 QO techniques are presented,

with the developing of a software to analyze without huge computer resources relatively electrically big structures, like reflectors, in presence of small feeds.

In the second part of the Chapter, two techniques are developed based on the Method of Moments (MoM) with the aim of reducing the usual time consumming of full wave analysis as well as to be able to carry out simulations with limited computational resources.

First of all, a fast iterative technique is presented for the analysis of large reflectors through the combination of MoM with Physical Optics (PO) on Section 5.3. The iteration is based on a Krylov approach imposing orthogonality on each step, together with the use of Macro Basis Functions (MBF) on the feed region. The complexity of the problem is reduced by a N_f/P factor with N_f the number of unknowns in the reflector and P the number of MBFs, with respect to previous approaches.

On Section 5.4, related with mutual coupling of antenna elements, a method based on the study of the impedance matrix between MBF functions is developed. By the modification of certain matrix elements and with the aid of previous simulations, it is possible to have an estimation of the mutual coupling between single devices as well as to create a model for it without the need of the simulation of the entire array. This method will be applied to regular arrays as well as to sparse arrays, where the mutual impedance is not easily computed by an analytical expression.

5.2 Quasioptical analysis

The aim of the work described on this section is the study of optical systems in an efficient manner, and take advantage of the QO techniques developed and summarized in [122] among previous authors. One of the best definitions of quasi-optics belongs to the propagation of a beam of light, collimated, but with relatively small dimensions in comparison with its wavelength. This definition can be applied either to microwave beams or to submillimeter frequencies. Quasioptical techniques belong to the region where microwave and optics can not be applied anymore. It includes the situation where a beam is moderately big in wavelengths. This approximation allows the application of Beam Mode Expansion (BME) and gaussian beam propagation [122]. It includes the diffraction limits and the advantage of using QO techniques lies in the approximation between BME of gaussian beams.

5.2.1 Gaussian Beam Propagation

There are two approximations in QO theory: Fundamental Mode propagation and Higer Order Modes propagation, what is called BME. The wave equation comes from the paraxial wave equation in cylindrical coordinates with axial symmetry, given by Eq. 5.1. The solutions of this equation are the gaussian propagation modes.

$$\frac{\partial^2 u}{\partial r^2} + \frac{\partial^2 u}{\partial r^2} + \frac{1}{r}\frac{\partial u}{\partial r} - 2jk\frac{\partial u}{\partial z} = 0 \tag{5.1}$$

With the fist solutions of Eq. 5.1, the fundamental parameters of a gaussian beam are obtained, assuming Z as the propagation axis, like R, curvature radius of the beam; ω, the beam radius, defined as the value of the radius when the field drops $1/e$ with respect to its value in the axis. Another definition is ω_0, known as the beam waist, is the radius of the beam at $Z = 0$ and is the minimum radius that the beam could have, where R is infinite, characteristic of a planar wavefront. These parameters charazterize a gaussian beam, therefore, for a BME, these parameters will be the key factors for the fundamental mode.

When a beam can not be characterized by the fundamental mode only, due to its complexity and a low energy coupled to this mode, it is neccesary to obtain the parameters for the higher order modes. They contain variations that can be sum to the fundamental mode, to characterize a certain beam that has more power variations than in the propagation axis [122].

Once the parameters for a BME are obtained, the transformation of beams through optical elements is straight forward. This is the main advantage of having an electromagnetic beam characterized by gaussian coefficients.

For this Thesis, the simulation software has been implemented with Matlab [127], including the main transformation elements such as lenses: thick and thin; and mirrors: planar, conical, elliptical, parabolic and hyperbolical. For the simulation, besides the parameters of the BME, some other effects have been taken into account, like losses on the system due to truncation and dispersion, cross-polarization and dielectric absortion [122].

5.2.2 Validation and test results

Three different subsystems have been employed for the validation of the program before using it for design purposes on this thesis: Crawford Hill telescope [128], Yebes 40 m radiotelescope [129] and a confocal ellipsoid reflector

system [130].

Crawford Hill Telescope

The Crawford Hill Telescope is described in [128], including a schematic of the quasioptical system on it. The focal distances can be calculated from the provided data: curvature and beam radius for each gaussian beam. The simulation frequency is 120 GHz and it is used both the mirror based aproximation and the thin lenses equivalent.

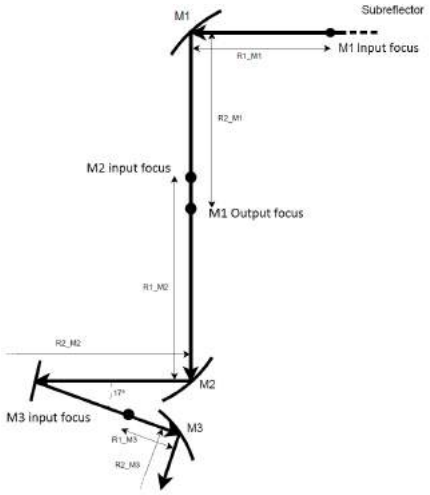

Figure 5.1: Crawford Hill Telescope beam path.

In Fig. 5.1 it is presented the beam path that has been simulated. All the caculations to obtain both the focal distances in the case of lenses and the focus position in the case of mirrors are done employing Eqs. 5.2-5.3 [122]. The system is in reception configuration. From the values of curvature radius and beam radius in the subreflector ($R = 5359\ mm$ and $\omega = 372.6\ mm$), it is possible to calculate the position and the input beam waist also with Eqs. 5.2-5.3

$$z = \frac{R}{1 + \left(\frac{\lambda R}{\pi \omega^2}\right)^2} \tag{5.2}$$

$$\omega_0 = \frac{\omega}{\sqrt{1 + \left(\frac{\pi \omega^2}{\lambda R}\right)^2}} \tag{5.3}$$

Also, the focal distance of each of the mirrors can be calculated with $\frac{1}{f_{ellipsoid}} = \frac{1}{R_1} + \frac{1}{R_2}$ knowing the input and output curvature radius of each of

Mirror	Input focus	Output focus	Focal Distance (f)
M1	[0 0 0]	[-1326.1 0 -2312.5]	842.7932
M2	[-1326.1 0 -2160.9]	[-22069 0 -3715]	1445.8
M3	[-1910.3 0 -4002.3]	[-1621.2 0 -4908.1]	319.7881

Table 5.1: Values of the focus and focal disitances of the elliptical mirrors, in mm.

the beams [128]. It can be assumed that the input focus of the mirror is on the same position as the corresponding beam waist, and knowing the intersection point of each beam with its mirror (Fig. 5.1), R_1 is the distance between the input focus and the intersection point with the mirror. Therefore, from the previous equation, R_2 can be obtained. Once these data are known and the direction of the output beam also, to compute the position of the output focus is straightforward.

This method can be applied to each elliptical mirror on the system, to compute its focal points and distance. In Table 5.1 are shown the values of the parameters that define each of the mirrors. These data have been computed placing the M1 focus on the origin, asuming that the beam propagation direction comes from the subreflector and is $-\hat{x}$.

With the aim of validating the developed software, the results obtained with it and the errors with respect to reference [128] are shown in Table 5.2. The maximum error is 0.146%, in the M2 R_{out}. Taking into account also all the other values and for a quick system analysis, as is the intention of this software, these are satisfactory results. Regarding the simulation with lenses, the mirrors M1, M2 and M3 are replaced by thin lenses with a focal distance the same as the corresponding mirror. The simulation results show a maximum error between 0.146% and 0.157%, not being a significatively high.

The simulated diagram is shown in Fig. 5.2, obtained with the developed software.

Yebes 40 m Radiotelescope

The second system to analyze in order to validate the software is the Yebes 40 m radiotelescope, that belongs to the Spanish Astronomical National Observatory. This telescope is fully described in [129]. This system includes all the types of mirrors that have been implemented on this application, and also a thick biconvex lens. This component hetereogenity allows, by simula-

Measurement	Table I [128]	Simulation	Difference	Error (%)
M1: ω	$92,9$	$92,9503$	$0,050$	$0,054$
M1: R_{in}	$1346,3$	$1346,4834$	$0,183$	$0,013$
M1: R_{out}	$2253,5$	$2252,986$	$0,514$	$0,023$
M2: ω	$68,1$	$68,1538$	$0,053$	$0,079$
M2: R_{in}	$1683,8$	$1683,4209$	$0,379$	$0,022$
M2: R_{out}	$10227,8$	$10242,7417$	$14,94$	$0,146$
M3: ω	$59,6$	$59,652$	$0,052$	$0,087$
M3: R_{in}	36688	$36689,0341$	$1,034$	$0,003$
M3: R_{out}	$322,6$	$322,5999$	10^{-6}	$31 \cdot 10^{-6}$

Table 5.2: Comparison between measurements and the simulation data with reflectors. Data in millimiters.

tion of a single system, the computation of matrix transformation and all the parameters of each of the elements.

The frequency band employed is from 92 GHz to 120 GHz. From the design data in the reference, all the input parameters for the software can be computed. The measurements taken to compare the real and simulated system are the following: one of the most important variable that should be taken into account is that the beam radius in the subreflector should be the same for all the frequency bands, with the aim to preserve as a criteria design a drop of power of 12 dB on the edge. On the other hand, as the telescope is in Cassegrain configuration, it is taken, as a second measurement, the beam waist on the Cassegrain focus, as well as the position displacement of the waist with respect to this focus. A sketch of the system is depicted in Fig. 5.3, and a more detailed diagram on Fig. 5.4.

Source

beam waist: $3,3689$ mm.
beam waist position: [0 0 0] mm.
direction: [0 0 1].

Biconvex Lens

position: [0 0 $66,2363$].
thickness: 0 mm;
radius: $31,505$ mm.
$R_1 : -\infty$.
$R_2 : 47,3$ mm.
$n = 2$.

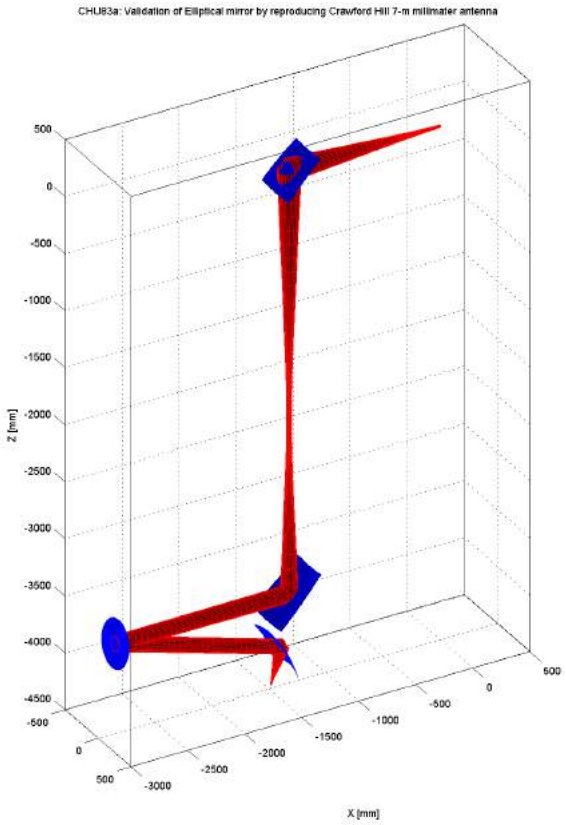

Figure 5.2: Crawford Hill Telescope simulated system

Elliptical mirror

input focus: [0 0 172, 4656] mm.
output focus: [0 1010 624, 1363] mm.
focal distance: 312, 1 mm.
radius: 120 mm.

Planar mirror 1

position: [0 1352, 9 624, 1363] mm.
normal direction: [0, 70711 $-$ 0, 70711 0].
radius: 212, 6694 mm.

Planar mirror 2

position: [790 1352, 9 624, 1363] mm.
normal direction: [−0, 70711 − 0, 66446 0, 24184].
radius: 296, 3131 mm.

Planar mirror 3
position: [790 − 1928, 6 1818, 5] mm.
normal direction: [−0, 70711 0, 66446 − 0, 24184].
radius: 662, 9126 mm.

Planar mirror 4
position: [−1185 − 1928, 6 1818, 5] mm.
normal direction: [0, 70711 0 0, 70711].
radius: 662, 9126 mm.

Subreflector
input focus: [−1185 − 1928, 6 − 4781, 5] mm.
output focus: [−1185 − 1928, 6 21818, 5] mm.
focal distance: −1263, 9213 mm.
radius: 1640 mm.

Main Reflector
focus: [−1185 − 1928, 6 22340] mm.
axis direction: [0 0 1]
focal distance: 15000 mm.
radius: 20000 mm.

Measurement	Reference	Simulation	Difference	Error (%)
Beam radius in subreflector edge	1395	1396, 8576	1, 858	0, 1332
Beam radius in waist	17, 7	17, 7154	$15, 4 \cdot 10^{-3}$	0, 087
Displacement of the waist of the Cassegrain focus	4, 3	4, 7746	$474, 6 \cdot 10^{-3}$	11, 04

Table 5.3: Comparison between the measurements on reference [129] and the simulation data. Data in millimeters.

The results are on Table 5.3. For the two first measurements, the error is on the same order of magnitude as for the system on Section 5.2.2. Nevertheless, for the last measurement, the error is 11.04%. This error can be acceptable or not, depending on the sensitivity of the simulated system and the approximations and assumptions made. For the approximations in this

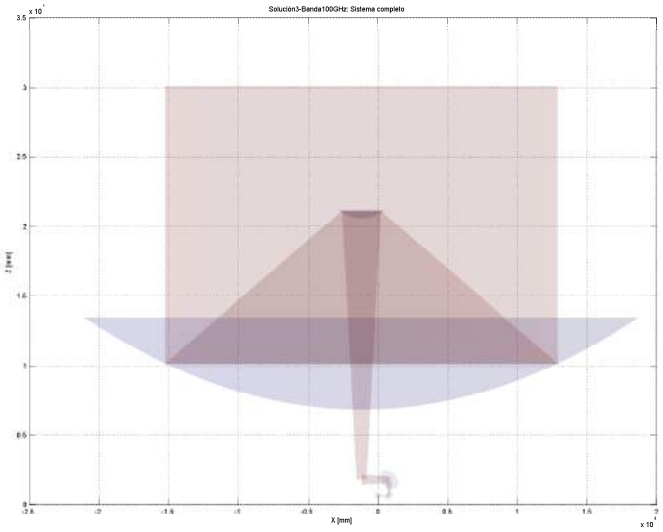

Figure 5.3: Cassegrain System of the Yebes 40 m telescope.

Thesis, and the applications to the THz regime, this error is comparable with other assumptions.

On the other hand, in the reference it is included the far field radiation diagram for the working band in the simulations on this dissertation. This allows the comparison of another feature of the software. From the employed feed horn, the beam radius at the waist is $\omega(0) = 3,3689\ mm$, the displacement of the beam waist inside the horn $z_{offset} = 7,4363\ mm$ and the aperture radius $a = 6,17\ mm$. Despite the BME coefficients are unknown, they can be computed with the available data and [131] as well as the beam radius at the horn aperture $\omega(z_{offset}) = 3,9704\ mm$. The relation between the horn aperture radius and the beam radius on it is $a/z_{offset} = 0,6435$. This value maximizes the power contained in the fundamental mode of the BME ($97,2\%$) and allows to apply the coefficients in 5.4 [131].

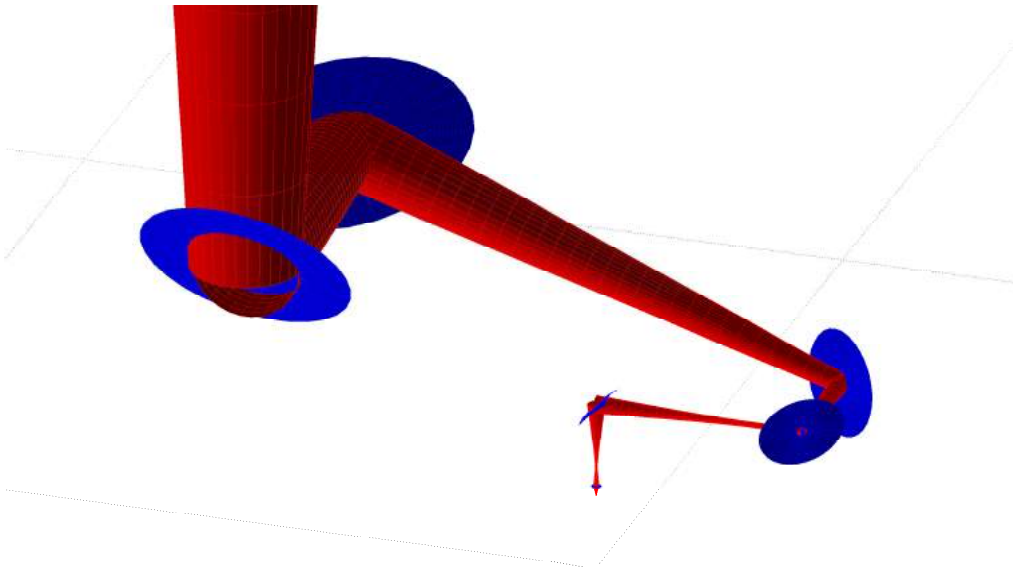

Figure 5.4: Detail of the manufactured system in the receptros cabinet for the high band.

$$coefficients = \begin{bmatrix} 1,12972 \\ -0,00008 \\ -0,13757 \\ -0,04923 \\ 0,02228 \\ 0,03887 \\ 0,02276 \\ 0,00014 \\ -0,01437 \\ -0,01742 \\ -0,01209 \end{bmatrix}^T .$$

If the transversal cuts are compared, in Fig. 5.5 it can be observed the similarity of both of them. The sidelobe is three orders of magnitude below the main lobe. Measured in terms of power, is a drop of at least 60 dB. Also, the first null is in a transversal distance of 10^6 mm. In the obtained figure, this null is at aproximately 10^{-4} rad, if it is considered that in simulation the measurement of the radiation diagram is at 10^{10} mm, this angle corresponds with the same transversal distance of the reference.

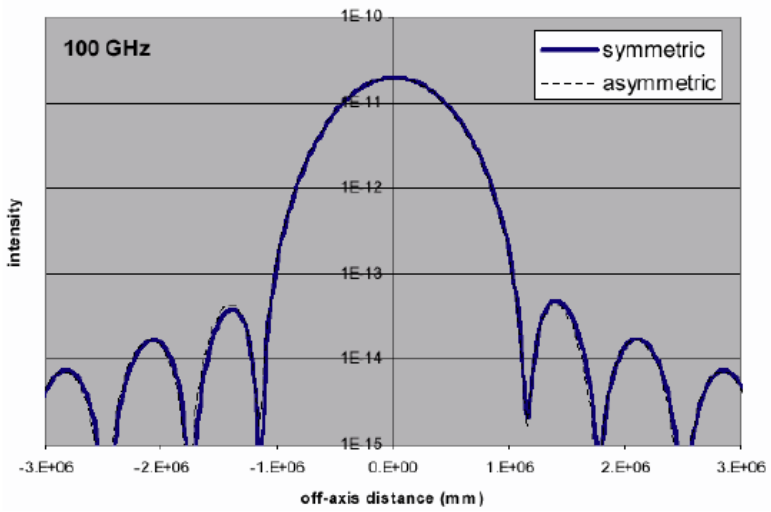

(a)

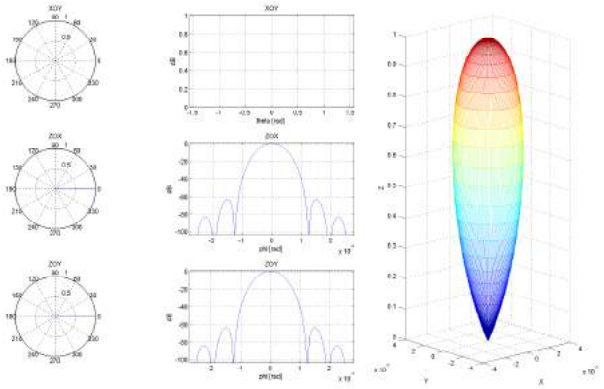

(b)

Figure 5.5: Radiation diagram of from the CAY 40 m telescope (a) in the reference [129] and (b) simulated.

Confocal Ellipsoid Reflector System

The simulation of this system is a step forward on the frequency band. Both of the previous analysis are designed to operate at 100 GHz and 120 GHz, while the current one will simulate the system on the THz band. The working central frequency is 670 GHz, so $\lambda_0 = 0,4477\ mm$.

The work has been developed in two steps: first of all, the system described in [130] with parabolic mirrors is simulated. The objective is to confirm that when a collimated beam is applied to a mirror of this type, in a parallel

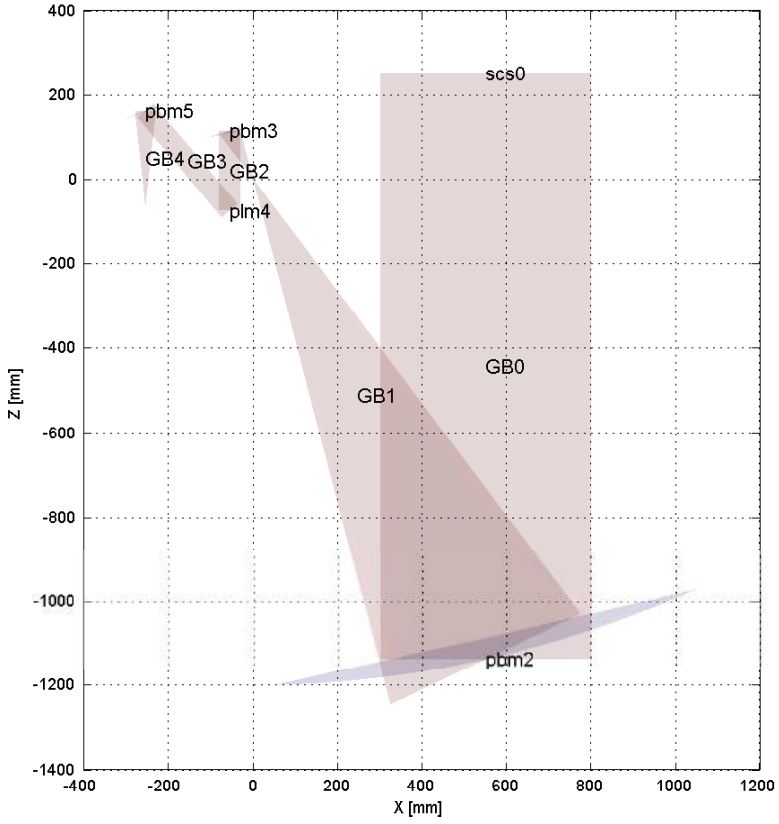

Figure 5.6: System with the parabolic primary reflector.

direction to the reflector axis, the output beam waist is on the focus of the imaginary parabola that conforms the mirror.

In Fig. 5.6 is shown the cut in the XZ plane of the simulation of the first of the sytems in the reference. This system is simulated in reception configuration, and it is composed of the following elements, derived from the data in the reference.

Source

beam radius on the waist: 250 mm.
waist position: [500 0 250] mm.
direction: [0 0 -1].

Primary reflector

focus: [0 0 0]mm.

axis direction: [0 0 1]
focal distance: $1263,3\ mm.$
radius: $500\ mm.$

Subreflector
focus: [0 0 0] $mm.$
axis direction: [0 0 -1]
focal distance: $126,3\ mm.$
radius: $50\ mm.$

Planar mirror
position: $[-55,1\ 0\ -76,4]\ mm.$
normal direction: $[-0,342\ 0\ 0,9397]$.
radius: $50\ mm.$

Feed mirror
focus: $[-254,3\ 0\ -62,3]\ mm.$
axis direction: $[0,64271\ 0\ -0,76611]$
focal distance: $223,4\ mm.$
radius: $50\ mm.$

In this case, the accuracy of the system will be given by the distance of the waist position of the beams, named in Fig. 5.6 as $GB1$ and $GB4$, to the focus of reflector parabola that generates them.

Beam	Waist position	Waist radius
$GB1$	$[-4,48 \cdot 10^{-4}\ 0\ 9,26 \cdot 10^{-4}]$	$0,72021$
$GB4$	$[-254,3\ 0\ -62,7076]$	$1,2732$

Table 5.4: Position of the interest beam waist and the value of the beam radius on it (in mm).

If the data from 5.4 with the primary reflector and feed mirror focus are compared, it is possible to obtain that for the beam $GB1$ there is an error of $0.001\ mm$, or in terms of wavelengths $0.0023\ \lambda_0$; while for $GB2$ the error is $0.4076\ mm$ or $0.9103\ \lambda_0$. This error is bearable or not depending on the analyzed system.

The second step is to replace the main parabolic reflector with an elliptic mirror that allows measurements at $25\ m$ of it. Under this assumption, the mirror should be designed to place the reflected beam waist in the same position of the first case, not having therefore any other change in the system.

Primary Reflector

input focus: [550 0 23863] mm.
output focus: [0 0 0] mm.
focal distance: $1202,5$ mm.
radius: 500 mm.

The reference system [130], is employed to measure the displacement of the output beam waist position from the primary reflector when the source is at $12,5$ cm from it. With a source that generates a beam radius on the waist of 4.477 mm, the waist positions can be obtained for several distances, detailed in Table 5.5.

Source at 25 m	Source at $12,5$ m	Difference
$[9.24 \cdot 10^{-4}\ 0\ -1,91 \cdot 10^{-3}]$	$[-26,2613\ 0\ 60,5042]$	$68,83$

Table 5.5: Position of the beam waist for the measurements at $12,5$ mm and 25 mm, in mm.

A displacement of the output beam waist position of $68,83$ mm has been obtained, in contrast with the 65 mm on the reference. This measurement assumes an error of 3.83 mm (8.5537 λ_0), giving a relative error of $5,8923\%$ from the value of reference.

5.3 Iterative MoM-PO Method

An iterative method based on Method of Moments (MoM) and Physical Optics (PO) has been developed [132, 133, 134, 135]. The direct MoM approach is often too limited in terms of unknowns of the impedance matrix to solve practical antenna problems. For relatively complex structures that requires a lot of unknowns and discretization it may not be possible to simulate it in personal computers and the need of super-computation machines raises.

When analyzing large structures, such as reflectors or analysis of finite ground planes, the number of unknowns in MoM becomes unpractically large, leading to unaffordable computational resources and time in many situations. The use of approximations such as PO, allows the reduction of the complexity in the system by analyzing in an efficient way the electromagnetic fields scattered by the mentioned surfaces. This method combined with more accurate methods such as MoM, allows to increase the efficiency of the computation.

Among the solutions to this problem, the Macro Basis Functions (MBF) approach has progressed substantially over the last decade [136, 137].

Several authors have already reported important progress in hybrid methods, especially in the combination of MoM and PO such as [132, 133, 134, 135]. In this work, the introduction of the MBF/Krylov approach imposing orthogonality on each step of the iteration and over each subdomain provides a new way of developing these kind of methods.

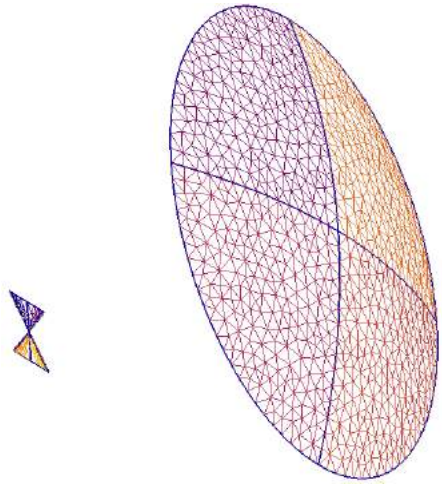

Figure 5.7: Analyzed system. Bowtie in front of a parabola of diameter 5 λ_0 and $f/D = 0.75$ with the mesh employed.

In a first instance, with the full MoM formulation, two subdomains are defined, by the use of an iterative approach based on Macro Basis Functions (MBFs) and Krylov Subspaces [136, 137, 138] that are obtained in a multiple-scattering fashion. The orthogonality between residues and the solution space is imposed at every iteration step on both subdomains (here, feed and reflector) thus leading to convergence in a few iterations. This allows the division of a big problem (feed+reflector) into two smaller problems, saving the computational resources of a full MoM analysis as explained in the introduction. In a second step, the analysis of the slave subdomain (reflector) is carried out by PO, allowing the reduction of the complexity for this subdomain.

In this work, the iteration method based on MBFs/Krylov subspaces is validated, with the analysis with MoM in both subdomains (feeding and reflector); this is the called MoM-MoM solution (Section 5.3.1). Then, once the method is validated, the solution for the fields on the reflector is obtained by the use of a PO approach, based on Rao-Wilton-Glisson (RWG) [140] basis functions; this solution is the called MoM-PO solution (Section 5.3.2).

5.3.1 Definition of the MBFs and full MoM formulation

In this Section the author analyze an antenna as a feed for a reflector and the reflector itself. As an example, one of the analyzed systems is shown in Fig. 5.7, as well as the mesh used for the simulations. The system is divided into two subdomains, where the set of MBFs is defined in a multiple-scattering fashion on each iteration.

The system of equations can be summarized according to Eq. 5.4 where Q_1 and Q_2 are the set of MBFs on the first and second subdomains, feed and reflector respectively, and Z_{ij} is the corresponding MoM sub-block [138]. For the case of a reflector, since the excitation vector must be zero, the system can be reduced to one equation, allowing the iteration procedure. Upon each iteration, orthogonality is imposed between MBFs on both domains using a QR factorization.

$$\begin{bmatrix} Q_1^H Z_{11} Q_1 & Q_1^H Z_{21} Q_2 \\ Q_2^H Z_{12} Q_1 & Q_2^H Z_{22} Q_2 \end{bmatrix} \begin{bmatrix} y_1 \\ y_2 \end{bmatrix} = \begin{bmatrix} Q_1^H V_1 \\ Q_2^H V_2 \end{bmatrix} \tag{5.4}$$

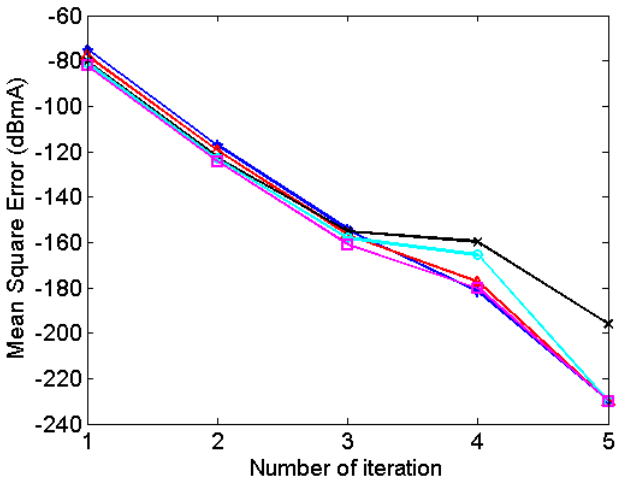

Figure 5.8: MSE for the different ground plane sizes and iterations. $3\lambda_0$ (+), $4\lambda_0$ ($\triangle$), $5\lambda_0$ (x), $6\lambda_0$ (o), $7\lambda_0$ ($\square$).

In previous approaches [132] the complexity of the problem is $O(N_f^2 N_r)$, while the complexity for the equation to solve in the current approximation is reduced to $N_f N_r P$, where N_f is the number of unknowns on the feed, N_r is the number of elements on the reflector and P the number of MBFs. Therefore the complexity is divided by a factor of N_f/P with respect to

previous approaches. The iterations are stopped when the Q_1 matrix loses full rank.

Two examples are analyzed for method validation purposes. A bowtie of $\lambda_0/2 \times \lambda_0/2$ size at 100 GHz has been employed as a feeding structure because it is simple to analyze and needs a reasonable number of unknowns for demonstration purposes. Also, in further Sections, a LTSA will be employed for results verification. First of all, a near-field analysis is carried out, with the simulation of the bowtie over a finite ground plane. The second example is the case of a far field analysis, with the study of the bowtie and a parabolic reflector. All these studies are compared in terms of input impedance of the bowtie (feed) and current on each RWG [140] basis function. The exact solution is computed by Gaussian elimination in the very large original MoM system of equations.

For the first example the bowtie is analyzed in front of the ground plane. The size of the ground plane ranges from 3 λ_0 to 7 λ_0 in order to show the convergence for different cases and it is placed at $\lambda_0/4$ from the bowtie. The Mean Square Error (MSE) computed as Eq. 5.5 where BF is the number of basis functions on the second subdomain, is shown Fig. 5.8 for the different ground plane sizes and for each iteration. In this figure it can be seen that the convergence within an error of -240 dB has been reached after the 5^{th} iteration as compared to the solution obtained with Gaussian elimination; this error can be considered as the machine rounding error. There is almost no influence on the convergence of the characteristics of the analyzed geometry. Regarding the radiation patterns, for this case, the error also remains below -200 dB.

$$MSE = 10log_{10}\left(\left(\sum |I_{exact} - I_{iteration}|^2\right)/BF\right) \tag{5.5}$$

In the case of the far-field analysis, the same bowtie is studied in front of a parabolic mirror. The diameter of the mirror is 7 λ_0 and f/D is set to 0.75, with the feed on the focal point, thus the mirror is placed in the far field of the antenna. The exact currents also converge to the exact solution within five iterations, giving errors below -240 dB, as in the previous case. The radiation patterns in E- and H-plane are shown in Fig. 5.9, together with the error for the exact solution. Both errors remain below -150 dB under the main lobe level, as the method has converged to the exact solution. With these two examples it has been demonstrated that it is thanks to the imposition of orthogonality between residues and the solution space on each step in a few iterations. However, the use of the MoM-MoM technique implies that the big matrices belonging to the second subdomain (reflector) should

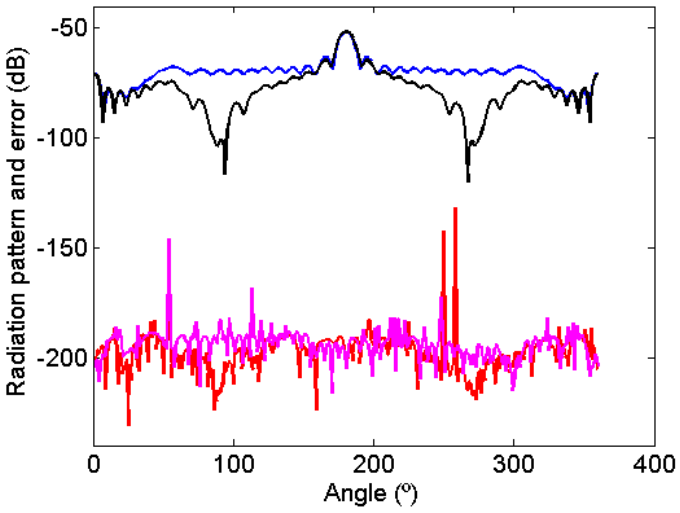

Figure 5.9: Radiation patterns for the MoM-MoM solution of a bowtie and a parabolic reflector of 7 λ_0 and f/D of 0.75. E-plane radiation pattern (blue) and error (red) and H-plane radiation pattern (black) and error (pink).

be computed, which is not affordable in many situations.

5.3.2 Analysis of the reflector with PO

Now that the iteration method has been validated, the analysis of the reflector is carried out with a PO approach. The currents are obtained on each basis function and are employed in the formation of the corresponding subspace (MoM-PO solution). The corresponding MBF for each iteration is computed with the $\vec{H}$ field incident on each basis function on the parabola as in Eq. 5.6, where the indices j and i refer to the basis functions over the feed and over the reflector, that is the contribution of the feed and the successive reflections for both structures. The matrix equation for this system is solved with a sparse LU factorization [127] of complexity $O(N_f)$ hence giving the MBF for each iteration.

$$\sum_i x_i \int \vec{J}_i \vec{J}_j dS = 2 \int \left(\hat{n} \times \vec{H_{inc}}\right) \vec{J}_j dS, \forall j \tag{5.6}$$

For the validation of the method, also the near field and the far field analysis are carried out over different examples. For all cases, comparisons are carried out with the MoM-MoM solution from the previous section. In

this case, the convergence has been reached in the 6^{th} iteration.

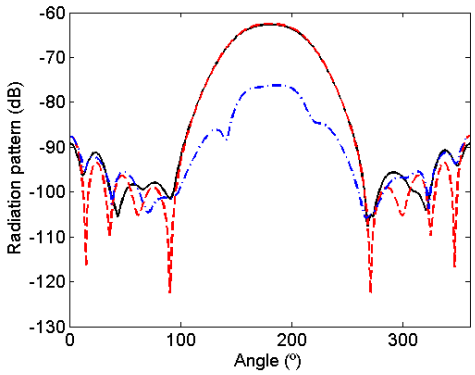

(a)

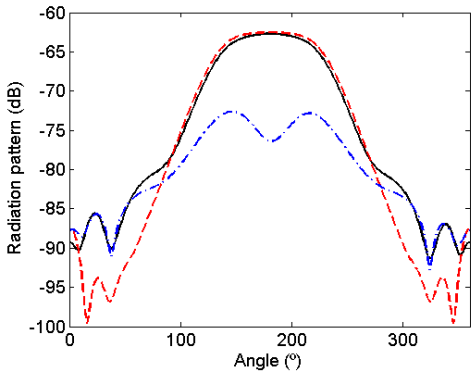

(b)

Figure 5.10: (a) E- and (b) H-plane radiation patterns for the MoM-MoM solution (dashed), MoM-PO solution (solid) and error (-.) for a bowtie over a finite ground plane of 3 λ_0.

The E-plane and H-plane radiation patterns for the bowtie over a finite ground plane are shown in Fig. 5.10(a) and Fig. 5.10(b) respectively. For the case of the E-plane, the method gives a low error in the main beam, while in the H-plane the error is higher due to the highest scattering by the edges for the illumination of the reflector. With this method the input impedance for the bowtie is $282.67 - j13.45\ \Omega$, while with the exact solution equals $280.13 - j151.09\ \Omega$, i.e. the error is below 1%.

Regarding the far field analysis, a bowtie in front of a parabolic mirror is analyzed. The mirror diameter is 7 λ_0 and the f/D ratio is equal to 0.75. The bowtie is in the focus of the parabola. The radiation patterns for both E- and H-plane are shown in Fig. 5.11(a) and Fig. 5.11(b) respectively. In

these figures the radiation patterns for the MoM-MoM solution and for the MoM-PO solution are shown, as well as the error for the MoM-PO solution. This error is below $-30\ dB$ the main lobe level in both planes. The errors are due to the PO approximation, indeed, in the previous Section has been demonstrated that the method converges rapidly to the exact solution of the MoM-MoM problem. The differences in the secondary lobes are due to scattering by the edges, not accounted for with this method. The computing time from the MoM-MoM solution to the MoM-PO is reduced to 1/3. Longer time savings are expected for bigger structures.

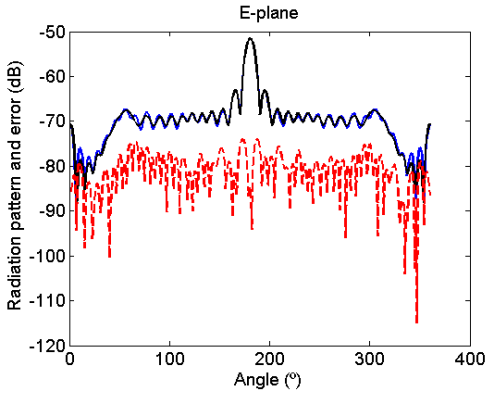

(a)

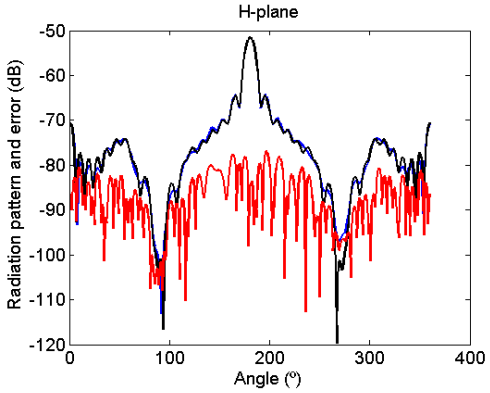

(b)

Figure 5.11: (a) E- and (b) H-plane radiation patterns for a bowtie and a parabolic reflector for MoM+MoM solution (black), MoM+PO solution (blue) and error for MoM+PO solution (red). Reflector $f/D = 0.75$, diameter=7 λ_0.

The error for the near-field analysis is higher than the error for the far-field, due to the PO approximation, according to which the elements should

be placed in the far-field region from each other.

Two more examples have been computed to show the characteristics of the method. The first one is a Linear Tapered Slot Antenna (LTSA) in front of the parabolic mirror. Since the pattern of this antenna is much more directive than the pattern of a bowtie, the convergence for this system is different. Also the diffraction by the edges of the reflector has a lower effect than in the bowtie case due to a different illumination. The error for this case is at least 18 dB below the level of the main lobe, with the maximum error in the side lobe levels.

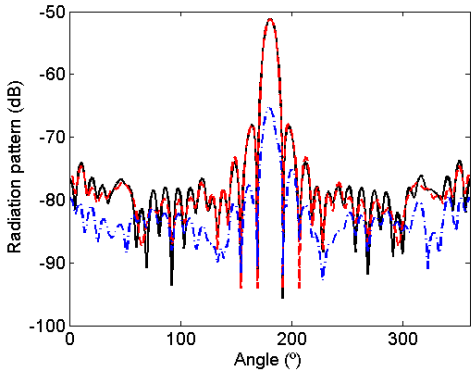

(a)

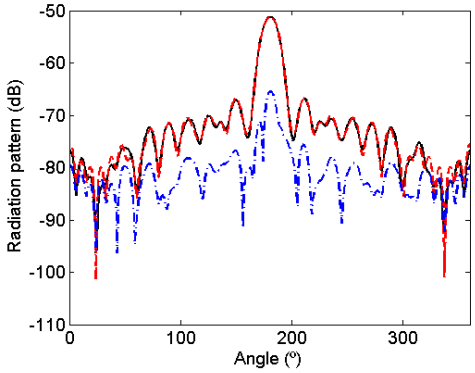

(b)

Figure 5.12: (a) E- and (b) H-plane radiation pattern for a LTSA and a parabolic reflector for MoM+MoM solution (dashed), MoM+PO solution (solid) and error for MoM+PO solution (-.). Reflector $f/D = 0.75$, diameter=7 λ_0.

The second system involves a bowtie and a finite ground plane in the first subdomain and a parabolic reflector in the second subdomain. For this

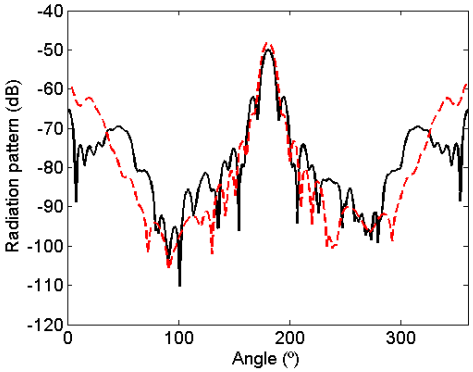

(a)

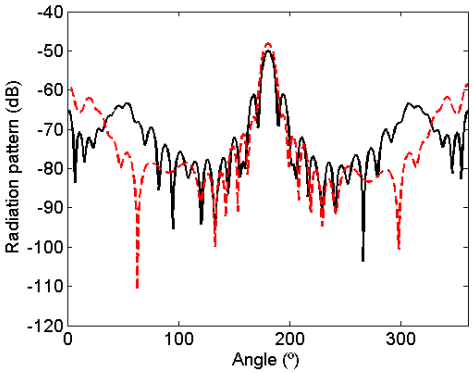

(b)

Figure 5.13: (a) E- and (b) H-plane radiation patterns for a bowtie+finite ground plane and a parabolic reflector. Solution with blockage (solid), without blockage (dashed). Reflector $f/D = 0.75$, diameter=7 λ_0, ground plane size=3 λ_0.

case, the blockage produced by the ground plane in the radiation pattern is studied.

In Fig. 5.13(a) and Fig. 5.13(b) the radiation patterns for this example are shown. In both planes the effect of blockage is appreciated with the difference between the two curves mostly limited to the main lobe.

5.4 MoM Large Array Analysis

One of the main limitations with structures analyzed with MoM is a computational limit: the inversion of the MoM impedances matrix. This task limits

strongly the number of unknowns while analyzing a problem turning in a limitation of the number of elements in an array. Several studies have been carried out to overcome this limitation, some of them with great results

5.4.1 Problem and Scenarios

Electromagnetic problems analyzed with MoM generally have computing limitations due to the computational cost associated with the impedance matrix inversion. This can enormously restrict the number of unknowns to be treated with the MoM. The computational cost ((N^2) being N the number of elements) reduces then the maximum number of elements in the array.

When an electrically large array with a great number of unknowns needs to be analyzed, the inversion of the MoM impedance matrix becomes not a straightforward task in terms of computing resources. Once the MoM impedance matrix is available, the currents for the basis functions and the solution for the electromagnetic problem can be achieved. However, when the electromagnetic problem is very large, either because the array has a great number of elements or because the electromagnetic structure is also large (or both of them), the number of unknowns becomes enormous. Thus, the direct inversion of the impedance matrix and the computational cost associated to it gets more and more unapproachable.

For cases such as this, simplifications in the matrix or mathematical approaches to speed up the method to solve the matrix are always welcome. Some assumptions and simplifications must be made in order to compute the currents with the lowest possible error. Thus, a reduction of this matrix should be made maintaining the accuracy for the computed currents, and therefore the behavior of the array.

The method proposed in this Section consists on a modification in the MoM impedance matrix. Then, the error between the exact currents on the antennas in a very large array and the hypothetical currents on those same antennas, as if they were isolated without any other antenna in the array, is minimized. The idea to pay the attention to the currents rises because, in this way, the entire electromagnetic problem is fully determined and solved. Large electromagnetic problems (arrays in this case) can be analyzed by only calculating the currents on the antennas that we want to obtain the information from. The proposed algorithm aims for optimizing the error between the exact computed currents for the entire array and the currents when only the isolated analysis of the core is carried out. The analysis of much larger problems, that is, a small array embedded on a large array can be analyzed by only computing exactly the currents within the core.

In this Section, three different scenarios will be analyzed: linear array, square (regular array) and random irregular arrays. All the scenarios will be analyzed with MoM by exciting all the elements in the array. Half wavelength dipoles will be used as radiating elements just for comparison with other results and commercial software packages. The grid of the corresponding half-wavelength dipole is shown in Fig. 5.14.

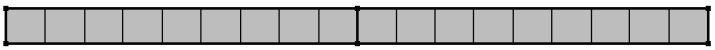

Figure 5.14: Meshed dipole employed in simulations.

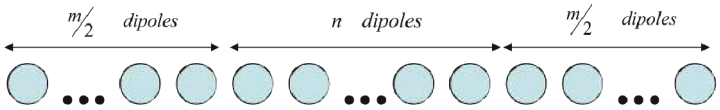

Figure 5.15: Sketch for the linear system.

The n-element array (core) is simulated surrounded by m peripherical elements to obtain the corresponding currents. In the following Subsections the simulation procedure for the three different arrays is explained.

Linear Array

The first situation to be studied is a linear array. For this kind of array the number of elements in the core will be 9. The number of elements surrounding the core, m, will vary between 10 and 92. This means that there will be between 5 to 46 elements at each side of the array core. Initially, the spacing between the radiating elements will be $\lambda/2$. Although different spacings have been analyzed (including lower than $\lambda/2$ where the mutual coupling is stronger), the results are somewhat similar to the $\lambda/2$ spacing, so that case will be chosen as representative of the potentiality of the proposed method. Fig. 5.15 shows the array under study.

Regular Square Array

For the square array case, the number of elements in the core has been set to 9 (in a configuration of 3×3) while m, the number of elements surrounding the core will vary between 16 and 216. This will make possible analyze 5×5 to 15×15 arrays. the schematic of the proposed configuration is shown in Fig. 5.16.

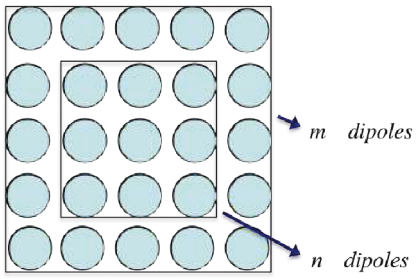

Figure 5.16: Sketch for the regular square system.

Sparse Irregular Array

The third situation concerns the irregular array where all the elements are randomly placed inside two circles with different radius. The first circle detemines the array core and the elements that will be analyzed. The second circle determines the number of elements, m, that have to be analyzed in the peripheric area around the core. All the elements will be placed according to the random Penrose function, as in Fig. 5.17.

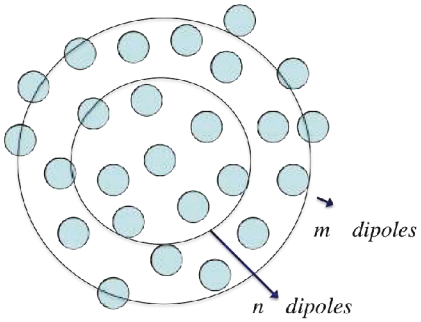

Figure 5.17: Sketch for the Sparse Irregular System.

5.4.2 Algorithm Development

The proposed method is based on a correction in the MoM impedance matrix. This correction yields to a reduction in the error on the currents in the core elements in comparison with the currents in these core elements as if they were isolated. The original matrix for an $n \times n$ array is shown in Eq. 5.7. Each Z_{ij} element is a square $n_{abf} \times n_{abf}$ sub-matrix being n_{abf} the number of RWG [140] functions defined on any antenna.

For each simulation, $n \times n$ is taken as the maximum computational limit.

This means that from the computational point of view, no elements could be added in the array in spite of their actual contribution to the currents in the $n \times n$ array.

The method is based on a modification of the elements in the diagonal of the MoM matrix Eq. 5.7. The new elements in the diagonal are given by a linear combination of the mutual coupling sub-matrices between the i^{th} element and any of the elements in the core.

The prime Z'_{ii} elements are the elements of the diagonal of the modified MoM matrix. The elements Z_{ij} (with j being the core element and varying from 1 to n and i being the elements surrounding the core and varying from $(n+1)$ to m) are the mutual coupling submatrices between the core elements and the outer elements. Then the modified MoM matrix is given as Eqs. 5.8 to 5.9.

$$Z_{isolated} = \begin{bmatrix} Z_{1,1} & Z_{1,2} & \cdots & Z_{1,n-1} & Z_{1,n} \\ Z_{2,1} & Z_{2,2} & \cdots & Z_{2,n-1} & Z_{2,n} \\ \vdots & \vdots & \ddots & \vdots & \\ Z_{m-1,1} & Z_{m-1,2} & \cdots & Z_{m-1,n-1} & Z_{m-1,n} \\ Z_{m,1} & Z_{m,2} & \cdots & Z_{m,n-1} & Z_{m,n} \end{bmatrix} \tag{5.7}$$

$$Z_{optimized} = \begin{bmatrix} Z'_{1,1} & Z_{1,2} & \cdots & Z_{1,(n-1)} & Z_{1,n} \\ Z_{2,1} & Z'_{2,2} & \cdots & Z_{2,(n-1)} & Z_{2,n} \\ \vdots & \vdots & \ddots & \vdots & \\ Z_{(m-1),1} & Z_{(m-1),2} & \cdots & Z'_{(m-1),(n-1)} & Z_{(m-1),n} \\ Z_{m,1} & Z_{m,2} & \cdots & Z_{m,(n-1)} & Z'_{m,n} \end{bmatrix} \tag{5.8}$$

$$\begin{gathered} Z'_{1,1} = Z_{1,1} + \alpha_1 Z_{(n+1),1} + \beta_1 Z_{(n+2),1} + \cdots + \tau_1 Z_{m,1} \\ Z'_{2,2} = Z_{2,2} + \alpha_2 Z_{(n+1),2} + \beta_2 Z_{(n+2),2} + \cdots + \tau_2 Z_{m,2} \\ Z'_{(n-1),(n-1)} = Z_{(n-1),(n-1)} + \alpha_{(n-1)} Z_{(n+1),(n-1)} + \beta_{(n-1)} Z_{(n+2),(n-1)} + \cdots + \tau_{(n-1)} Z_{m,(n-1)} \\ Z'_{n,n} = Z_{n,n} + \alpha_n Z_{(n+1),n} + \beta_n Z_{(n+2),n} + \cdots + \tau_n Z_{m,n} \end{gathered} \tag{5.9}$$

This modification in the diagonal elements allows taking into account in a trusty and exact way the peripheric elements of the core when calculating the currents on those elements. Once this correction has been undertaken, the problem is to find the suitable coefficients (to minimize the error between the exact currents $\alpha_i,\ \beta_i, \cdots,\ \tau_i \quad i \in \{1, \cdots, n\}$ considering all the array elements) and the ones obtained with the modified MoM matrix.

This error will be minimized with an optimization algorithm. The target would be to minimize the error between the calculated current and the current obtained with the exact analysis. This algorithm will be trained with the results of previous simulations. However, the objective of the method is to obtain the results from previous predictions over the array currents, as it will be explained later on. This is the main objective for the proposed method: to be able to predict the currents in a core array embedded in a larger one, and starting from previous studies and without the need of a full analysis.

The method is applied to the three types of proposed arrays: linear, square and irregular sparse, with good results for any kind of arrays.

5.4.3 *One's* correction

A straightforward correction method is to set the coefficients $\alpha_i,\ \beta_i, \cdots,\ \tau_i\ i \in \{1, \cdots, n\}$ to 1 what makes that the corrected sub-matrices in the main diagonal will be the sum of the original element plus the mutual coupling sub-matrices between the core and peripheral elements as in Eq. 5.10.

$$Z'_{ii} = Z_{ii} + Z_{(n+1),i} + Z_{(n+2),i} + \cdots + Z_{m,i};\ 0 < i \leq,\ n < j < m \qquad (5.10)$$

One of the major advantages on making the coefficients equal to unity is that there is not additional computational burden in comparison with the isolated situation, even in terms of memory storage. In this way, very large arrays can easily be analyzed by only computing the mutual coupling (mutual impedance matrix) between each of the elements within the core and the added elements. This can be made relatively easily with closed formulas like applying Hansen method [139] for dipoles or with MoM for any element. The results for any of the proposed topologies are shown in next Sections.

Linear Arrays

Let us consider a 77 element linear array. It will be assumed that the core will consist of 9 elements embedded in the full array. The result when the proposed correction is applied to that array is shown in Fig. 5.18. Two different currents are calculated: the currents in the core in presence of all the elements (I_{exact}, represented as a solid line with $\circ$) and the currents in the core as if they were isolated ($I_{isolated}$, not plotted in the Figure).

The difference between the previous currents denotes the error ($I_{exact} - I_{isolated}$, represented solid with $\square$). When the currents are calculated with the

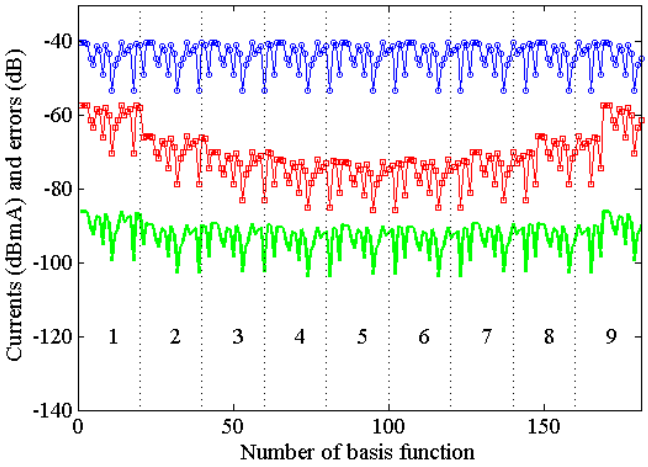

Figure 5.18: Currents for the 9-element core. Exact computed currents in dBA (dark-blue ∘), error in currents for the isolated core analysis in dB $I_{exact} - I_{isolated}$ (red, □) and error in currents computed with the proposed algorithm in dB $I_{exact} - I_{corrected}$.

proposed method, the new set of currents is given by $I_{corrected}$, not represented in the figure, and the error will be given by the difference between the last current and the corrected ones $I_{exact} - I_{corrected}$, represented as a solid line without any mark. In Fig. 5.18, for the isolated case, the average error is 5.87% while for the method with MoM the mean square error is always under 0.3%.

Then, with the correction on the elements of the main diagonal of the MoM matrix, the error is improved more than 20 dB. The more critical elements are the ones at the edge of the core of the array. Fig. 5.18 shows that the error in this element for the isolated analysis is 10 dB larger than in the central elements. This drawback is overcomed with the proposed solution since the error becomes more uniform (especially at the edge of the array) and is reduced in more than 10 dB over the isolated solution.

Regular Square Arrays

The approach when the coefficients are set to 1 has also been applied to a regular topology such as a square array. Fig. 5.19 shows the obtained results. The represented currents follow the same convention as the ones for the linear array. The error when the correction in MoM matrix is applied reduces down to 20 dB in comparison with the isolated case without an extra computational

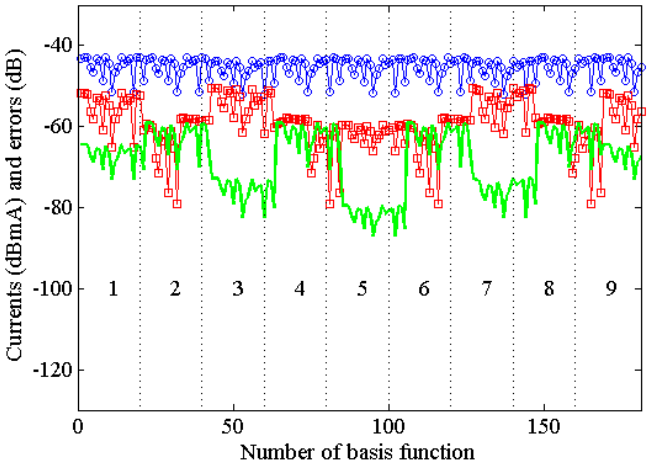

Figure 5.19: Currents for the 9-element core square array. Exact computed currents (dark-blue ○), currents for the isolated core analysis (red □) and currents computed with the proposed algorithm.

cost. For this regular array the error when the currents is obtained only in the isolated core is 24.7% while when the correction is applied this reduces down to 9.2%. Then, the method presents a great versatility and potentiality on analyzing large arrays with a low computational cost and a low error.

Gathering together all these results, it can be concluded that the developed algorithm presents a good performance in evaluating the currents for arrays that can not be simulated with a full-wave method due to computational limitations

Sparse Irregular Arrays

The method is also applied on an irregular array, the third scenario in the simulations. The topology of the array is shown in Fig. 5.20 where the positions are obtained from a penrose function. The results obtained for this system are shown in Fig. 5.21. for this case, there are fifteen elements in the core, inside the first infuence radius, while there are 41 elements in the peripheral area (inside the second influence radius). The error for the coefficients set to one is below the error for the isolated analysis in most of the elements of the array, the overall error for the isolated analysis is $17,5\%$, giving the correction an error of $6,9\%$. For the case of these arrays, with any extra computational load, a low error is achieved without the analysis of the entire array.

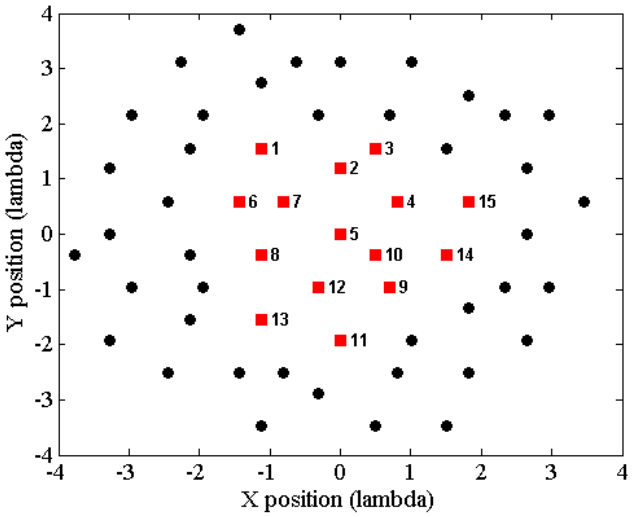

Figure 5.20: Position of the elements for an irregular array. Elements considered in the core (□) and elements in the peripheral area (•)

5.4.4 Optimized Coefficients and Predictions

The coefficients of the corrected matrix can be arbitrarily set in order to improve the error for the currents on each element of the array. Once shown the results of the method for these coefficients set to one, the next objective is to improve this error and also to estimate the currents without the analysis of the entire array or any extra computational load.

The first step on this estimation is the running of an optimization algorithm over the coefficients $\alpha_i,\ \beta_i, \cdots,\ \tau_i\ \ i \in \{1, \cdots, n\}$. With this optimization, the error for the 'corrected' currents given by Eq. 5.11 is minimized with a Particle Swarm Optimization (PSO) algorithm [141].

$$\frac{\sum |I_{exact} - I_{isolated}|^2}{N_{basis}} \tag{5.11}$$

By the use of this optimization algorithm it can be demonstrated that once the optimized coefficients are known for the impedances matrix, it is possible to estimate the currents for bigger arrays with no extra computational load. The data obtained from the optimization procedure will be employed in the estimation of these currents. Several sample arrays will be simulated in order to obtain a behavior law for the correction of the impedances matrix. If the behavior of the correction can be estimated, the analysis of bigger arrays can be carried out without extra computational load.

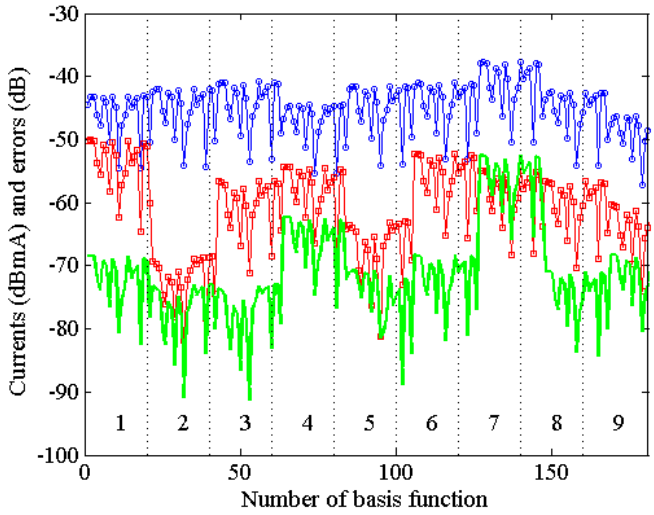

Figure 5.21: Currents for the elements inside the core from first to fifteen. Exact currents on the elements (∘) and errors for: isolated analysis (□) and one's correction (thick).

Estimation procedure

The estimation of the currents is accomplished by the study of the shape of the correction matrix given by Eqs. 5.12- 5.13. This matrix is a diagonal matrix whose elements are $n_{abf} \times n_{abf}$ matrices. The interesting characteristic of these matrices for the current development is that they have the same shape on every simulation, i.e. the same envelope, for arrays with the same topology.

$$Z_{correction} = Z_{optimized} - Z_{isolated} = \begin{bmatrix} \epsilon_1 & 0 & \cdots & 0 & 0 \\ 0 & \epsilon_2 & \cdots & 0 & 0 \\ \vdots & \vdots & \ddots & \vdots & \\ 0 & 0 & \cdots & \epsilon_{n-1} & 0 \\ 0 & 0 & \cdots & 0 & \epsilon_n \end{bmatrix} \tag{5.12}$$

$$\begin{aligned} \epsilon_1 &= \alpha_1 Z_{(n+1),1} + \beta_1 Z_{(n+2),1} + \cdots + \tau_1 Z_{m,1} \\ \epsilon_2 &= \alpha_2 Z_{(n+1),2} + \beta_2 Z_{(n+2),2} + \cdots + \tau_2 Z_{m,2} \\ \epsilon_{(n-1)} &= \alpha_{(n-1)} Z_{(n+1),(n-1)} + \beta_{(n-1)} Z_{(n+2),(n-1)} + \cdots + \tau_{(n-1)} Z_{m,(n-1)} \\ \epsilon_n &= \alpha_n Z_{(n+1),n} + \beta_n Z_{(n+2),n} + \cdots + \tau_n Z_{m,n} \end{aligned} \tag{5.13}$$

At this point it is important to distinguish between different topologies, i.e. linear arrays with even or odd number of elements added in the peripheral area. This is due to the different behaviour of the mutual coupling effects in these two situations.

As the correction matrix has always the same shape for arrays with the same topologies, it may be employed in the estimation of the currents of bigger arrays. Nevertheless, a correction (δ) in the absolute value of each of the elements in the matrix should be applied depending on the topology of the array under study. This correction is quantified for the different array configurations employed in the current paper in terms of the number of elements added to the peripheral area (m). This should be done in order to induce a behavior law when there is enough number of simulation samples. As mentioned in the previous section, the behavior of δ, is not the same for different array topologies. This δ is the difference between the maximum absolute values of the data employed for the estimation and the data under estimation. When a behavior law is obtained a estimation for the currents can be achieved. It is important also to remark that with this method, it is not necessary to evaluate the mutual impedances matrix between the elements in the core and the elements added to the peripheral areas, as the predictions are made entirely from the data available from previous optimizations. The method is applied again to the three scenarios under study: linear, square and irregular arrays.

Linear Arrays

For the application of this method, the shape of the correction matrix for the linear array is shown in Fig. 5.22(a) for nine elements in the core and twenty elements in the peripheral area (ten on each side of the array). This matrix is employed in the estimation of the currents for bigger arrays up to one hundred and fourty elements in the peripheral area. Besides, a well-known behavior in mutual coupling for arrays is observed in this graph. For the edge elements, the correction that should be applied is higher, and it decreases with $1/R^2$ as we approach to the central elements. Also, the edge elements have a higher variance for the error within the same element (dipole, n_{abf} points). Thus, when a prediction is obtained this fact should be taken into account.

For the case of linear arrays, the δ parameter is estimated as shown in Fig. 5.22(b) for even and odd number of elements within m in the array. A third order interpolation has been computed, giving out an analytical solution for these curves. The mathematical expressions for these plots are given by

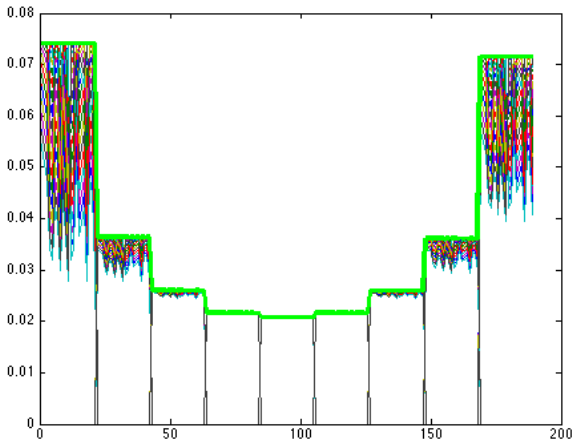

(a)

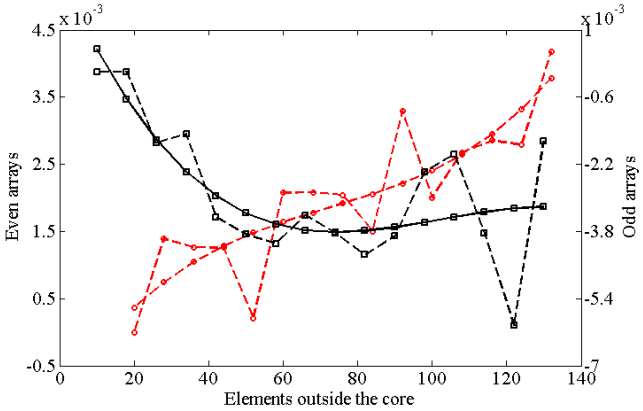

(b)

Figure 5.22: (a) Absolute value for impedances correction with $m = 20$, and (b) Offset for the error matrix in terms of elements added outside the core for even and odd arrays. Computed offset even ($*$ -solid), 3^{rd} order interpolation even ($*$ -dashed), computed offset odd ($\circ$ -solid), 3^{rd} order interpolation odd ($\circ$ -dashed).

Eqs. 5.14 - 5.15.

$$p_{even}(x) = a_3x^3 + a_2x^2 + a_1x + a_0 \begin{matrix} a_0 = -9.910^{-4} & a_1 = 8.510^{-5} \\ a_2 = -9.4610^{-7} & a_3 = 4.3610^{-9} \end{matrix} \quad (5.14)$$

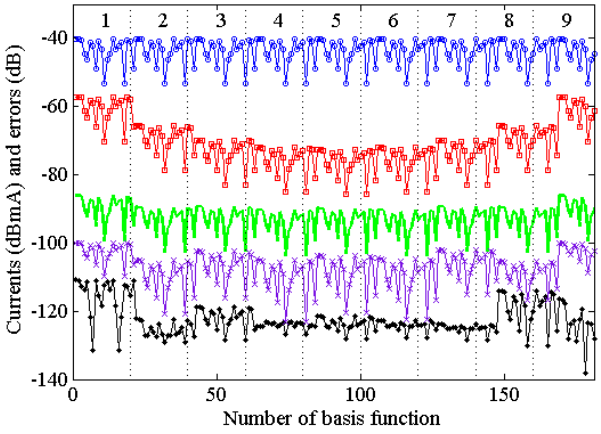

(a)

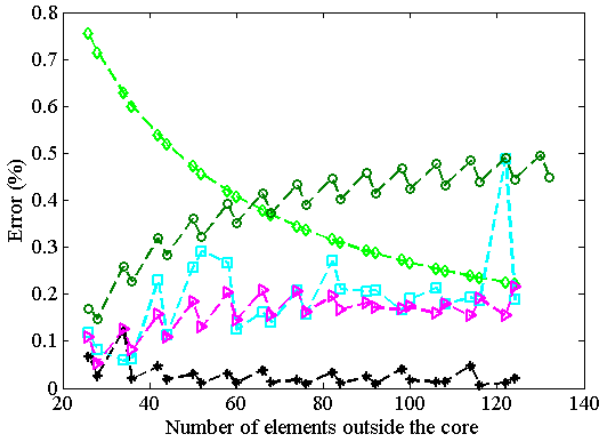

(b)

Figure 5.23: (a) Currents for a linear array: exact currents ($\circ$), error for isolated analysis ($\square$), error for one's correction (thick), error for PSO optimization ($\bullet$) and error for the estimation ($\times$); and (b) Error for different corrections: one's correction ($\Diamond$), optimized coefficients ($*$), correction without offset ($\circ$), prediction with offset ($\square$), interpolated offset ($\trianglerighteq$).

$$p_{odd}(x) = b_3x^3 + b_2x^2 + b_1x + b_0 \begin{matrix} b_0 = -9.910^{-4} & b_1 = 8.510^{-5} \\ b_2 = -9.4610^{-7} & b_3 = 4.3610^{-9} \end{matrix} \quad (5.15)$$

With the δ parameter quantified, an estimation for the currents is obtained, showing the results in Fig. 5.23(a) for $n = 9$ and $m = 68$. The exact

currents and the errors for the different methods of estimation are shown. The optimization is carried out with $m = 68$, and the prediction for the currents is achieved with the data of $m = 20$ and the δ estimated in Fig. 5.22(b). The error rates are 0.07% for the prediction and 0.01% for the optimized coefficients, while the isolated analysis remains over 6%.

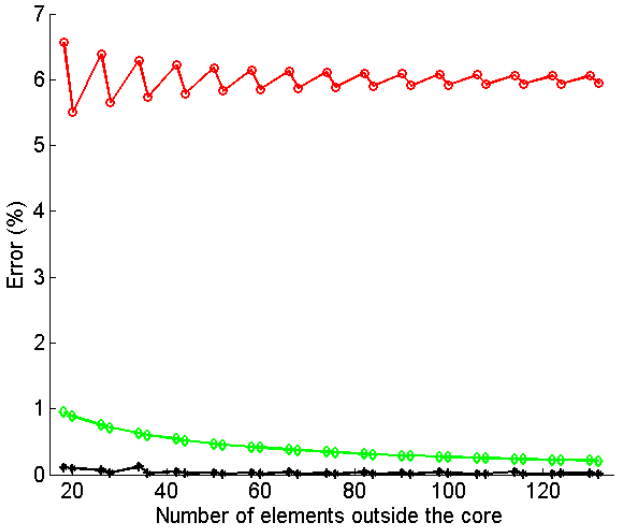

Figure 5.24: Error evolution for isolated analysis ($\circ$), coefficients set to one ($\Diamond$) and optimized coefficients ($*$) in terms of the peripheral elements.

Several simulations have been carried out for the different examples. The error rates for the different estimation methods versus the number of elements within m is depicted in Fig. 5.23(b). All the estimations are obtained from the data of $m = 20$ and $m = 18$ for even and odd arrays and the predictions are achieved until $m = 120$ and $m = 124$. There is a small difference between the error corresponding to the prediction using the data from the sampled δ parameter and for the interpolated δ.

Also the error for the correction without using δ is shown, giving a worse result for bigger arrays than the one's correction. The ripple seen in the different graphs corresponds to the even and odd number of elements added in m. It is important to remark the shape of the error for the one's correction. As the number of elements in m increases, it tends to the optimized error, that can be considered as an infinite array. The error for this method converges to the infinite array solution.

The predictions have been carried out from arrays with more than one hundred elements less and errors 50 dB lower have been achieved. It is also

important to notice than in most of the cases, the interpolated function gives error rates lower than the sampled data from simulations.

The ripple seen in this graph is due to the even/odd number of elements added to each side of the array. When the number of elements is small, i.e. five elements on each side, the ripple in the error is larger than with a high number of peripheral elements. This is due to the half-wavelength spacing between elements. Nevertheless, with the developed method, this error is constant and has no ripple, for both optimized elements and for the coefficients set to one.

Regular Square Arrays

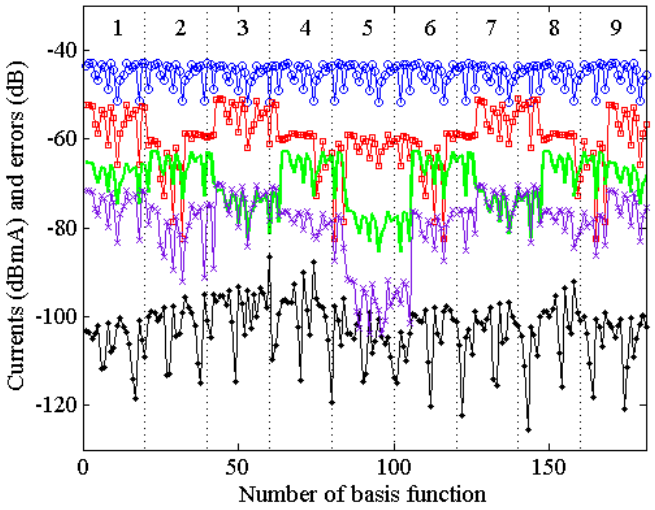

Figure 5.25: Prediction for a square array of 169 elements from the data of an array of 81 elements, with 9 elements in the core. Exact currents on the elements (∘) and errors for: isolated analysis (□), one's correction (thick), optimized coefficients (•) and prediction (×).

In the square array scenario, the correction technique is applied as in linear arrays. Also, a distinction between even and odd number of elements is applied. An example of the results obtained with this method is shown in Fig. 5.26, where an array of 169 (13×13) elements is analyzed with $n = 9$ and $m = 160$. The data obtained for the prediction is from the optimization of an square array of $m = 72$ elements. The estimation improves the error given by the coefficients set to one. The error rate for the isolated analysis, one's correction, prediction and PSO optimization are 24.5%, 6%, 2.8% and 0.17% respectively.

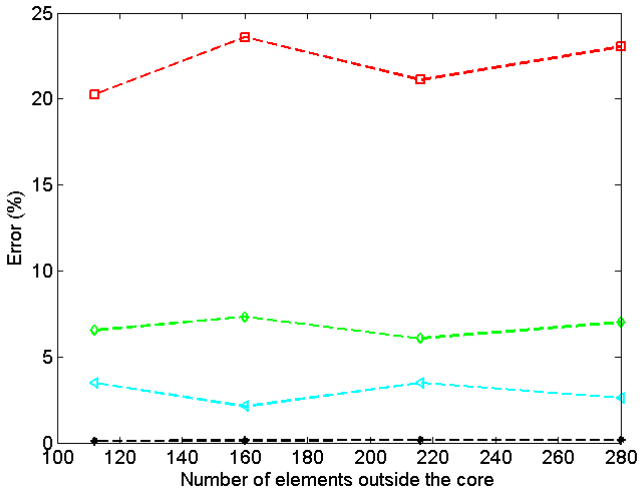

Figure 5.26: Error for differente corrections. Isolated analysis (□), one's correction (◊), optimized coefficients (∗), correction with offset (⊵).

5.5 Conclusions, future lines and contributions

In this Chapter, three different numerical methods are presented with the goal of optimizing the analysis time and computation resources of THz systems. The first one is based in QO techniques while the other two combine MoM with PO and optimization techniques.

The results obtained with the first method, the QO approach, throw a maximum error of 11%, being most of the discrepancies below 1%. The great advantage of this method is that as in a matter of seconds, it is possible to have an idea and to evaluate the focusing properties of a whole complex system, by only knowing the coefficients of the BME of the feed; the optical elements coefficients are already characterized by their geometrical parameters.

For both methods employing MoM, a reduction in the amount of computational resources has been demonstrated. First of all with the aid of the combination of PO+MoM, and then with the modification of the diagonal of the impedances matrix in a direction of considering the mutual coupling with surrounding elements, so they do not need to be included in the analysis reducing therefore the number of unknowns.

Some straightforward lines to continue the developing of this chapter are for example the introduction of difraction and misalignment properties on the QO software developed. Also, the introduction of a synthesis algorithm that

allows giving the paramters of the beam, the design of the focusing elements needed.

Regarding the MoM and PO analysis, the difraction by the edges and also the possible blockage of the structs holding a subreflector can be introduced. The introduction also of the analysis of feed elements with dielectric is also important, then any antenna can be evaluated. Also, for the array analysis, the method sould be validated for elements different than the dipoles, with more complexity on the impedances matrix.

The contributions of the content of this Chapter to international journals, conference papers and research stages are:

- B. Andrés-García, D. González-Ovejero, C. Craeye, L. E. García-Muñoz and D. Segovia-Vargas, "An iterative MoM/PO method based on a MBF/Krylov Approach", *IV European Conference on Computational Mechanics*, Paris, France, 2010.
- B. Andrés-García, L. E. García-Castillo, I. Gómez-Revuelto, L. E. García-Muñoz and C. Craeye, "Modular Approach to FEM-MoM Hybridization for the Analysis of Finite Array Antennas", *IV European Conference on Computational Mechanics*, Paris, France, 2010.
- J. Montero-de-Paz, O. García-Pérez, A. Rivera-Lavado, E. Ugarte-Muñoz, B. Andrés-García, M. Molina-Romero, T. Finn, J. A. López-Fernández, V. González-Posadas, L. E. García-Muñoz, D. Segovia-Vargas, "Focusing System for a 300GHz Radar with Two Target Distances", *EuCAP (European Conference on Antennas and Propagation)*, Rome, Italy, 2011.
- G. Dohler, S. Preu, S. Malzer, B. Andrés-García, L. E. García-Muñoz, "Large Area THz Emitters", *SPIE, Defense, Security, and Sensing 2011, Terahertz Physics, Devices and Systems V*, Orlando, Florida, 2011.
- J. Montero-de-Paz, J. Ancizu Vergara, B. Andrés-García, L. E. García-Muñoz and D. Segovia-Vargas, "Hemispheric Lens Design in the Millimeter and Sub-Millimeter regime", *URSI 2010*, Bilbao, Spain, September 2010.
- B. Andrés-García, D. González-Ovejero, C. Craeye, L. E. García-Muñoz and D. Segovia-Vargas, "An Iterative MoM/PO Method Based on a MBF/Krylov Approach", *EuCAP (European Conference on Antennas and Propagation)*, Barcelona, Spain, April 2010.
- C. Craeye, B. Andrés-García, L. E. García-Muñoz, R. Sarkis, "An Open Source Code for the Calculation of the Effects of Mutual Coupling in

Arrays of Wires and for the ASM-MBF Method", *International Journal of Antennas and Propagation, Invited paper*, Vol. 2010, 2010.

- M. Molina, "Implementación de una Herramienta para el Estudio Rápido de Sistemas Cuasi-Ópticos", *Proyecto de Fin de Carrera (Final Master's Project)*, October 2010.
- Research stage during 3 months at Université Catholique de Louvain, May-July 2009.

CHAPTER 6

Conclusions and Future Working Lines

6.1 Final Conclusions

In this thesis, different techniques both in analysis methods and new antenna topologies have been presented for the THz band. Each of them, comprises a part of a whole system and they are the initial step and a proof of concept for further development, optimization and design to obtain an efficient system in this frequency band. The antennas designed are based in planar technology, in substrate horns, end-fire and broadside antennas. As feeds, different kind of PM are employed, depending on the application such as interdigitated PM, or n-i-pn-i-p, as well as Schottky diodes in a receiving configuration.

There are three main blocks: broadside atennas, end-fire antennas and numerical methods. The goal for the three of them is to optimize the radiated power as well as to do a fast analysis of the systems.

In the first block, broadside antennas, a reduction and miniaturization of at least one order of magnitude of the antenna employed with n-i-pn-i-p photomixers as feeds is achieved, obtaining the same or higher efficiency as with previous designs. This allows the implementation in arrays, having therefore more beams radiating for a future phased array configuration or an imaging array. This has been implemented in ultra-wideband arrays, for two different types of single elements, log-spiral and log-periodic antennas, obtaining the same efficiency as for the reference elements.

With the aid of previous work, in Chapter 3, new 3-D structures, dielectric horns etched on the semiconductor substrates, have been designed. With these structures the power obtained out of the devices is higher than with the conventional systems with only a radiating element and a lens. The electromagnetic energy is coupled and focused in the structure, not allowing the spreading throughout the substrate due to the modes propagating in the horn and the semiconductor-air interface. The results have been verified in simulation, with both narrow and broadband elements, and also they have been validated with experimental results employing a n-i-pn-i-p photomixer, a log-spiral antenna, etched horn and a lens with no focusing properties.

The second block of this Thesis is based on end-fire antennas. The need of increase the efficiency and reduce the losses on the system, suggest to avoid the use of Si lenses, and employ end-fire antennas. The TSA is a suitable and efficient radiating element that can be implemented in high permittivity substrates if they have a suitable geometry. A modal theory has been developed, including a theoretical understanding of the substrate thickness limitations. It has been proven by the study of the fields, obtained with full wave simulations. Based on this theory, three different applications are presented: wedge antenna, EBG antenna and substrate-superstrate antenna. The wedge antenna assumes the implementation of the feeding in a semiconductor while the radiating element is over a low-permittivity substrate with a wedge geometry. Radiation patterns are found symmetrical for the manufactured devices, demonstrating this way the good performance of the device. The EBG was also manufactured, in the band of $[60 - 100]\ GHz$, obtaining also good results in terms of radiation patterns, and also impedance. Regarding the substrate-superstrate antenna, it was simulated with a full-wave analysis, achieving also good performance in the operation band, and a good and symmetrical end-fire radiation.

Regarding the third main area of this Thesis, there have been explored, implemented and verified some techniques to allow the design and analysis of structures with a reduced computational cost. QO techniques have been implemented, with the use of BME and characterization of lenses and mirrors with their respective beam transformation matrix. This way, a maximum error of 11% was obtained, allowing the design of a complex focusing system in a few seconds. Also, a MoM+PO hybrid method based on MBF/Krylov subspaces has been developed for the analysis of big structures like reflectors. The method is based on successive iterations employing the QR factorization for the orthogonalization of the subdomain Krylov base at every step. Some comparisons with exact solutions have been presented for the validation of the method. The use of approximations like PO allows the reduction of computing

resources and time with the aim of analyzing complex systems not affordable with conventional MoM, like structures with a diameter around 50 λ.

Future steps will involve corrections for scattering by the edges on the reflector. To continue with MoM analysis, large array analyses have been performed by the study of the MoM impedances matrix and the modification of it in terms of linear combination of the mutual coupling with smaller arrays. The method was applied in linear, square and random arrays, showing good performance in the three of them. Coefficients are obtained for the linear combination in order to optimize the methods, demonstrating this way the possibility of the analysis of arrays of more elements than in a full wave simulation. In a next step, the coefficients are optimized with PSO, demonstrating tha the error can be reduced to a very low level.

6.2 Future Working Lines

Most of the main working lines have been mentioned at the end of each of the chapters. Nevertheless, a general summary will be done here with a wider field of view over some applications and joint works between Chapters. All the work on this Thesis is focused on the analysis of devices on the THz range as well as the optimization of radiating elements in high permittivity substrates. Several types of antennas are designed, giving a starting point for some systems that can be developed on the future.

As a straightforward example is the excitation of arrays in Chapter 2 in a phased array configuration. This will allow the steering of the beam as well as to have a higher radiated power. Following with array configurations, sparse arrays can be designed in order to reduce the number of elements, and also the mutual coupling. It is important to note that most of the classical array theory can be applied here, if the positioning of the optical fibers to illuminate the photomixers can be implemented. With phase delay for the optical fibers, all the phase differences between elements can be achieved.

Regarding Chapter 3, the devices presented on this Thesis are only a proof of concept for future designs. The angle of the etching in the semiconductor should be improved as well as the implementation of a waveguide on the substrate. This will allow also to employ thicker wafers, being more robust for processing and manufacturing. To continue with Chapter 2 too, the implementation of this structure in an array configuration can lead to very high radiating power and also to maximize the efficiency of the system.

For end-fire antennas, the implementation of new geometries that lead to a suppresion of the high order modes is the main future line. As mentioned

in the conclusions of Chapter 4. One idea for this application is the etching of the central part of the substrate, acting as a mode supressor. The theory developed is also a first step for the study if this antennas; waveguide theory can be applied now to the design of them, having therefore a wide variety of options and models to study it. The experimental measurement of the devices can also be performed, especially the ones that could not be measured during this Thesis due to the lack of time on the stages. The array configuration shall be finished, and also the double sided-array.

To continue the developing of the numerical methods Chapter, in the MoM+PO approach, the difraction by the edges and the possible blockage of the structs for subreflectors can be introduced. Also, to include more elements on the system, such as lenses, or a Cassegrain configuration for example, with a subreflector and a main reflector. For the QO case, also discontinuities, and difraction can be included, as well as to improve the error for complex systems. Another future line for this software is the implementation of a synthesis algorithm that allows the design starting from other parameters of the system.

References

[1] C. A. Balanis, *Antenna theory: analysis and design*, 3rd ed. Hoboken, NJ: John Wiley, 2005.

[2] Y.-S. Lee, *Principles of terahertz science and technology*, 1st ed. New York, NY: Springer, 2008.

[3] B. Ferguson and X.-C. Zhang, "Materials for terahertz science and technology," *Nat Mater*, vol. 1, pp. 26-33, 2002.

[4] R. Köler, A. Tredicucci, F. Beltram, H. E. Beere, E. H. Linfield, A. G. Davies, D. A. Ritchie, R. C. Iotti, and F. Rossi, "Terahertz semiconductor hetero-structure laser," *Nature* 417, 156Ű159, 2002.

[5] B. S. Williams, "Terahertz quantum-cascade lasers," *Nat Photon*, vol. 1, pp. 517-525, 2007.

[6] C. M. Armstrong, "The truth about terahertz," *Spectrum*, IEEE, vol. 49, pp. 36-41, 2012.

[7] P. R. Smith, D. H. Auston, and M. C. Nuss, "Subpicosecond photoconducting dipole antennas," *Quantum Electronics, IEEE Journal of,* vol. 24, pp. 255-260, 1988.

[8] E. R. Brown and F. W. Smith and K. A. McIntosh,"Coherent millimeter-wave generation by heterodyne conversion in low-temperature-grown GaAs photoconductors", *Journal of Applied Physics*, vol. 73, pp. 1480-1484, 1993.

[9] J. Faist, F. Capasso, D. L. Sivco, C. Sirtori, A. L. Hutchinson, and A. Y. Cho, "Quantum Cascade Laser," *Science*, vol. 264, pp. 553-556, 1994.

[10] P.H. Siegel, "Terahertz Technology", *IEEE Trans. on Microwave Theory and Tech.*, Vol. 50, No. 3, pp. 910 - 928, Mar 2002.

[11] M. Tonouchi, "Cutting-edge Terahertz Technology", *Nature Photonics*, Vol. 1, pp. 97-105, 2007.

[12] D. M. Pozar, *Microwave engineering,* 4th ed. Hoboken, NJ: Wiley, 2012.

[13] T. W. Crowe, W. L. Bishop, D. W. Porterfield, J. L. Hesler, and R. M. Weikle, "Opening the terahertz window with integrated diode circuits," *Solid-State Circuits, IEEE Journal of*, vol. 40, pp. 2104-2110, 2005.

[14] R. J. Trew, "High-frequency solid-state electronic devices," Electron Devices, IEEE Transactions on, vol. 52, pp. 638-649, 2005.

[15] H. Eisele, "InP Gunn devices for 400-425 GHz," *Electronics Letters*, vol. 42, pp. 358-359, 2006.

[16] H. Eisele and R. Kamoua, "Submillimeter-wave InP Gunn devices," *Microwave Theory and Techniques, IEEE Transactions on,* vol. 52, pp. 2371-2378, 2004.

[17] N. Orihashi, S. Suzuki, and M. Asada, "One THz harmonic oscillation of resonant tunneling diodes," *Applied Physics Letters,* vol. 87, p. 233501, 2005.

[18] A. Maestrini, J. Bruston, D. Pukala, S. Martin, and I. Mehdi, "Performance of a 1.2 THz frequency tripler using a GaAs frameless membrane monolithic circuit," *Microwave Symposium Digest,* 2001 IEEE MTT-S International, 2001, pp. 1657-1660 vol.3.

[19] A. G. Davies, E. H. Linfield, and M. B. Johnston, "The development of terahertz sources and their applications," *Physics in Medicine and Biology,* vol. 47, p. 3679, 2002.

[20] B. S. Williams, S. Kumar, H. Qing, and J. L. Reno, "High-power terahertz quantum cascade lasers," *Lasers and Electro-Optics,* 2006 and 2006 Quantum Electronics and Laser Science Conference. CLEO/QELS 2006. Conference on, 2006, pp. 1-2.

[21] S. Kumar, B. S. Williams, S. Kohen, Q. Hu, and J. L. Reno, "Continuous-wave operation of terahertz quantum-cascade lasers above liquid-nitrogen temperature," *Applied Physics Letters*, vol. 84, pp. 2494-2496, 2004.

[22] C. Worrall, J. Alton, M. Houghton, S. Barbieri, H. E. Beere, D. Ritchie, and C. Sirtori, "Continuous wave operation of a superlattice quan-

tum cascade laser emitting at 2 THz," *Opt. Express,* vol. 14, pp. 171-181, 2006.

[23] C. Walther, M. Fischer, G. Scalari, R. Terazzi, N. Hoyler, and J. Faist, "Quantum cascade lasers operating from 1.2 to 1.6 THz," *Applied Physics Letters,* vol. 91, p. 131122, 2007.

[24] S. Fathololoumi, E. Dupont, C. W. I. Chan, Z. R. Wasilewski, S. R. Laframboise, D. Ban, A. Mátyás, C. Jirauschek, Q. Hu, and H. C. Liu, "Terahertz quantum cascade lasers operating up to 200 K with optimized oscillator strength and improved injection tunneling," *Opt. Express,* vol. 20, pp. 3866-3876, 2012.

[25] Q. Y. Lu, N. Bandyopadhyay, S. Slivken, Y. Bai, and M. Razeghi, "Room temperature single-mode terahertz sources based on intracavity difference-frequency generation in quantum cascade lasers," *Applied Physics Letters,* vol. 99, p. 131106, 2011.

[26] W. Shi, Y. J. Ding, and P. G. Schunemann, "Coherent terahertz waves based on difference-frequency generation in an annealed zincŰgermanium phosphide crystal: improvements on tuning ranges and peak powers," *Optics Communications*, vol. 233, pp. 183-189, 2004.

[27] K. Suizu and K. Kawase, "Monochromatic-Tunable Terahertz-Wave Sources Based on Nonlinear Frequency Conversion Using Lithium Niobate Crystal," *Selected Topics in Quantum Electronics, IEEE Journal of,* vol. 14, pp. 295-306, 2008.

[28] W. Shi, Y. J. Ding, N. Fernelius, and K. Vodopyanov, "Efficient, tunable, and coherent 0.18-5.27-THz source based on GaSe crystal," *Opt. Lett.,* vol. 27, pp. 1454-1456, 2002.

[29] E. Nichols and J. Tear, " Joining the infra-red and electric wave spectra," *Astrophysical Journal,* vol. 61, pp. 17-37, 1925.

[30] T. de Graauw, et al, "The Herschel-Heterodyne Instrument for the Far-Infrared (HIFI)*," *A&A,* vol. 518, p. L6, 2010.

[31] M. C. Kemp, "Millimetre wave and terahertz technology for the detection of concealed threats: a review," *Proc. SPIE 6402, Optics and Photonics for Counterterrorism and Crime Fighting II*, September 2006.

[32] R. Appleby and H. B. Wallace, "Standoff Detection of Weapons and Contraband in the 100 GHz to 1 THz Region," *Antennas and Propagation, IEEE Transactions on,* vol. 55, pp. 2944-2956, 2007.

[33] P. U. Jepsen, D. G. Cooke, and M. Koch, "Terahertz spectroscopy and imaging Ű Modern techniques and applications," *Laser & Photonics Reviews,* vol. 5, pp. 124-166, 2011.

[34] D. L. Woolard, R. Brown, M. Pepper, and M. Kemp, "Terahertz Frequency Sensing and Imaging: A Time of Reckoning Future Applications?," *Proceedings of the IEEE,* vol. 93, pp. 1722-1743, 2005.

[35] http://www.teraview.com/.

[36] http://www.picometrix.com/.

[37] http://www.toptica.com/.

[38] http://www.traycer.com/.

[39] B. B. Hu and M. C. Nuss, "Imaging with terahertz waves," *Opt. Lett.,* vol. 20, pp. 1716-1718, 1995.

[40] T. Kleine-Ostmann, P. Knobloch, M. Koch, S. Hoffmann, M. Breede, M. Hofmann, G. Hein, K. Pierz, M. Sperling, and K. Donhuijsen, "Continuous-wave THz imaging," *Electronics Letters,* vol. 37, pp. 1461-1463, 2001.

[41] V. P. Wallace, A. J. Fitzgerald, S. Shankar, N. Flanagan, R. Pye, J. Cluff, and D. D. Arnone, "Terahertz pulsed imaging of basal cell carcinoma ex vivo and in vivo," *British Journal of Dermatology,* vol. 151, pp. 424-432, 2004.

[42] A. J. Fitzgerald, V. P. Wallace, M. Jimenez-Linan, L. Bobrow, R. J. Pye, A. D. Purushotham, and D. D. Arnone, "Terahertz Pulsed Imaging of Human Breast Tumors," *Radiology,* vol. 239, pp. 533-540, 2006.

[43] D. Crawley, C. Longbottom, V. P. Wallace, B. Cole, D. Arnone, and M. Pepper, "Three-dimensional terahertz pulse imaging of dental tissue," *Journal of Biomedical Optics,* vol. 8, pp. 303-307, 2003.

[44] M. v. Exter, C. Fattinger, and D. Grischkowsky, "Terahertz time-domain spectroscopy of water vapor," *Opt. Lett.,* vol. 14, pp. 1128-1130, 1989.

[45] D. F. Plusquellic, K. Siegrist, E. J. Heilweil, and O. Esenturk, "Applications of terahertz spectroscopy in biosystems," *Chemphyschem,* vol. 8, pp. 2412-31, 2007.

[46] K. Fukunaga, Y. Ogawa, S. i. Hayashi, and I. Hosako, "Terahertz spectroscopy for art conservation," *IEICE Electronics Express,* vol. 4, pp. 258-263, 2007.

[47] J. B. Jackson, M. Mourou, J. F. Whitaker, I. N. Duling Iii, S. L. Williamson, M. Menu, and G. A. Mourou, "Terahertz imaging for

non-destructive evaluation of mural paintings," *Optics Communications,* vol. 281, pp. 527-532, 2008.

[48] A. J. L. Adam, P. C. M. Planken, S. Meloni, and J. Dik, "TeraHertz imaging of hidden paintlayers on canvas," *Opt. Express,* vol. 17, pp. 3407-3416, 2009.

[49] N. Krumbholz, T. Hochrein, N. Vieweg, T. Hasek, K. Kretschmer, M. Bastian, M. Mikulics, and M. Koch, "Monitoring polymeric compounding processes inline with THz time-domain spectroscopy," *Polymer Testing,* vol. 28, pp. 30-35, 2009.

[50] Y. C. Shen, "Terahertz pulsed spectroscopy and imaging for pharmaceutical applications: a review," *Int J Pharm,* vol. 417, pp. 48-60, 2011.

[51] J. A. Zeitler and Y.-C. Shen, *Terahertz Spectroscopy and Imaging.* Berlin Heidelberg: Springer 2013.

[52] Y. C. Shen, T. Lo, P. F. Taday, B. E. Cole, W. R. Tribe, and M. C. Kemp, "Detection and identification of explosives using terahertz pulsed spectroscopic imaging," *Applied Physics Letters,* vol. 86, p. 241116, 2005.

[53] Y. Shen, P. F. Taday, and M. C. Kemp, "Terahertz spectroscopy of explosive materials," *Proceedings of SPIE,* vol. 5619, pp. 82-89, 2004.

[54] K. Kawase, Y. Ogawa, Y. Watanabe, and H. Inoue, "Non-destructive terahertz imaging of illicit drugs using spectral fingerprints," *Opt. Express,* vol. 11, pp. 2549-2554, 2003.

[55] P. Mousavi, F. Haran, D. Jez, F. Santosa, and J. S. Dodge, "Simultaneous composition and thickness measurement of paper using terahertz time-domain spectroscopy," *Appl. Opt.,* vol. 48, pp. 6541-6546, 2009.

[56] D. Banerjee, W. von Spiegel, M. D. Thomson, S. Schabel, and H. G. Roskos, "Diagnosing water content in paper by terahertz radiation," *Opt. Express,* vol. 16, pp. 9060-9066, 2008.

[57] J. Federici and L. Moeller, "Review of terahertz and subterahertz wireless communications," *Journal of Applied Physics,* vol. 107, p. 111101, 2010.

[58] D. Saeedkia, *Handbook of terahertz technology for imaging, sensing and communications.* Cambridge , UK: Woodhead, 2013.

[59] T. Kleine-Ostmann, K. Pierz, G. Hein, P. Dawson, and M. Koch, "Audio signal transmission over THz communication channel using semiconductor modulator," *Electronics Letters,* vol. 40, pp. 124-126, 2004.

[60] T.-A. Liu, G.-R. Lin, Y.-C. Chang, and C.-L. Pan, "Wireless audio and burst communication link with directly modulated THz photoconductive antenna," *Opt. Express,* vol. 13, pp. 10416-10423, 2005.

[61] T. M. Korter and D. F. Plusquellic, "Continuous-wave terahertz spectroscopy of biotin: vibrational anharmonicity in the far-infrared," *Chemical Physics Letters,* vol. 385, pp. 45-51, 2004.

[62] W. Zhang, E. R. Brown, M. Rahman, and M. L. Norton, "Observation of terahertz absorption signatures in microliter DNA solutions," *Applied Physics Letters,* vol. 102, p. 023701, 2013.

[63] F. Hindle, A. Cuisset, R. Bocquet, and G. Mouret, "Continuous-wave terahertz by photomixing: applications to gas phase pollutant detection and quantification," *Comptes Rendus Physique,* vol. 9, pp. 262-275, 2008.

[64] I. S. Gregory, W. R. Tribe, C. Baker, B. E. Cole, M. J. Evans, L. Spencer, M. Pepper, M. Missous, "Continuous-Wave Terahertz System with a 60 dB Dynamic Range", *Applied Physics Letters,* Vol. 86, No. 20, pp. 204104 - 204104-3, May 2005.

[65] J. Karsten, H. Quast, R. Leonhardt, T. Loffler, M. Thomson, T. Bauer, H. G. Roskos, and S. Czasch, "Continuous-wave all-optoelectronic terahertz imaging," *Applied Physics Letters,* vol. 80, pp. 3003-3005, 2002.

[66] R. Wilk, F. Breitfeld, M. Mikulics, and M. Koch, "Continuous wave terahertz spectrometer as a noncontact thickness measuring device," *Appl. Opt.,* vol. 47, pp. 3023-3026, 2008.

[67] B. Thomas, A. Maestrini, J. Gill, C. Lee, R. Lin, I. Mehdi and P. de Maagt, "A Broadband $835 - 900$ GHz Fundamental Balanced Mixer Based on Monolithic GaAs Membrane Schottky Diodes", *IEEE Trans. on Microwave Theory and Techniques*, vol. 58, no. 7, pp. 1917 - 1924, July 2010.

[68] Ivan Camara-Mayorga, "Photomixers as tunable terahertz local oscillators" Doctoral Dissertation by, *Max Planck Institute fur Radioastronomie*, Bonn, 2008.

[69] A. Stohr, A. Malcoci, A. Sauerwald, I. Camara Mayorga, R. Güsten, D. S. Jäger, "Utra-Wide-Band Travelling Wave Photodetectors for Photonic Local Oscillators", *Journal of Lightwave Technology*, Vol. 21, No. 12, pp. 3062 - 3070, Dec 2003.

[70] E. R. Brown, "THz generation by photomixing in ultrafast photoconductors," *Int. J. High Speed Electron. and Systems*, 13, 497, pp. 147 - 195, 2003.

[71] H. Ito, F. Nakajima, T. Futura, and T. Ishibashi, "Continuous THz-wave generation using antenna-integrated uni-travelling-carrier photodiodes," *Semicond. Sci. Technol.*, 20, 191, pp. 141 - 150, 2005.

[72] G. H. Döhler, F. Renner, O. Klar, M. Eckardt, A. Schwanhuer, S. Malzer, D. Driscoll, M. Hanson, A. C. Gossard, G. Loata, T. Löffler, and H. Roskos, "THz-photomixer based on quasi-ballistic transport," *Semicond. Sci. Technol.*, 20, pp. 178 - 190, 2005.

[73] I. Camara-Mayorga, A. Schmitz, T. Klein, C. Leinz and R. Gusten, "First In-Field Application of a Full Photonic Local Oscillator to Terahertz Astronomy," *IEEE Trans. on Terahertz Science and Technology*, vol. 2, no. 4, pp. 393-399, July 2012.

[74] A. Maestrini, J. S. Ward, C. Tripon-Canseliet, J. J. Gill, C. Lee, H. Javadi G. Chattopadhyay, and I. Mehdi, "In-Phase Power-Combined Frequency Triplers at 300 GHz," *IEEE Microwave and Wireless Components Letters*, March 2008.

[75] Sascha Preu, "Continuous-Wave, Tunable THz n-i-pn-i-p Superlattice Photomixers and Applications" Doctoral Dissertation by, *Erlangen Scientific Press, progress in modern optics 30*, Erlangen, 2009.

[76] S. Preu, F. H. Renner, S. Malzer, G. H. Döhler, L. J. Wang, M. Hanson, A. C. Gossard, T. L. J. Wilkinson, R. E. Brown, "Efficient Terahertz Emission from Ballistic Transport Enhanced n-i-p-n-i-p Superlattice Photomixers", *Applied Physics Letters*, Vol. 90, No. 21, pp. 212115 - 212115-3, May 2007.

[77] Y. Mushiake, "Self-complementary antennas, " *IEEE Antennas and Propagation Magazine* Vol. 34, Issue 6, De. 1992.

[78] S. Preu, G. Döhler, L. Wang, A. Gossard, "Tunable, continous-wave Terahertz photomixer sources and applications," *Journal of Applied Physics*, Vol. 109, No. 061301, 2011.

[79] E. A. Michael, I. Camara-Mayorga, R. Gusten, A. Dewald, R. Schieder, "Terahertz continuous-wave large-area travelling-wave photomixers on high-energy low-dose ion-implanted GaAs" *Applied Physics Letters*, Vol. 90, Issue. 17, pp. 171109-171109-3, 2007.

[80] D. F. Filipovic, S. S. Gearhart, G. M. Rebeiz, "Double-Slot Antennas on Extended Hemispherical and Elliptical Silicon Dielectric Lenses,"

IEEE Trans. Microwave Theory Tech., vol. 41, no. 10, pp. 1738-1749, October 1993.

[81] CST Microwave Studio 2011.

[82] John L. Volakis. *Antenna Engineering Handbook*, McGraw Hill, 2007.

[83] E. E. Altshuler, "Self- and Mutual Impedances on Travelling-Wave Linear Antennas" *IEEE Trans. on Antennas and Propagation*, vol. 37, no. 10, pp. 1312-1316, October 1989.

[84] D. E. J. Humphrey, V. F. Fusco, S. Drew, "Active Antenna Array Behavior," *IEEE Trans. Microwave Theory and Techniques*, vol. 43, no.8, pp. 1819Ű1825, August 1995.

[85] P. R. Haddad, D. M. Pozar, "Anomalous Mutual Coupling Between Microstrip Antennas," *IEEE Trans. Antennas and Propagation*, vol. 42, no. 11, pp. 1545Ű1549, November 1994.

[86] C. A. Balanis *Advanced Engineering Electromagnetics*, John Wiley and Sons, New York, 1989.

[87] E. de Lera Acedo, E. Garcia, V. Gonzalez-Posadas, J. L. Vazquez-Roy, R. Maaskant, D. Segovia, "Study and Design of a Differentially-Fed Tapered Slot Antenna Array", *IEEE Trans. Antennas Propagat.*, vol. 58, pp. 68-78, Jan. 2010.

[88] G. M. Rebeiz, L. P. B. Katehi, W. Y. Ali-Ahmad, G. V. Eleftheriades and C. C. Ling, "Integrated Horn Antennas for Millimeter-Wave Applications", *IEEE Transactions on Antennas and Prop. Magazine*, Vol. 34, No. 1, pp. 7 - 16, Feb. 1992.

[89] A. D. Olver, P. J. Clarricoats, "Dielectric cone loaded horn antennas", *IEE Proceedings*, Vol. 135, No. 3, pp. 158-162, Jun. 1998.

[90] S. K. Palit, W. Perris, "Dielectric-loaded pyramidal horns", *JEEE*, Aust., vol.16, no.2, p.139-146, 1996.

[91] Erik Lier, "A dielectric hybrid mode antenna feed: a simple alternative to the corrugated horn", *IEEE Trans. Antennas Propagat.*, vol. 34, no. 1 pp. 21-29, Jan 1986.

[92] G. V. Eleftheriades, W. Y. Ali-Ahmad, L. P. B. Katehi, G. M. Rebeiz, "Millimeter-Wave Integrated-Horn Antennas: Part I Theory", *IEEE Transactions on Antennas and Prop.*, Vol. 39, No. 11, pp. 1575 - 1581, Nov. 1991.

[93] I. A. Eshrah, A. B. Yakovlev, A. A. Kishk, A. W. Glisson, G. W. Hanson, "The TE_{00} waveguide mode - the "complete" story", *IEEE Antennas*

and Propagation Magazine, page(s): 33 - 41 , Volume: 46 Issue: 5, Oct. 2004.

[94] A. J. Marcatili, "Dielectric rectangular waveguide and directional coupler for integrated optics", *Bell Syst. Tech. J.* 48: 2071-102, 1969.

[95] P. Elias, I. Kostic, J. Soltys and S Hasenöhrl, "Wet-etch bulk micromachining of (100) InP substrates", *J. Micromech. Microeng.* Vol. 14, pp. 1205 - 1214, 2004.

[96] P. J. Gibson, "The Vivaldi aerial", *Proc. 9th Eur. Microwave Conf.*, Brighton, U.K., pp. 101 - 105, June 1979.

[97] K. S. Yngvesson, D. H. Schaubert, T. L. Korzeniowski, E. L. Kollberg, T. Thungren, and J. F. Johansson, "Endfire tapered slot antennas on dielectric substrates", *IEEE Trans. Antennas Propagat.*, vol. 33, pp. 1392-1400, Dec. 1985.

[98] K. S. Yngvesson, T. L. Korzeniowski, Y. S. Kim, E. L. Kollberg, and J. F. Johansson, "The Tapered Slot Antenna: A new integrated element for millimeter wave applications", *IEEE Trans. Microwave Theory Tech.*, vol. 37, pp. 365-374, Feb. 1989.

[99] R. Maaskant, M. V. Ivashina, O. Iupikov, E. A. Redkina, S. Kasturi, D. H. Schaubert, "Analysis of Large Microstrip-Fed Tapered Slot Antenna Arrays by Combining Electrodinamic and Quasi-Static Field Modes", *IEEE Trans. on Antennas and Prop.*, Vol. 59, Nr. 6, pp. 1798-1807, 2011.

[100] M. V. Ivashina, O. Iupikov, R. Maaskant, W. A. van Cappellen, T. Oosterloo, "An Optimal Beamforming Strategy for Wide-Field Surveys With Phased-Array-Fed Reflector Antennas", *IEEE Trans. on Antennas and Prop.*, Vol. 59, Nr. 6, pp. 1864-1875, 2011.

[101] B. Andres-Garcia, L. E. Garcia-Munoz, I. Camara-Mayorga, D. Segovia-Vargas, R. Gusten, "Antenna in the Terahertz Band for Radioastronomy applications", *Proceedings of the Fourth European Conference on Antennas and Propagation (EuCAP), 2010*, Page(s): 1, 4, 2010.

[102] R. Janaswamy, D. H. Schaubert, and D. M. Pozar, "Analysis of the transverse electromagnetic mode linearly tapered slot antenna", *Radio Science*, vol. 21, no. 5, pp. 797-804, Sept.-Oct. 1986.

[103] R. Janaswamy, D. H. Schaubert, "Characteristic impedance of a Wide Slotline on Low-Permittivity Susbtrates", *IEEE Trans. On Microwave Theory and Techniques*, Vol. 34, no. 8, pp. 900-902, August 1986.

[104] R. Janaswamy, D. H. Schaubert, "Analysis of the Tapered Slot Antenna", *IEEE Trans. Antennas Propagat.*, vol. 35, no. 9, pp. 1058-1065, Sept. 1987.

[105] H. Holter, T.-H. Chio, and D. H. Schaubert, "Elimination of impedance anomalies in single- and dual-polarized endfire tapered slot phased arrays", *IEEE Trans. Antennas Propagat.*, vol. 48, pp. 122âĂŞ124, Jan. 2000.

[106] D. Schaubert, "A class of E-plane scan Blindnesses in single-polarized arrays of tapered-slot antennas with a ground plane", *IEEE Trans. Antennas Propag.*, vol. 44, no. 7, pp. 954-959, Jul. 1996.

[107] J. B. Rizk, G. M. Rebeiz, "Millimeter-wave Fermi tapered slot antennas on micromachined silicon substrates", *IEEE Transactions on Antennas and Propagation* Volume: 50 , Issue: 3, Page(s): 379-383, March 2002.

[108] R. Maaskant, *Analytical and Numerical Modeling of Currents on Vivaldi Antennas for Radio Astronomy*, Technische Universiteit Eindhoven, 2003.

[109] B. Stockbroeckx, A. Vander Vorst, "Electromagnetic Modes in Conical Transmission Lines with Application to the Linearly Tapered Slot Antenna", *IEEE Trans. Antennas Propagat.*, vol. 48, pp. 447-455, March. 2000.

[110] B. Stockbroeckx, A. Vander Vorst, "Copolar and Cross-polar radiation of Vivaldi antenna on dielectric substrate", *IEEE Trans. Antennas Propagat.*, vol. 48, pp. 19-25, Jan. 2000.

[111] P. J. Gibson, "The Vivaldi Aerial", *Microwave conference, 1979. 9th European*, pp. 101-105, September 1979.

[112] I. S. Gregory, C. Baker, W. R. Tribe, M. J. Evans, H. E. Beere, E. H. Linfield, A. G. Davies and M. Missous, “High resistivity annealed low-temperature GaAs with 100 fs. lifetimes", *Journal of Applied Physics*, vol. 83, pp. 4199, 2003.

[113] D. B. Rutledge, D. P. Neikirk and D. P. Kasilingam,“Infrared and Millimeter Waves", pp. 1-90, vol. 10, ed. K. J. Button, Academic, New York, 1983.

[114] I. Camara Mayorga, P. Muñoz Pradas, E. A. Michael, M. Mikulics, A. Schmitz, P. van der Wal, C. Kaseman, R. Güsten, K. Jacobs, M. Marso, H. Luth, P. Kordos, "Terahertz photonic mixers as local

oscillators for hot electron bolometer and superconductor-insulator-superconductor astronomical receivers", *Journal of Applied Physics*, vol. 100, no. 4, pp. 043116 - 043116-4, Aug. 2006.

[115] I. Cámara Mayorga, E. A. Michael, A. Schmitz, P. van der Wal, R. Güsten, K. Maier and A. Dewald,"Terahertz photomixing in high energy oxygen- and nitrogen-ion-implanted GaAs", *Applied Physics Letters*, vol. 91, pp.1107-1109, 2007.

[116] Feko SWuite 6.0.

[117] Ansoft HFSS 13.

[118] Juan Enrique Page, Jesus Maria Rebollar, Jose Antonio Encinar, *Temas avanzados en teoria electromagnetica*, Universidad Politecnica de Madrid, Departamento de Electromagnetismo y Teoria de Circuitos, Madrid, 1992.

[119] P. J. Clarricoats, A. D. Olver, "Corrugated horns for microwave antenas", *Peter Peregrinus IEE Books*, London, 1984.

[120] D. Marcuse, *Theory of dielectric optical waveguides* , American Telephone and Telegraph Company, American Press, 1991.

[121] R. N. Simons, *Coplanar Waveguide Circuits, Components, and Systems*, 1st ed. New York, US: John Wiley & Sons, Inc. 2001.

[122] P. F. Goldsmith, "ÍQuasioptical Systems: Gaussian Beam Quasioptical Propagation and Applications," 1st ed. IEEE Press, 1998.

[123] S. E. Schwarz, "Efficiency of quasi-optical couplers," *Int. J. Infrared Millimeter Waves*, vol.5 no.12, pp. 321-325, 1984.

[124] B. A. Munk, *Frequency Selective Surfaces: Theory and Design*, John Wiley & Sons, 2005.

[125] F. Yang, Y. Rahmat-Samii, *Electromagnetic Band Gap Structures in Antenna Engineering*, Cambridge University Press, 2009.

[126] R. Mittra, "Techniques for analyzing frequency selective surfaces - a review", *Proceedings of the IEEE*, Vol. 76, Issue 12, pp. 1539-1615 Dec. 1988.

[127] Matlab. [Online]. Available at http://www.mathworks.com

[128] Ta-Shing Chu, "An Imaging Beam Waveguide Feed," *IEEE Trans. Antennas Prop.*, vol. 31, no. 4, pp. 614-619, May 1983.

[129] L. E. Garcia Muñoz, "Contribución al Estudio de la Focalización Multibanda de Radiotelescopios," *Universidad Politécnica de Madrid*, Nov. 2003.

[130] K.B. Cooper, N. Llombart and R.J. Dengler, "Confocal ellipsoidal reflector system for a mechanically scanned active terahertz imager," *IEEE Trans. Antennas Prop.*, vol. 58, no. 6, pp. 1834-1841, June 2010.

[131] R. J. Wylde, "Millimeter wave Gaussian beam-mode optics and corrugated feed horns", *IEE Proc. H, Microwaves, Opt. & Antennas*,13, pp. 258-262, 1984.

[132] M. Djordjevic and B. M. Notaros, "Higher Order Hybrid Method of Moments-Physical Optics Modeling Technique for Radiation and Scattering From Large Perfectly Conducting Surfaces," *IEEE Trans. Antennas Prop.*, vol. 53, no. 2, Feb. 2005.

[133] M. Carr and J.L. Volakis, "A Generalized Framework for Hybrid Simulation of Multi-Component Structures Using Iterative Field Refinement," *IEEE Antennas and Prop. Magazine*, vol. 48, no. 1,pp. 22-32, Feb. 2006.

[134] R.E. Hodges and Y. Rahmat-Samii, "An Iterative Current-Based Hybrid Method for Complex Structures," *IEEE Trans. Antennas Prop.*, vol. 45, no. 2, pp. 265-276, Feb. 1997.

[135] U. Jakobus and F. Landstorfer, "Improved PO-MM Hybrid Formulation for Scattering from Three-Dimensional Perfectly Conducting Bodies of Arbitrary Shape," *IEEE Trans. Antennas Prop.*, vol. 43, no. 2, pp . 162-169, Feb. 1995.

[136] J.Yeo, V.Prakash and R.Mittra, "Efficient Analysis of a class of microstrip antennas using the Characteristic Basis Function Method (CBFM)," *Microwave Optical Technol. Letters*, vol. 39, pp. 456-464, Dec. 2003.

[137] E. Suter and J.R. Mosig, "A subdomain multilevel approach for the efficient MoM analysis of large planar antennas," *Microwave Optical Technol. Letters*, vol. 26, pp. 270Ð277, Aug. 2000.

[138] C. Craeye, "On the connection between multiple-scattering based Macro Basis Functions and Krylov subspace methods," *Proc. of ICEAA conference*, Torino, Sep. 14-18, 2008.

[139] R. C. Hansen, *Phased Array Antennas,* John Wiley & Sons, Nov. 2009.

[140] S.M. Rao, D.R. Wilton and A. W. Glisson, "Electromagnetic Scattering by Surfaces of Arbitrary Shape," *IEEE Trans. Antennas Prop.*, vol. 30, no. 3, pp. 409-418, May 1982.

[141] J. Kennedy, R. Eberhart, “Particle Swarm Optimization," *Proceedings of IEEE International Conference on Neural Networks IV*. pp. 1942Ű1948, 1995.

List of Publications and Awards

Awards

- October 2010: Spanish Education and Science Ministry (MEC) Official Grant (FPU) for funding his doctoral research activity.
- May 2009: XXIX AEIT/COIT (Official Association of Spanish Telecommunication Engineers) Best Thesis Dissertation Award on Security and Defense.
- April 2009: Short-Term Scientific Mission funded by the European Action COST ic0603 ASSIST (Antenna Systems & Sensors for Information Society Technologies).
  Host institution: Universitè Catholique de Louvain. Directed by Prof. Christophe Craeye.

Peer Reviewed Journal Publications

- B. Andrés-García, L.E. García-Muñoz, V. González-Posadas, F. J. Herráiz-Martínez and D. Segovia-Vargas, "Filtering Lens Structure Based on SRR for the Low Terahertz Band", *Progress in Electromagnetic Research*, pp. 71-90, Vol. 93, 2009.
- B. Andrés-García, L.E. García-Muñoz, V. González-Posadas and D. Segovia-Vargas, "Super-Dense Array emulating the Huma eye Vision Properties", *Microwave and Optical Technology Letters*, Vol. 51, No. 12, 2009.
- C. Craeye, B. Andrés-García, L. E. García-Muñoz, R. Sarkis, "An Open Source Code for the Calculation of the Effects of Mutual Coupling in Arrays of Wires and for the ASM-MBF Method", *International Journal of Antennas and Propagation, Invited paper*, Vol. 2010, 2010.
- B. Andrés-García, L.E. García-Muñoz, I. Cámara-Mayorga, D. Segovia-Vargas, and R. Gusten, "Ultrawideband Antenna Excited by a Photomixer in the Low Terahertz Band", *Progress in Electromagnetic Research*, vol. 114, pp. 1-15, 2011.
- B. Andrés-García, L. E. García-Muñoz, S. Bauersmidth, S. Preu, S. Malzer, G. Dohler, L. J. Wang and D. Segovia-Vargas, "Gain Enhancement by Dielectric Horns in the Terahertz band", *IEEE Transactions on Antennas and Propagation*, vol. 59, no. 9, September 2011.
- A. Rivera-Lavado, L. E. García-Mu´ noz, S. Bauersmidth, S. Preu, S. Malzer, G. Dohler, B. Andrés-García and D. Segovia-Vargas, "Arrays and New Antenna Topologies for Increasing THz Power Generation Using Photomixers", *Journal of Infrarred, Millimeter and Terahertz Waves*, vol. 34, no. 2, January 2013.

Conference Papers

- B. Andrés-García, E. García-Muñoz, V. González-Posadas, D. Segovia-Vargas "Super-Dense Array Emulating the Human Eye Vision Properties", *European Conference on Antennas and Propagation*, Berlin, Germany, April 2009.
- B. Andrés-García, L. E. García-Muñoz, V. González-Posadas, D. Segovia-Vargas, "Filtering Lens Structure Based on SSRs in the Low Terahertz Band", *Metamaterials 2009*, London, UK, September 2009.
- B. Andrés-García, D. González-Ovejero, C. Craeye, L. E. García-Muñoz and D. Segovia-Vargas, "An iterative MoM/PO method based on a

MBF/Krylov Approach", *IV European Conference on Computational Mechanics*, Paris, France, 2010.

- B. Andrés-García, L. E. García-Castillo, I. Gómez-Revuelto, L. E. García-Muñoz and C. Craeye, "Modular Approach to FEM-MoM Hybridization for the Analysis of Finite Array Antennas", *IV European Conference on Computational Mechanics*, Paris, France, 2010.
- B. Andrés-García, L. E. García-Muñoz I. Cámara, R. Gusten and D. Segovia-Vargas, "Antenna in the Terahertz Band for Radioastronomy applications", *EuCAP (European Conference on Antennas and Propagation)*, Barcelona, Spain, April 2010.
- B. Andrés-García, D. González-Ovejero, C. Craeye, L. E. García-Muñoz and D. Segovia-Vargas, "An Iterative MoM/PO Method Based on a MBF/Krylov Approach", *EuCAP (European Conference on Antennas and Propagation)*, Barcelona, Spain, April 2010.
- J. Montero-de-Paz, J. Ancizu Vergara, B. Andrés-García, L. E. García-Muñoz and D. Segovia-Vargas, "Hemispheric Lens Design in the Millimeter and Sub-Millimeter regime", *URSI 2010*, Bilbao, Spain, September 2010.
- B. Andrés-García, L. E. García-Muñoz, I. Cámara, D. Segovia-Vargas and R. Gusten, "Antenna in the Terahertz band for Radioastronomy Applications", *URSI 2010*, Bilbao, Spain, September 2010.
- G. Dohler, S. Preu, S. Malzer, B. Andrés-García, L. E. García-Muñoz, "Large Area THz Emitters", *SPIE, Defense, Security, and Sensing 2011, Terahertz Physics, Devices and Systems V*, Orlando, Florida, 2011.
- B. Andrés-García, L.E. García-Muñoz, S. Bauersmidth, S. Preu, S. Malzer, G. Dohler, L. J. Wang, D. Segovia-Vargas, "Dielectric Horn Antennas in the Terahertz Band", *EuCAP (European Conference on Antennas and Propagation)*, Rome, Italy, 2011.
- J. Montero-de-Paz, O. García-Pérez, A. Rivera-Lavado, E. Ugarte-Muñoz, B. Andrés-García, M. Molina-Romero, T. Finn, J. A. López-Fernández, V. González-Posadas, L. E. García-Muñoz, D. Segovia-Vargas, "Focusing System for a 300GHz Radar with Two Target Distances", *EuCAP (European Conference on Antennas and Propagation)*, Rome, Italy, 2011.
- Belén Andrés García, Luis Enrique García Muñoz, Sebastian Bauerschmidt, Sascha Preu, Stefan Malzer, Gottfried Dohler, Linjun Wang and Daniel Segovia Vargas, "Dielectric Horn Antennas in the Terahertz Band", *URSI 2011*, Madrid, Spain, 2011.

Appendix I

Mask for antenna manufacturing at Max Planck Insitute for the Science of Light

The follonwing mask have been processed for the manufacturing of the devices on Chapters 2 and 3.

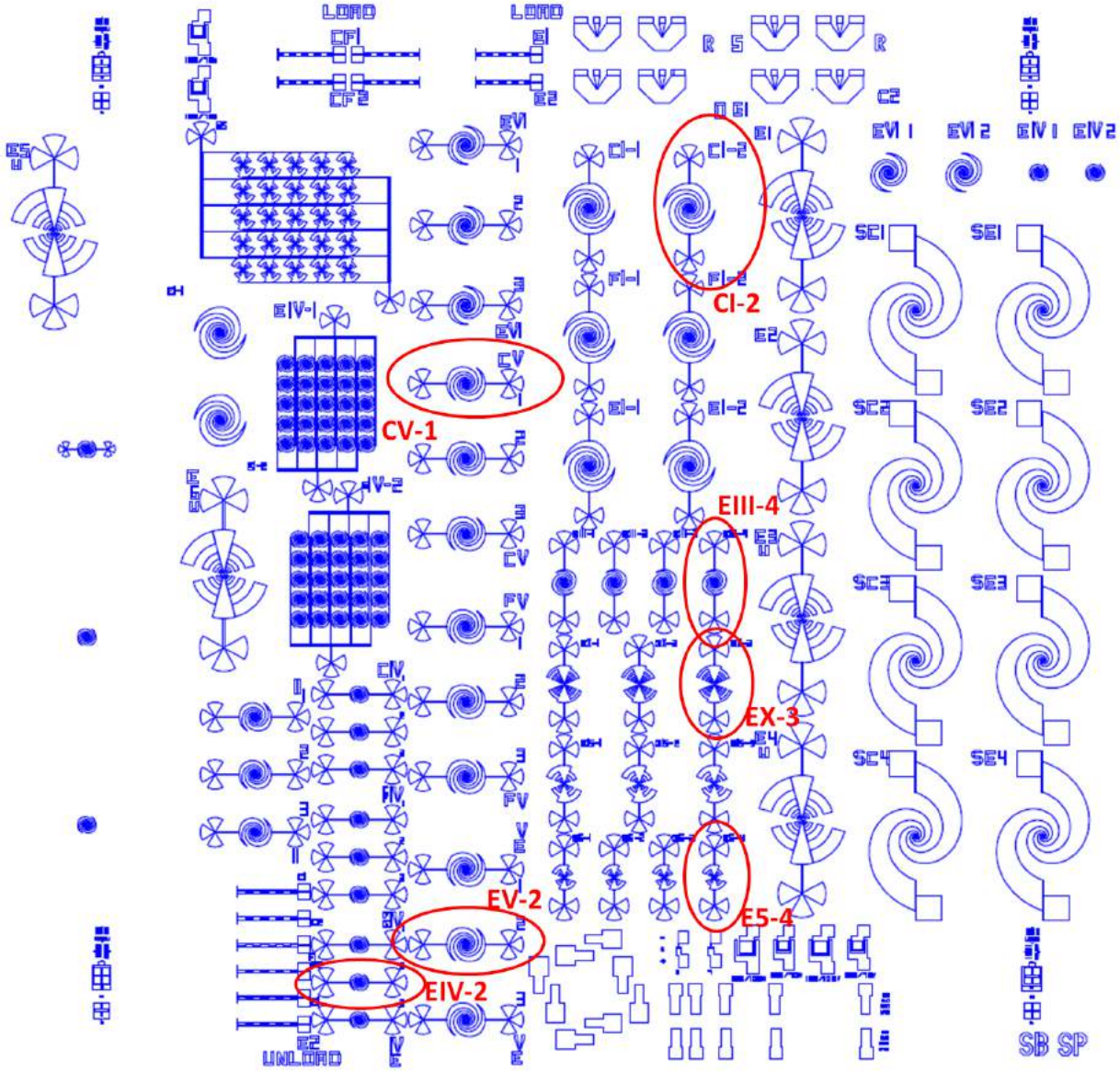

Figure 6.1: First Mask outline

Appendix II

Geometry and specification data employed in PM measurements

Table 6.1: Golay Cell data

Parameter	Data
Diameter of entrance cone, mm	11.0
Diameter of entrance window, mm	6.0
Material of entrance window	High-Density Polyethylene (HDPE)
Optimal operating wavelength, μm	$15 \div 8000$
Recommended detected power, W, up to:	1×10^{-5}
Optimum modulation frequency, Hz	15 ± 5
Noise-equivalent power 20 Hz	
typical, $W/Hz^{1/2}$	1.4×10^{-10}
minimum, $W/Hz^{1/2}$	0.8×10^{-10}
Optical responsitivity 20 Hz	
typical, V/W	1×10^5
maximum, V/W	1.5×10^5
Response rate	
typical, ms	30
minimum, ms	25
Detectivity (D) at entrance cone aperture:	
typical, $cm \times Hz^{1/2}/W$	7.0×10^9
maximum, $cm \times Hz^{1/2}/W$	11.0×10^9
Ambient operating pressure range, mm Hg	$760 \div 10^{-3}$
Operational and storage temperature range, $\circ C$	$5 \div 40$
Humidity, %	$45 \div 80$
Vibration	avoid vibrations at $1 \div 100$ Hz
Rated voltage, AC	$100/115 \pm 10\%$ $220/230 \pm 10\%$
Line frequency, Hz	$50 \div 60$
Overall dimensions, $L \times W \times H$, mm^3	$126 \times 45 \times 87$
Weight, kg	0.8

Table 6.2: Parabolic mirror data

Parameter	Data
Diameter, mm	76.20
Diameter tolerance, mm	$+1.0/-0$
Effective Focal Length (EFL), mm	150.50
Focal length tolerance (%)	± 1
Aperture (f#)	5.80
Edge Thickness (ET), mm	12.70
Surface Accuracy (λ)	1/8
Substrate	Pyrex®7740
Coating	Enhanced Aluminum, $R_{avg} > 95\%@450 - 650nm$
Typical energy density limit	$0.2J/cm^2$ @532, $10ns$
Back surface	Ground
RoHS	Exempt